ASSESSMENT OF WILCOX κ - ω TURBULENCE MODEL IN REGIONS OF SHOCK-WAVE TURBULENT BOUNDARY-LAYER INTERACTION

BY ROBERT A. ALVIANI

A thesis submitted to the

School of Graduate Studies

Rutgers, The State University of New Jersey

in partial fulfillment of the requirements

for the degree of

Master of Science

Graduate Program in Mechanical and Aerospace Engineering

Written under the direction of

Doyle D. Knight

and approved by

_____

_____

_____

_____

New Brunswick, New Jersey

October, 2018

ABSTRACT OF THE THESIS

Assessment of Wilcox κ - ω Turbulence Model in Regions of Shock-Wave Turbulent Boundary-Layer Interaction

by Robert A. Alviani

Thesis Director: Doyle D. Knight

Turbulence models require constant research and development due to the nature of the models themselves. This thesis investigates the fidelity of the Reynolds-averaged Navier-Stokes (RANS) based 2006 Wilcox κ - ω turbulence model. The commercial flow solver GASPex is utilized for simulations, along with MATLAB for grid generation and Tecplot for post-processing. Associated results obtained are subsequently compared to an experimental study done by CUBRC in 2014. In this study, CUBRC ran a series of supersonic flow experiments on multiple physical configurations. The data obtained from these experiments include surface pressure and surface heat transfer values in regions of shock-wave turbulent boundary-layer interaction (SBLI). The purpose of the study was to document this data for further blind code validation studies. This thesis focuses on the results obtained for the large cone flare configuration. Ten runs were completed on the large cone flare, where six of the ten runs were simulated for comparison. Corresponding Mach numbers for the experiment range from 5 to 8. A grid convergence study was done and documented to ensure solution independence of grid discretization. Computational results conclude that the Wilcox κ - ω model predicts surface pressure well for all cases. Average surface pressure is predicted reasonably

upstream of SBLI and post-flare, and peak surface pressure is predicted within the experimental uncertainty. However, separation is found to be significantly over-predicted for most cases. The Wilcox κ - ω model is shown to predict surface heat transfer poorly throughout. In regions of SBLI, surface heat transfer is shown to be drastically over-predicted, especially peak magnitudes. Additionally, it can be seen that the Wilcox κ - ω model produces a large anomalous spike in surface heat transfer downstream of the cone-flare junction in all cases. This spike is shown to be directly correlated to a large spike in turbulent kinetic energy near the surface of the large cone, observed at the same location. Causes for this spike are currently unknown and have not been further investigated, however similar spikes have been seen in the computational results obtained for the hollow cylinder flare configuration. Future work encompasses further assessment of the Wilcox κ - ω model in similar flow regimes. Since over-prediction is a strong factor of error in regions of SBLI, modifications to the Wilcox κ - ω model are required for more accurate predictive capabilities. The anomalous spike that occurs in surface heat transfer also needs be fully investigated to determine possible causes and resolutions.

Keywords: Hypersonics, CFD, RANS, Turbulence, Wilcox, SBLI

Acknowledgements

In light of everything I have accomplished, I would like to take the time to acknowledge and thank everyone that has helped get me here. First and foremost, I would like to thank my mother, Francesca Alviani, and my father, Michael Alviani, for the unconditional love and support they have provided me throughout my life. I would also like to thank my godmother, Dr. Anne Marie Petrock, for always giving me the encouragement I needed to pursue my aspirations and goals. Lastly, I would like to acknowledge my two brothers, Christopher and Nicholas Alviani, and the entirety of my extended family. Thank you all for being an ever-growing positive influence in my life.

In addition to my family, I would also like to acknowledge the people who have directly contributed to my academic and personal success while at Rutgers. First, I would like to thoroughly thank my advisor Dr. Doyle Knight, who has always pushed me to achieve the absolute best of my possibilities. What Professor Knight has taught me throughout my research is truly invaluable, and this thesis would have never came to fruition without his guidance. I would also like to thank the members of my lab, Nadia Kianvashrad and Saumil Patel, who stepped in whenever I was stuck and needed help with my research. Additionally, I would like to thank Rutgers' department of Mechanical and Aerospace Engineering, as well as its faculty, who have molded me into the engineer that I am today. And lastly, I would like to acknowledge the members of the graduate committee who have reviewed this thesis, as well as the Graduate Director Dr. Jerry Shan. Thank you all for what you have done for me.

Dedication

This thesis is hereby dedicated to my grandparents Anthony and Maria Pia Alviani. You will always hold a place in my heart.

Table of Contents

List of Figures

List of Tables

Chapter 1

Introduction

Aerodynamics, a sub-field of fluid and gas dynamics, has been researched and applied to countless applications throughout history. Human advancements such as flying and space travel were made possible by the advancements in this field. Aerodynamics is indefinitely expanding with new research, and dates back to the times of Aristotle and Archimedes. Throughout history, notable researchers in aerodynamics include Leonardo Da Vinci, Sir Isaac Newton, Daniel Bernoulli, Leonhard Euler, and Sir George Cayley. Da Vinci (1505) was the first to consider the concepts of lift when observing bird flight [1]. Newton (1687), who is considered the first aerodynamicist in a modern sense, developed the early theories of air resistance [2]. Bernoulli (1738) developed relationships between pressure and velocity in flowing fluids, and Euler (1757) used these principles to derive the well-known Euler equations [3]. Cayley (1810), who is recognized as the "father of aviation", discovered the generation of lift due to the pressure distribution on the surface of a wing [3]. The list of notable researchers who contributed to the field of aerodynamics can be considered much larger as numerous developments have been made throughout history, and is therefore condensed for brevity.

The field of aerodynamics can be narrowed into smaller sub-fields for further consideration. One of the areas that can be considered is supersonic aerodynamics. This field encompasses all flow that that moves faster than the speed of sound, i.e. Mach ≥ 1. Additionally, three separate flow regimes can be discussed. These regimes are sonic, Mach $= 1$, supersonic, $1 <$ Mach < 5, and hypersonic, Mach ≥ 5. While the first photographs showing proof of supersonic phenomena such as shock waves were published by Ernst Mach in 1887 [4], the creation of a manned aircraft able to fly supersonically in level flight wasn't achieved until 1954. This aircraft was the American X-1B, which was the

first in a series of rocket-powered aircrafts purposed for experimental research [5]. The developments in supersonic aerodynamics that made the X-1B possible were made by many notable contributors, such as Ludwig Prandtl, Theodor Meyer, Adolf Busemann, and Theodore von Karman [6]. Research in supersonics has expanded immensely since the X-1B and has been essential to developments in aerodynamics, propulsion, and combustion.

While supersonic aerodynamics and development have flourished over the years, new found problems and issues have as well. One issue is that when working with the highly non-linear Navier-Stokes equations, numerical approximations are often required in order to obtain solutions. Subsequently, this produced the new area of research known as computational fluid dynamics (CFD). Considering that the numerical calculations employed in CFD require computing power to be remotely feasible, research and development of CFD methods weren't actualized until the rise of computers in the late 1950's. Early developments in CFD were made by various researchers such as Sergei Godunov, Peter Lax, Burton Wendroff, and Robert MacCormack. These developments include Riemann-based schemes (Godunov), hyperbolic dissipative schemes (Lax-Wendroff), and explicit Navier-Stokes methods (MacCormack) [7]. Further progression of CFD methods took place in the 1970s with the development of the potential flow equations. Later in the 1980's, invscid Euler and Navier-Stokes schemes were developed by Bram van Leer, Joseph Steger, R.F. Warming, Philip Roe, and Ami Harten. These developments include the high-order Godunov scheme (van Leer), flux-vector splitting scheme (Steger-Warming), approximate Riemann solver (Roe), and total variation diminishing scheme (Harten) [7]. Additional CFD development continued into the 21st century up to present day, with research producing new methodology and modifications to existing schemes/codes.

While these developments pushed the capabilities of CFD and allowed for excellent prediction of compressible fluid dynamics, the incorporation of turbulence has been a persistent issue. Turbulence and associated modeling have been well-studied and documented throughout history, with notable contributions from Joseph Boussinesq, Osborne Reynolds, and Ludwig Prandtl. Arguably, the start of turbulence modeling began

when Boussinesq (1877) postulated that turbulent stresses are linearly proportional to mean strain rates [8]. Later, Reynolds (1895) proposed that turbulent quantities can be separated into two portions, mean and fluctuating, also known as Reynolds Averaging (a statistical approach). This led to the notion that turbulence can be considered a random, or chaotic, phenomenon [9]. These two developments led to what are known as the Reynolds-averaged Navier-Stokes (RANS) equations. However, due to insufficient knowledge of viscous flows at the time, further progress was halted until Prandtl's (1904) discovery of the boundary layer. About thirty years later, Prandtl (1925) then proposed a method of prediction of eddy viscosity, the turbulent transfer of momentum by eddies, dubbed the mixing-length theory [9]. This theory was developed into the first algebraic turbulence model, or the zero-equation model. At the end of World War 2, Prandtl (1945) further postulated a new model where eddy viscosity depends on the kinetic energy of turbulent fluctuations, κ [9]. This introduced a new differential transport equation to the Navier-Stokes equations and thusly become the first one-equation turbulence model. In the one-equation model, eddy viscosity depends on history of the flow and thus is more physically realistic than the algebraic model [9]. However, a turbulence length scale specification is still required and therefore this model is considered incomplete. Andrey Kolmogorov (1942) proposed the first complete turbulence model, where two differential transport equations are presented [9]. The first is a modeled equation for turbulent kinetic energy, κ, and the second is a modeled equation for the rate of dissipation of energy, ω. This model is known as the first two-equation model, although it was not extensively used until further progression of computing methods. Additionally, another type of turbulence model was created by Julius Rotta (1951), the Reynolds stress transport model, which removed the dependence of the Boussinesq approximation [9]. Two equation models were further developed throughout the 20th century, such as the κ - ω model by Philip Saffman (1970) and the κ - ϵ model by Brian Launder and Dudley Spalding (1972) [9]. Although Launder's κ - ϵ model saw popular use, it showed demonstrable inadequacy in prediction of flows with adverse pressure gradients. Saffman's κ - ω model overcame this significant issue by integrating through the viscous sublayer, thus becoming the more popular model of the two [9].

The κ - ω model was further developed through the end of the 20th century into the 21st century by various contributors such as David Wilcox and Florian Menter. The latest modified κ - ω model was introduced in 2006 by Wilcox, and consequently is the primary turbulence model that is investigated for this thesis.

Aside from RANS-based turbulence models, there are multiple Navier-Stokes solvers that attempt to resolve turbulence features differently. Among these are large eddy simulation (LES), detached eddy simulation (DES), and direct numerical simulation (DNS). Each method has its own respective advantages and disadvantages when comparing to their RANS-based cousins. For example, while DNS allows for numerical resolution of the whole range of spatial and temporal scales of turbulence, it is extremely computationally expensive [10]. LES allows for reduction of computational cost by ignoring the smaller length scales, hence the name, but is still more computationally expensive than RANS-based models [10]. DES acts as a combination of both RANS and LES modeling but requires more complicated meshes due to the separation of RANS and LES regions [11]. Considering that the scope of this thesis revolves around the RANS-based Wilcox κ - ω model, these models will not be further discussed.

1.1 Concluding Remarks

With a layout of the history of aerodynamics, CFD, and turbulence modeling, the last question to answer is: "how accurate are the current models"? David Dolling published an article in 2001 summarizing modern shock-wave boundary-layer interaction (SBLI) research, concluding that important quantities for strong interactions are consistently predicted poorly [12]. Countless studies have been done in congruence to this publication. One of such studies, done in 1998 by Doyle Knight and Gerard Degrez, concluded that surface pressure, surface heat transfer, and skin friction obtained from RANS simulations of 2D and 3D interactions were inaccurately predicted [13]. Knight later published in 2003 that RANS computations for compression corner induced SBLI were accurate for weak interactions but still showed significant inaccuracy for strong interactions [14]. Anthony Oliver, et al., (2007) published equivalent results in that

various quantities, such as separation and skin friction, were predicted reasonably well for weak SBLI interactions but poorly for strong SBLI interactions [15]. In an identical computational study to this thesis, Saumil Patel (2018) found that in high Reynolds number flows, the Wilcox κ - ω model largely over-predicted surface heat transfer and separation in regions of SBLI [16]. The studies listed here cover only a small fraction of the investigations into the predictability of current turbulence models; where most, if not all, result in similar conclusions. Collectively, it is abundantly clear that turbulence modeling still requires development in order to improve its predictive capabilities. In order to identify the underlying issues associated with any turbulence model, blind code validation studies are employed. Experimental data obtained from these studies can then be utilized in comparison to simulations conducted with various CFD methods and turbulence models. This is done in order to understand the computational results obtained and the discrepancies between them and experimental data. This information can further be used for assessment of a given turbulence model, which can lead to modifications/corrections of the model. This is where the primary scope of the thesis lies, which is the assessment of the Wilcox κ - ω turbulence model. Specifically, assessment is conducted in SBLI regions for hypersonic, high Reynolds number, flows.

1.2 Outline

The following chapters of this thesis will be briefly outlined. Chapter 2 provides an overview of governing equations and fundamental physics associated with SBLI. Chapter 3 presents the important considerations for the employed numerical schemes using the 1D Euler equations. Chapter 4 presents the formation of the 3D equations employed in research, as well as derivations of the RANS equations and the Wilcox κ - ω turbulence model. Chapter 5 provides the outline of the experimental study conducted by CUBRC, as well as data obtained. Chapter 6 discusses the specific methodology of this thesis, such as the grid generation and commercial software information. Chapter 7 presents the final results of the computational study done for this thesis. Lastly, Chapter 8 provides the grounds for any related future work that can be considered.

Chapter 2

Precursor Physics and Aerodynamics

Before moving into the methodology of this research, a brief overview of the physics involved will be presented. In this chapter, the main topics that are going to be covered are the conservation equations, supersonic flow phenomena, and turbulence. The information presented here will be utilized in further discussions and is considered fundamental to the topics covered in this thesis.

First, the flowfield specification needs to be prescribed. In classical field theory, two specifications exist for flowfield, Eulerian and Lagrangian. The Lagrangian description of flow considers the thermodynamic and flow properties of individual fluid particles [17]. These properties change over time and are tracked for each respective particle. For example, a specific fluid particle's position can be defined as $\mathbf{X}(x_o, t)$ and subsequently, an arbitrary flow property of the particle can be defined as $\phi(\mathbf{X}(x_o, t), t)$. The Eulerian description of flow considers the thermodynamic and flow properties of specific locations of the flow, rather than the fluid particles themselves [17]. Here, individual particles are ignored and fluid properties can be written as a function of space and time. Consider a location $\mathbf{x}$, and time t, where an arbitrary fluid property can then be written as $\phi(\mathbf{x}, t)$. Further, the Eulerian and Lagrangian specifications can be related by what is known as the material derivative. Essentially, the material derivative describes the time rate of change of a physical quantity that is subjected to a velocity field $\mathbf{V}(\mathbf{x}, t)$ [17]. For the arbitrary fluid property $\phi(\mathbf{x}, t)$, this can be written as follows.

$$\frac{D\phi}{Dt} = \frac{\partial \phi}{\partial t} + \mathbf{V} \cdot \nabla \phi = \frac{\partial \phi}{\partial t} + u\frac{\partial \phi}{\partial x} + v\frac{\partial \phi}{\partial y} + w\frac{\partial \phi}{\partial z} \tag{2.1}$$

2.1 Conservation of Mass, Momentum, and Energy

This section will follow the derivations published by Anderson (2003) [18]. The main focus of continuum mechanics is the derivations of fundamental equations that are valid for all continuous media [19]. These equations, which are based on the universal laws of physics, are known as the conservation equations. One method of derivation of the conservation equations utilizes the Eulerian specification and is known as the control volume approach. This approach employs a stationary finite control volume, hence Eulerian, to derive the fundamental conservation equations. The basic formation of this derivation is done by setting an arbitrary control volume around a fluid flow, with inclusion of a control surface around boundaries. Using this system, the conservation equations can be derived with use of various conservation laws. The three laws employed are the law of conservation of mass, the law of conservation of linear momentum, and the first law of thermodynamics.

First is the continuity equation. This equation is derived from the law of conservation of mass, which states that mass cannot be created or destroyed [20]. The control volume formation of the continuity equation relates the rate of change of mass inside the control volume to net mass flow into the control volume. The terms below contain the fluid density ρ, the fluid velocity vector $\mathbf{V} = u\hat{i} + v\hat{j} + w\hat{k}$, the control volume V, the unit normal vector $\hat{\mathbf{n}}$, and the control surface A. With this, the continuity equation can be shown as:

$$\frac{\partial}{\partial t}\iiint_V \rho dV = -\oiint_A \rho(\mathbf{V}\cdot\hat{\mathbf{n}})dA \tag{2.2}$$

Second is the conservation of momentum equation. The law of conservation of linear momentum, derived from Newton's laws, states that linear momentum is neither created or destroyed and is only changed through the action of forces [20]. Therefore, in the control volume approach, the conservation of momentum equation is formed by equating the rate of change of momentum inside the control volume to the net forces exerted onto the fluid and net flux of momentum across the control surface. Here, new

terms p and $\boldsymbol{\mathcal{F}}_{viscous}$ $\{\hat{i}, \hat{j}, \hat{k}\}$ represent the fluid pressure and viscous forces exerted on the fluid, respectively. It should also be noted that external body forces are ignored. Thus, the conservation of momentum equation can shown in integral form as:

$$\frac{\partial}{\partial t}\iiint_V \rho \mathbf{V} dV + \oiint_A \rho \mathbf{V}(\mathbf{V}\cdot\hat{\mathbf{n}})dA = -\oiint_A p\hat{\mathbf{n}}dA + \boldsymbol{\mathcal{F}}_{viscous} \tag{2.3}$$

Last is the conservation of energy equation. The first law of thermodynamics states the same as the above two laws, in that energy is considered conserved and only changed with the action of work and heat addition [20]. In the control volume approach, the conservation of energy equation relates the rate of change of total energy inside the control volume to the rate of heat addition to the fluid, net work exerted onto the fluid, and net flux of energy across the control surface. Additional new terms consist of e, $\mathcal{W}_{viscous}$, and $\dot{\mathcal{Q}}$; which represent total energy of the fluid per unit mass, viscous work exerted on the fluid, and rate of global fluid heat transfer, respectively. Further, the conservation of energy equation can be shown as:

$$\frac{\partial}{\partial t}\iiint_V \rho e dV + \oiint_A \rho e(\mathbf{V}\cdot\hat{\mathbf{n}})dA = -\oiint_A p(\mathbf{V}\cdot\hat{\mathbf{n}})dA - \dot{\mathcal{Q}} + \mathcal{W}_{viscous} \tag{2.4}$$

2.1.1 Differential Mapping / Constitutive Relationships

Using mathematical analysis, conservation equations (2.2)-(2.4) can be represented as a system of differential equations. These equations are commonly employed for fluid dynamic calculations, and are subsequently introduced/discussed in Chapter 4. To obtain the conservative differential formations, the control volume equations must be mapped to their respective differential forms. For example, consider an arbitrary function ϕ, as well as a basic control volume integral equation shown as:

$$\frac{\partial}{\partial t}\iiint_V \phi dV + \oiint_A \phi(\mathbf{V}\cdot\hat{\mathbf{n}})dA = 0 \tag{2.5}$$

The divergence theorem is first applied in order to convert the surface integral in equation (2.5) to a volume integral. In addition, the time derivative attached to the volume integral in equation (2.5) can be moved inside the integral due to the control volume being independent of time. These two modifications can be shown as:

$$\oiint_A \phi(\mathbf{V}\cdot\hat{\mathbf{n}})dA = \iiint_V \nabla\cdot(\phi\mathbf{V})dV, \qquad \frac{\partial}{\partial t}\iiint_V \phi dV = \iiint_V \frac{\partial\phi}{\partial t}dV \tag{2.6}$$

Utilizing relations shown in (2.6), a single volume integral containing all terms can be obtained. Further, it can be noted that if an integral over an arbitrary volume is equal to zero, then the integrand must also be equal to zero everywhere in volume [18]. Thus, equation (2.5) is further transformed into the final conservative differential form.

$$\begin{gathered}\iiint_V \left[\frac{\partial\phi}{\partial t} + \nabla\cdot\big(\phi\mathbf{V}\big)\right]dV = 0 \\ \frac{\partial\phi}{\partial t} + \nabla\cdot\big(\phi\mathbf{V}\big) = 0\end{gathered} \tag{2.7}$$

At this point, it is important to note constitutive relationships that are associated with these equations. From classical thermodynamics, the constitutive relationship, or equation of state, can be obtained for an ideal gas. Additionally, the relationship between total energy e and internal energy e_i, can be shown as follows.

$$\rho = pRT, \qquad e = e_i + \frac{1}{2}||\mathbf{V}||^2 \tag{2.8}$$

Along with this, internal energy e_i, which total energy can be derived from, can be defined by two state variables such as $e_i = e_i(T, P)$. With additional assumptions, this expression can be shown as an exact relation. For a thermally perfect gas, internal energy can be related to just one thermodynamic property such as $e_i = e_i(T)$, where the derivative can be shown as $de_i = c_v dT$. For a calorically perfect gas, internal energy can be explicitly related to temperature and heat capacity, such as that $e_i = c_v T$.

2.2 Supersonic Flow

The following section will follow the derivations published by Anderson [18]. The main considerations when discussing supersonic flow lies in the phenomena associated with it. The most basic supersonic phenomena that can be considered are shock waves and expansions fans. Fundamentally, shock waves will cause the flow to discontinuously change its speed and related thermodynamic quantities. There are various classifications for shock waves, such as normal, oblique, strong/weak, and detached/attached. Normal shocks can occur for supersonic flow in situations such as within pipe flow (normally when chocked). Oblique shocks are often seen at the leading edge of a sharp object (flat plate) or due to a physical ramped surface (compression corner). Oblique shocks can additionally be considered strong or weak, depending on specific physical and flow quantities (e.g. deflection angle and incoming Mach number). Most notably, oblique shocks waves will occur during supersonic flow when the flow is forced to turn into itself. This is illustrated for an inviscid, two-dimensional, flow in Figure 2.1. Essentially, this happens when the flow hits, or goes over, a changing boundary. If the changing boundary causes the flow to be deflected up, an oblique shock will form. An easy way to describe an oblique shock is a coalescence of infinite compression waves placed directly on top of each other. For sea-level, supersonic air flow, the thickness of a shock wave is roughly on the order of a mean free path $\mathcal{O}(10^{-5}$ inches) [21]. In the case of an oblique shock, flow properties, such as velocity and Mach number, decrease instantaneously. Related thermodynamic properties, such as density and temperature, increase instantaneously. This instantaneous change additionally causes large entropy generation due to stagnation pressure decreases.

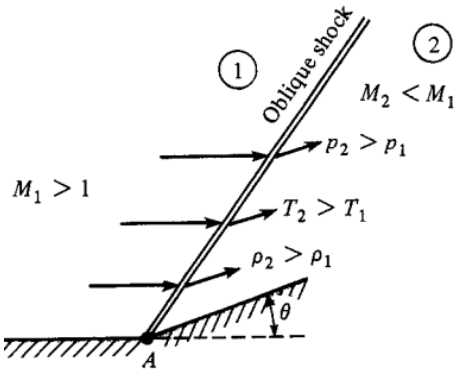

Figure 2.1: Oblique Shock [18]

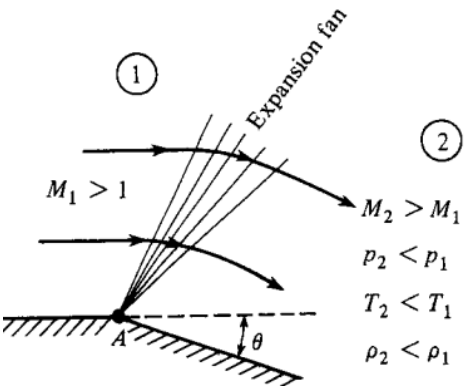

Figure 2.2: Expansion Fan [18]

The contrary of this occurs when the supersonic flow moves over a boundary that is fanning. This will cause an expansion fan to form, as seen to the left in Figure 2.2 (also inviscid). Similarly to an oblique shock, an expansion fan can be considered a coalescence of weak expansion waves. For the situation shown, flow is forced to turn away from itself and thus opposite affects seen by the oblique shock occur. As a result, flow properties increase and related thermodynamic properties decrease. However, unlike an oblique shock, this change occurs continuously with zero entropy generation.

2.2.1 Conical Flow, 3D Considerations

This subsection follows observations made in NASA technical report 1135 [22]. Further considerations can be noted pertaining to supersonic flow over a cone. First, consider the 2D case of a cone which can be represented as a wedge. For this, supersonic flow will hit the leading edge of the cone and create an oblique shock seen in Figure 2.1. For a cone however, 3D relieving effects take place and significantly affect the magnitude of change in flow quantities. Aside from this, it is important to note that the strength of the oblique shock for both a cone and a wedge is a function of the deflection angle, σ, and flow Mach number. This strength can be noted to affect shock angle and associated changes in flow quantities. Certain deflection angle and Mach number combinations can result in either an attached or detached leading edge shock. An attached shock operates as an oblique shock, where a detached shock operates as a strong/bow shock. Additionally, if an attached shock forms at the leading edge of a 3D cone, it can be stated that the shock wave will take the 3D formation of a circular cone as well. Due to this, flow quantities are determined as constant across concentric conical surfaces between the shock and the cone and as a result, can be considered to depend only

on one spatial direction. This is useful when considering computational analysis of cone geometries, as a pseudo-2D axisymmetric representation of a cone is sufficient for modeling. In turn, this greatly reduces the computational loading of a fluid simulation without loss of important physical phenomena.

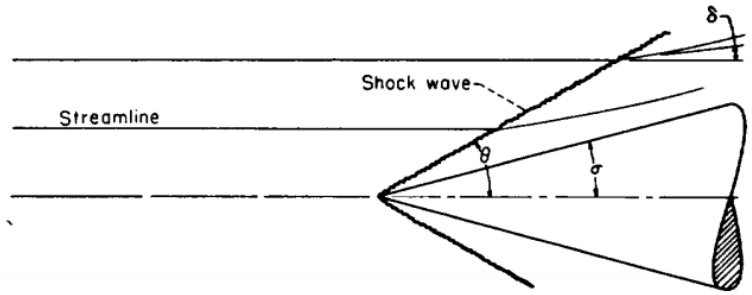

Figure 2.3: 3D Conical Flow [22]

2.2.2 Shock-Wave Boundary-Layer Interaction

This subsection follows the outline presented by Bibin, et. al., (1993) [23]. As the main focus of investigation for this thesis is within regions of shock-wave boundary-layer interaction (SBLI), the phenomena associated with SBLI will be presented. SBLI occurs mainly in regions of supersonic inviscid-viscous interaction and leads to boundary layer separation, as well as peak aerothermodynamic loading. While SBLI can occur in multiple situations, ramp-induced SBLI will be discussed. Consider supersonic flow across a flat plate, illustrated on the next page in Figure 2.4. Viscous effects are not ignored, and thusly a laminar boundary layer is formed along the surface. In addition, a weak oblique shock will form as the flow hits the leading edge of the flat plate due to the boundary layer displacement thickness. Further downstream, the compression corner will induce an adverse pressure gradient, which will result in flow separation of the boundary layer (S). Separation will also produce a free-shear layer which acts as a boundary layer not attached to a physical surface. Aside from separation, multiple shocks are present in SBLI. Due to the abrupt change of flow at the separation point, a

separation shock will form at the start of the separation region. Similarly, a reattachment shock will form at the end of separation (R). In the situation shown, shock-shock interaction occurs downstream (triple-point), where a discontinuity in entropy is seen due to differing shock families (slip-line). Lastly, peak aerothermodynamic loading is usually seen directly at reattachment (R). It should be noted that since SBLI strongly depends on freestream/physical conditions, various differing SBLI formations can be seen aside from what's presented.

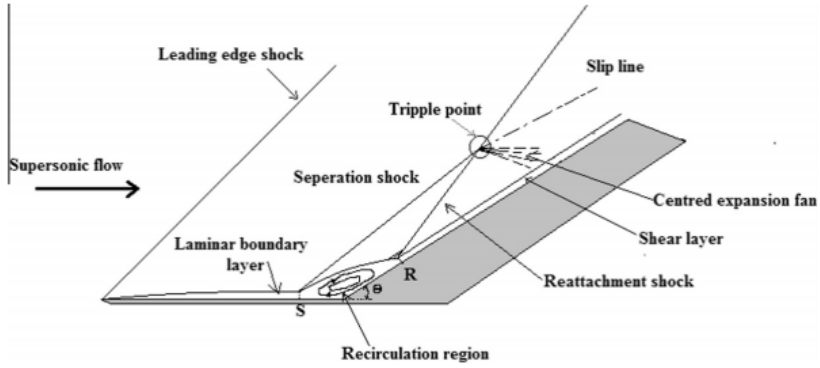

Figure 2.4: Shock-Wave Boundary-Layer Interaction [23]

2.3 Turbulence

Turbulence can be described as random chaotic fluctuations in fluid flow properties. Turbulence is a continuum phenomenon, and can be characterized by irregularity, diffusivity, and dissipation [24]. The energy cascade, which is the transfer of energy from large scales to small scales, as well as the Reynolds number, which is the ratio of inertial forces to viscous forces, can be noted as driving mechanisms of turbulent flows [25].

Turbulent flows are always considered highly irregular and thus normally treated with a statistical approach [24]. This is done by decomposing flow quantities into a sum of their mean and fluctuating portions. The mean, or average, can be obtained in various ways, such as with respect to time. Consider a turbulent velocity $u_i(x,t)$ that is

fluctuating with time, as shown in Figure 2.5. In this figure, $U_i(x)$ (shown) is the time-averaged mean, and $u_i''(x,t)$ (not shown) consists of the fluctuations of $u_i(x,t)$ from the mean $U_i(x)$. This is known as Reynolds-averaging and is fundamental to development of the Reynolds-averaged Navier-Stokes (RANS) equations.

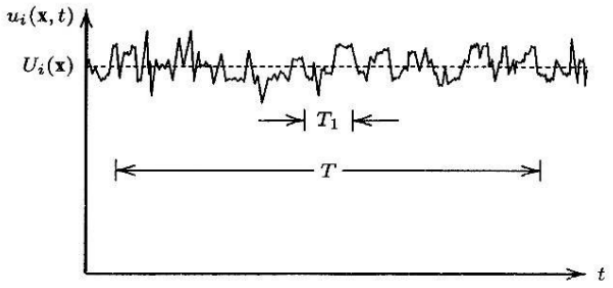

Figure 2.5: Time-Averaged Velocity [9]

Following Tennekes and Lumley (1972) [24], turbulence can be characterized by diffusivity, rotationality, and dissipation. The diffusivity of a turbulent flow can be characterized by the increased rates of mass, momentum, and energy transport. Turbulent diffusion also leads to rapid mixing of the fluid. The rotationality of turbulence can be shown as high levels of fluctuating vorticity. In 3D, vortices are subjected to stretching and squeezing due to vorticity gradients, which is known as vortex stretching. Vortex stretching acts as a vorticity-maintenance mechanism, and since absent in 2D flows, forces turbulence to always be considered three dimensional. The dissipation of turbulence flows can be characterized by the rapid kinetic energy dissipation of the flow. Through this, eddies of differing length scales are formed. The energy cascade from large-scale structures to smaller scales occurs due to inertial instabilities. This cascade of energy continues to transfer to smaller and smaller scales until molecular diffusion becomes important and viscous dissipation occurs. The scale at which this happens is known as the Kolmogorov Length Scale [26].

Laminar flow will typically transition to turbulence when the Reynolds number becomes $\mathcal{O}(10^5)$ [27]. This transition is visualized in Figure 2.6 (a) for a cigarette plume. A laminar boundary layer in the same situation will become unstable and transition

into a turbulent boundary layer. A fully-developed turbulent boundary layer, as seen in Figure 2.6 (b), consists of three layers with differing length scales. These layers are known as the viscous sublayer, non-viscous rotational layer, and outer potential (inviscid) layer. Flow within the bottom two layers is not steady, however the extremely small viscous sublayer is considered near-laminar because of the overwhelming effects of viscosity [24]. Turbulence clearly plays a large role in SBLI, and as mentioned, requires statistical modeling. The method of turbulence modeling employed in this thesis is further discussed in Chapter 4.

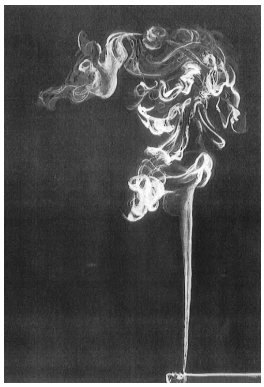

(a) Turbulence Transition [24]

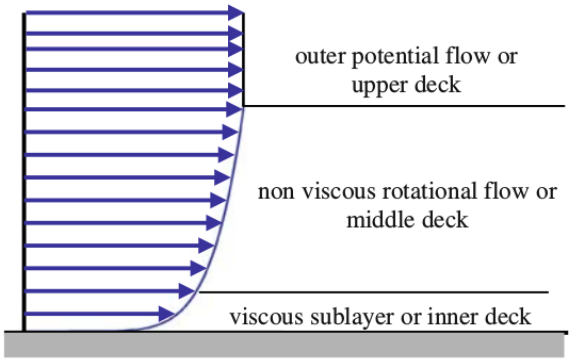

(b) Turbulent Boundary Layer [28]

Figure 2.6: Turbulence Transition and Boundary Layer Schematic

Chapter 3

Numerical Considerations

Computational fluid dynamics (CFD) revolves around solving the governing partial differential equations, as well as integral formation of these equations, via numerical approximations. This chapter will present the basic numerical considerations of the one-dimensional Euler equations. Numerical considerations associated with the full three-dimensional Navier-Stokes equations, with inclusion of viscous and turbulence effects, can be shown to follow the same principles as described here for the one dimensional Euler equations.

3.1 Finite Difference Method

Taylor expansion is a basic mathematical operation that transforms any function $f(x)$ into a infinite sum around a given point (a). This sum consists of the function defined at that point $f(a)$, as well as its derivatives $f^n(a)$ where:

$$f^n(a) = \left.\frac{\partial^n f}{\partial x^n}\right|_{x=a} \tag{3.1}$$

Taylor theorized that this sum will converge if the nth derivative f^n grows no faster than an arbitrary positive constant to the nth power [29]. Allowing this, then the Taylor expansion of function $f(x)$ can be written as:

$$\begin{aligned} f(x) &= \sum_{n=0}^{\infty} \frac{f^n(a)}{n!}(x-a)^n \\ &= f(a) + \left.\frac{\partial f}{\partial x}\right|_{x=a} \Delta x + \left.\frac{\partial^2 f}{\partial x^2}\right|_{x=a} \frac{\Delta x^2}{2} + \cdots \end{aligned} \tag{3.2}$$

3.1.1 Backward and Forward Euler

The information presented in this subsection follows derivations published by Anderson (1995) [30]. Taylor expansion can be used to replace any quantity, per se, with a sum. Let a represent an arbitrary 1D variable, where $f(x)$ can be denoted as $a(x)$. In addition, consider a discrete set of points x_i, x_{i+1}, x_{i+2}, ... where $x_{i+1} = x_i + \Delta x$. Thus, utilizing Taylor expansion, it can be shown that the value of a_{i+1} can be expanded as:

$$\begin{aligned} a_{i+1} &= a_i + \left.\frac{\partial a}{\partial x}\right|_{x_i} \Delta x + \left.\frac{\partial^2 a}{\partial x^2}\right|_{x_i} \frac{\Delta x^2}{2} + \cdots \\ &\approx a_i + \left.\frac{\partial a}{\partial x}\right|_{x_i} \Delta x \end{aligned} \tag{3.3}$$

where the first line of (3.3) represents the exact definition of a_{i+1}, and the second line represents an approximation in which all higher order terms are ignored. However, re-arrangement of the second line approximation is needed to obtain a useful expression. Thus, (3.3) can be used to define an approximation of the first derivative of a_i as

$$\left.\frac{\partial a}{\partial x}\right|_{x_i} = \frac{a_{i+1} - a_i}{\Delta x} \tag{3.4}$$

which is considered the forward Euler numerical approximation of the derivative of a_i. The backward Euler numerical approximation would incorporate a_{i-1} rather than a_{i+1}. Additionally, a central difference approximation incorporates both. This derivation is fundamental to the finite difference method (FDM) applied to partial differential equations, and can further be expanded on.

The error associated with the approximation in (3.3) can be defined as the exact derivative (Taylor expansion with no approximation) minus the approximated derivative. As a result, the error associated with the approximation is simply a sum of higher order terms dropped. The order of error $\mathcal{O}$ represents the degree of the leading error term. Therefore, the error of the forward Euler approximation (3.4) can be defined as:

$$\left.\frac{\partial a}{\partial x}\right|_{x_i,real} - \left.\frac{\partial a}{\partial x}\right|_{x_i,approx} = \left.\frac{\partial^2 a}{\partial x^2}\right|_{x_i} \frac{\Delta x}{2} + \cdots = \mathcal{O}(\Delta x) \tag{3.5}$$

More advanced schemes can be used to further reduce this error, such as the central difference approximation which has an error of $\mathcal{O}(\Delta x^2)$. Additional considerations such as stability, consistency, and convergence that are also associated with FDM will be covered in an later section.

3.2 Finite Volume Method

The information presented in this section follows derivations published by Versteeg and Malalasekera (2007) [31]. To show the methodology of the finite volume method (FVM), consider a basic 1D advection problem:

$$\frac{\partial \phi}{\partial t} + \frac{\partial \psi}{\partial x} = 0 \tag{3.6}$$

Here, $\phi = \phi(x,t)$ and $\psi = \psi\ (\phi(x,t))$. To derive the FVM, equation (3.6) is first integrated in time ($n \rightarrow n+1$) as shown.

$$\phi^{n+1} = \phi^n - \int_n^{n+1} \frac{\partial \psi}{\partial x} dt \tag{3.7}$$

Allowing a 1D medium of constant area, the spatial domain x can be sub-divided into discrete finite volumes with cell-centers indicated by i, known as volume averaging. With this, the function ϕ can be transformed into its respective volume average $\bar{\phi}$, as:

$$\bar{\phi}^n = \frac{1}{x_{i+\frac{1}{2}} - x_{i-\frac{1}{2}}} \int_{x_{i-\frac{1}{2}}}^{x_{i+\frac{1}{2}}} \phi^n dx \tag{3.8}$$

Further, equation (3.7) can be transformed using relation (3.8) into the following equation, relating ϕ^{n+1} to the spatial integral of ϕ^n minus the temporal integral of $\frac{\partial \psi}{\partial x}$.

$$\bar{\phi}^{n+1} = \frac{1}{\Delta x_i} \int_{x-\frac{1}{2}}^{x+\frac{1}{2}} \left\{ \phi^n - \int_n^{n+1} \frac{\partial \psi}{\partial x} dt \right\} dx \tag{3.9}$$

By applying the divergence theorem to equation (3.9), the following equation can be derived.

$$\bar{\phi}^{n+1} = \bar{\phi}^{n} - \frac{1}{\Delta x_i}\Big\{ \int_{n}^{n+1} \psi_{i+\frac{1}{2}} dt - \int_{n}^{n+1} \psi_{i-\frac{1}{2}} dt \Big\} \tag{3.10}$$

Lastly, the semi-discrete numerical approximation of equation (3.6) can be obtained by further differentiating equation (3.10) with respect to time, as:

$$\frac{\partial \bar{\phi}_i}{\partial t} + \frac{\psi_{i+\frac{1}{2}} - \psi_{i-\frac{1}{2}}}{\Delta x_i} = 0 \tag{3.11}$$

Where equations (3.10) and (3.11) are the final 1D FVM formations.

3.3 1D Euler Equation Formation

The information presented in this section follows derivations published by Knight (2006) [32]. Using CFD methods such as FDM and FVM, numerical approximations for compressible flow can be obtained. The governing equations employed for the following derivations are the 1D Euler equations. Allowing for 1D flow, the compressible Euler equations can be written as:

$$\frac{\partial \rho}{\partial t} + \frac{\partial \rho u}{\partial x} = 0 \tag{3.12}$$

$$\frac{\partial \rho u}{\partial t} + \frac{\partial \rho u^2}{\partial x} = -\frac{\partial p}{\partial x} \tag{3.13}$$

$$\frac{\partial \rho e}{\partial t} + \frac{\partial (\rho e + p)u}{\partial x} = 0 \tag{3.14}$$

Further, equations (3.12)-(3.14) can be written in vector formation as:

$$\frac{\partial \mathcal{Q}}{\partial t} + \frac{\partial \mathcal{F}}{\partial x} = 0 \tag{3.15}$$

Here, the conservative vector $\mathcal{Q}$, and flux vector $\mathcal{F}$, in equation (3.15) can be shown in terms of density ρ, velocity u, pressure p, and total energy e as:

$$\mathcal{Q} = \begin{Bmatrix} \rho \\ \rho u \\ \rho e \end{Bmatrix}, \qquad \mathcal{F} = \begin{Bmatrix} \rho u \\ \rho u^2 + p \\ \rho e u + p u \end{Bmatrix} \tag{3.16}$$

For discussion of flux-vector splitting, it is important to note that $\mathcal{F}$ and $\mathcal{Q}$ can be related through the Euler Identity: $\mathcal{F} = \mathcal{A}\mathcal{Q}$. This relation can further transform equation (3.15) into the following:

$$\frac{\partial \mathcal{Q}}{\partial t} + \mathcal{A}\frac{\partial \mathcal{Q}}{\partial x} = 0 \tag{3.17}$$

The coefficient matrix $\mathcal{A}$ shown in equation (3.17) can be written in terms of velocity u and total enthalpy H:

$$\mathcal{A} = \begin{Bmatrix} 0 & 1 & 0 \\ \frac{1}{2}(\gamma-3)u^2 & (3-\gamma)u & (\gamma-1) \\ \frac{1}{2}(\gamma-1)u^3 - Hu & H-(\gamma-1)u^2 & \gamma u \end{Bmatrix} \tag{3.18}$$

where total enthalpy H can be written as:

$$H = e + \frac{p}{\rho} \tag{3.19}$$

3.3.1 Discretization

The 1D conservation equations (3.12)-(3.14) can be modeled in control volume form as well, for purposes of employment of the FVM. Consider equation (3.15), shown in integral formation as follows.

$$\frac{\partial}{\partial t}\int_V \mathcal{Q}dxdy + \int_{\partial V} \mathcal{F}dy = 0 \tag{3.20}$$

Now, just as with the FVM derivation, equation (3.20) can be applied to a discrete set of control volumes V_i. The solution requires specification of a set of these control volumes. Consider a 1D discretization, where the x-axis is set into M cells, indicted by i, shown below in Figure 3.1.

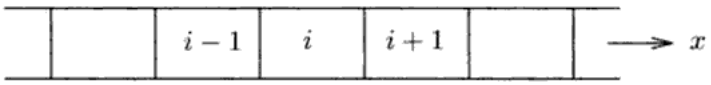

Figure 3.1: 1D Spatial Discretization

Additionally, the time domain can be decomposed as well (Taylor expansion):

$$t^{n+1} = t^n + \Delta t^n \tag{3.21}$$

Then, the conservative vector $\mathcal{Q}$ can be transformed into a volume averaged vector, Q_i. As with the previous derivation, the volume averaged vector Q_i can be shown as:

$$Q_i(t) = \frac{1}{V_i}\int_{V_i} \mathcal{Q}dxdy \tag{3.22}$$

where the 1D volume V_i is equal to $\Delta x \Delta y$. The flux quadrature $\mathcal{F}$, which involves both faces $i + \frac{1}{2}$ and $i - \frac{1}{2}$, can be represented by $F_{i+\frac{1}{2}}$ with the following spatial integral:

$$F_{i+\frac{1}{2}} = \frac{1}{A_{i+\frac{1}{2}}}\int_{x_{i+\frac{1}{2}}} \mathcal{F}dy \tag{3.23}$$

where the 1D intermittent area $A_{i+\frac{1}{2}}$ is equal to Δy. Collectively, the FVM representation of the 1D Euler equations can therefore be defined as:

$$\frac{\partial Q_i}{\partial t} + \frac{\left(F_{i+\frac{1}{2}} - F_{i-\frac{1}{2}}\right)}{\Delta x} = 0 \tag{3.24}$$

where the solution of (3.24) at time $n+1$ can be further be shown as:

$$Q_i^{n+1} = Q_i^n - \frac{1}{\Delta x}\int_{t^n}^{t^{n+1}} \left(F_{i+\frac{1}{2}} - F_{i-\frac{1}{2}}\right) dt \tag{3.25}$$

Equation (3.24) is the final formation by which the the Euler partial differential equations are transformed into a system of ordinary differential equations [32]. It should be noted that equation (3.24) additionally requires the specification of temporal and spatial algorithms. With any choice of algorithm, there are various numerical considerations that require discussion and are subsequently presented in the next section.

3.4 Accuracy, Consistency, Stability, and Convergence

When considering the 1D FVM approach to the Euler equations shown in equations (3.24) and (3.25), several numerical issues need to be considered. As with the previous section, the information presented in this section follows derivations published by Knight (2006) [32]. The four main numerical considerations are presented as follows.

(1) Accuracy: The direct measurement of agreement between the numerical algorithm and the exact solution.

(2) Consistency: The fidelity of the numerical algorithm, with respect to the representation of the actual solution of the governing partial differential equations.

(3) Stability: Ability of the numerical algorithm to remain stable with iteration and avoid temporally unbounded oscillations.

(4) Convergence: The ability of the numerical algorithm to converge to the exact solution with arbitrary reduction of spatial and temporal discretization.

3.4.1 Accuracy

To analyze the accuracy of the above equation, a class of discrete approximations is made to equation (3.25). This results in the following formation:

$$\begin{aligned} Q_i^{n+1} = Q_i^n &- \frac{\Delta t}{\Delta x}\Big\{\theta\Big[F\big(Q_{i+\frac{1}{2}}^{n+1}\big) - F\big(Q_{i-\frac{1}{2}}^{n+1}\big)\Big]\Big\} \\ &- \frac{\Delta t}{\Delta x}\Big\{\big(1-\theta\big)\Big[F\big(Q_{i+\frac{1}{2}}^{n}\big) - F\big(Q_{i-\frac{1}{2}}^{n}\big)\Big]\Big\} \end{aligned} \tag{3.26}$$

The formation presented in equation (3.26) can further be evaluated. First, the the approximation Q can be replaced with the exact expression $\mathcal{Q}$ by the following assumption:

$$Q_{i+\frac{1}{2}} = \mathcal{Q}(x) + \Delta x\mathcal{R}_1(x) + \Delta x^2\mathcal{R}_2(x) + \mathcal{O}(\Delta x^3) \qquad \text{at } x_{i+\frac{1}{2}} \tag{3.27}$$

where $\mathcal{R}_{1,2}$ is dependent on the algorithm employed. Utilizing equation (3.27), $F(Q_{i+\frac{1}{2}})$ can be expressed via Taylor expansion in the following manner.

$$\begin{aligned} F\big(Q_{i+\frac{1}{2}}\big) = F\big(\mathcal{Q}(x)\big) + \frac{\partial F}{\partial Q}\Big[\Delta x\mathcal{R}_1(x) + \Delta x^2\mathcal{R}_2(x) + \mathcal{O}(\Delta x^3)\Big] \\ + \mathcal{O}(\Delta x^2) \quad \text{at } x_{i+\frac{1}{2}} \end{aligned} \tag{3.28}$$

Additionally, the second term of equation (3.26) can be shown as [33]:

$$\begin{aligned} \Big[\theta F\big(\mathcal{Q}_{i+\frac{1}{2}}^{n+1}\big) + (1-\theta)F\big(\mathcal{Q}_{i+\frac{1}{2}}^{n}\big)\Big]\Delta t = \int_{t^n}^{t^{n+1}} F_{i+\frac{1}{2}}dt + (\theta - \frac{1}{2})\Delta t^2\mathcal{T}_1\big(x_{i+\frac{1}{2}}\big) \\ +\mathcal{O}(\Delta t^3) \end{aligned} \tag{3.29}$$

where $\mathcal{T}_1$ depends on F and θ (thus specified by the algorithm).

Equations (3.27)-(3.29) can then be used to transform the discrete approximation (3.26) into the following:

$$\begin{aligned}\mathcal{Q}_i^{n+1} = \mathcal{Q}_i^n - \frac{1}{\Delta x}\int_{t^n}^{t^{n+1}} \Big(F\big(\mathcal{Q}_{i+\frac{1}{2}}\big) - F\big(\mathcal{Q}_{i-\frac{1}{2}}\big)\Big)dt - (\theta - \frac{1}{2})\Delta t^2 \frac{\partial \mathcal{T}_1}{\partial x} \\ - \Delta x \Delta t\Big[\theta \frac{\partial}{\partial x}\Big(\frac{\partial F}{\partial Q}\mathcal{R}_1\Big)^{n+1} + (1-\theta)\frac{\partial}{\partial x}\Big(\frac{\partial F}{\partial Q}\mathcal{R}_1\Big)^{n}\Big] \\ + \mathcal{O}(\Delta t^2 \Delta x) + \mathcal{O}(\Delta t^3) + \mathcal{O}(\Delta x^2 \Delta t)\end{aligned} \tag{3.30}$$

Now, (3.30) can be used to determine accuracy. First, the error associated with this approximation must be defined. The conventional definition of error of an approximated function can be considered:

$$Q_i^{n+1}\Big|_{\text{discrete}} = Q_i^{n+1}\Big|_{\text{exact}} + \mathcal{E}(\Delta t, \Delta x) \tag{3.31}$$

Since error is expected to be formed by Taylor expansion, $\mathcal{E}$ can be decomposed into a polynomial to analyze accuracy as:

$$\begin{aligned}\mathcal{E}(\Delta x, \Delta t) = a\Delta x + b\Delta t + c\Delta x^2 + d\Delta x \Delta t + e\Delta t^2 \\ + \mathcal{O}(\Delta x^i \Delta t^{3-i})\big|_{i=0,\ldots,3} + \ldots\end{aligned} \tag{3.32}$$

Here, it is important to note that the leading non-zero constants define the order of accuracy. For equation (3.30), constants a, b, and c are zero. Constants d and e follow:

$$d = \Big[\theta \frac{\partial}{\partial x}\Big(\frac{\partial F}{\partial Q}\mathcal{R}_1\Big)^{n+1} + (1-\theta)\frac{\partial}{\partial x}\Big(\frac{\partial F}{\partial Q}\mathcal{R}_1\Big)^{n}\Big], \qquad e = -(\theta - \frac{1}{2})\frac{\partial \mathcal{T}_1}{\partial x} \tag{3.33}$$

Equations (3.30)-(3.33) are used to analyze the accuracy of the discrete approximation (3.26). It can first be noted that discretization causes error in terms of temporal and spatial components. Further, the definitions of θ and $\mathcal{R}_1$ are specified by a given algorithm. Directly, it can be seen that if the value of θ is equal to $1/2$, the algorithm

is temporally second-order accurate. Any other value will result in first-order temporal accuracy. Additionally, if $\mathcal{R}_1 = 0$, then the algorithm is spatially second-order accurate. For any non-zero value of $\mathcal{R}_1$, the algorithm is spatially first-order accurate.

3.4.2 Consistency

The consistency of the discrete approximation (3.26) can be determined by comparison to the exact integral formation (3.25) and the exact differential formation (3.15). The discrete approximation (3.26) is deemed consistent if the limit as $\Delta t \to 0$ yields the exact integral formation (3.25) and if the limit as $\Delta x \to 0$ and $\Delta t \to 0$ yields the exact differential formation (3.15). In basic terms, if the discretization of (3.26) is further reduced to an infinite amount of cells, the exact equations in which it was derived must be obtained. Consider the formation of error defined previously:

$$Q_i^{n+1}\Big|_{\text{discrete}} = Q_i^{n+1}\Big|_{\text{exact}} + \mathcal{E}(\Delta t, \Delta x) \tag{3.34}$$

$$\begin{aligned}\mathcal{E}(\Delta x, \Delta t) = a\Delta x + b\Delta t + c\Delta x^2 + d\Delta x\Delta t + e\Delta t^2 \\ + \mathcal{O}(\Delta x^i \Delta t^{3-i})\big|_{i=0,\ldots,3} + \ldots\end{aligned} \tag{3.35}$$

With equations (3.34) and (3.35), it can be shown that the discrete approximation of Q_i^{n+1} will approach the exact solution of Q_i^{n+1} as the error approaches zero. Additionally, it was shown in the previous section that the order of error is $\mathcal{O}(\Delta x\Delta t, \Delta t^2, \ldots)$. With this in mind, it can be implicitly stated that as $\Delta t \to 0$, $\mathcal{E} \to 0$. Additionally, it can also be stated that as $\Delta t \to 0$ and $\Delta x \to 0$, $\mathcal{E} \to 0$ as well. This further provides consistency of the discrete approximation (3.26) to the integral formation (3.25) and the differential formation (3.15), and thus proves that (3.26) is fully consistent.

3.4.3 Stability

Both equations (3.24) and discrete approximation (3.26) can be further evaluated in terms of stability using von Neumann analysis. To determine the stability, spatial discretization is first considered. For illustration, consider a basic flux quadrature:

$$\begin{aligned} F_{i+\frac{1}{2}} &= \mathcal{F}(Q_{i+\frac{1}{2}}), \\ Q_{i+\frac{1}{2}} &= Q_i \end{aligned} \tag{3.36}$$

By applying Taylor expansion and various approximations of terms, equation (3.24) can be further re-written as:

$$\frac{\partial Q_i}{\partial t} + A_i \frac{\left(Q_i - Q_{i-1}\right)}{\Delta x} = 0 \tag{3.37}$$

Additionally, the Fourier series coefficients of Q_i can be shown as:

$$\hat{Q}_k(t^n) = \frac{1}{2N} \sum_{i=1}^{i=2N} Q_i(t^n) e^{-ikx_i} \tag{3.38}$$

Utilizing equation (3.38), equation (3.37) can be re-written in terms of a Fourier series. In addition, matrix A is diagonalized and further simplifications are made:

$$\begin{aligned} &\frac{\partial \hat{Q}_k}{\partial t} + \alpha A \hat{Q}_k = 0 \\ &\frac{\partial \hat{Q}_k}{\partial t} + \alpha T \Lambda T^{-1} \hat{Q}_k = 0 \\ &\frac{\partial \tilde{Q}_k}{\partial t} + \alpha \Lambda \tilde{Q}_k = 0 \end{aligned} \tag{3.39}$$

where $\tilde{Q}_k = T^{-1}\hat{Q}_k$. The solution to the final equation shown in (3.39) can further be found by integration and written as:

$$\tilde{Q}_{k_m}(t) = \tilde{Q}_{k_m}(0) e^{-\alpha \lambda_m t} \tag{3.40}$$

Here, the coefficient α seen in equations (3.39) and (3.40) is key to the stability analysis of equation (3.24). α can be defined as:

$$\alpha = \frac{1}{\Delta x}\Big(1 - \cos k\Delta x\Big) + \frac{i}{\Delta x}\sin k\Delta x \tag{3.41}$$

Thus, in order for equation (3.24) to have spatial stability, the real portion of $\alpha\lambda_m$ must be positive. From equation (3.41), it can seen that the real portion of α, which is equal to $\frac{1}{\Delta x}(1 - \cos k\Delta x)$, is positive for all values of k. However, this requires λ_m to be positive for all values k as well. The eigenvalues of the constant matrix A are:

$$\lambda_1 = u, \qquad \lambda_2 = u + a, \qquad \lambda_3 = u - a \tag{3.42}$$

Therefore, the flux quadrature presented in (3.36) can be considered stable only when $u \geq a$. For this condition, the fluid must be traveling to the right at or above the speed of sound, which is consistent with supersonic flow physics.

Additional considerations for the discrete approximation (3.26) with the flux quadrature shown in (3.36) need to be made to ensure stability. Consider an analog to equation (3.40), derived from the discrete approximation (3.26):

$$\tilde{Q}_k^{n+1} = G\tilde{Q}_k^n \tag{3.43}$$

where the matrix G in equation (3.43) can be defined as:

$$G = \big[I + \Delta t\theta\alpha\Lambda\big]^{-1}\big[I - \Delta t(1-\theta)\alpha\Lambda\big] \tag{3.44}$$

The stability condition for equation (3.43) requires that $||G|| \leq 1$. This allows for the solution to be decaying, thus avoiding temporally unbounded oscillations. For the flux quadrature presented in (3.36), this can be shown more clearly in the following equation.

$$\Big(\frac{\Delta t\lambda_i}{\Delta x}\Big)\Big[\Big(\frac{\Delta t\lambda_i}{\Delta x}\Big)(1-2\theta)-1\Big]=0 \tag{3.45}$$

Equation (3.45) has a dependence on θ, which is prescribed by an algorithm. Consider the explicit Euler algorithm, where $\theta = 0$. With this, the conditions of stability derived from (3.45) take the form:

$$\lambda_i \geq 0 \qquad \text{and} \qquad \Delta t \leq \frac{\Delta x}{\lambda_i} \tag{3.46}$$

which further follows the notion that:

$$u \geq a \qquad \text{and} \qquad \Delta t \leq \Delta t_{CFL} \tag{3.47}$$

The term Δt_{CFL} is often seen in stability analysis and is known as the Courant-Friedrichs-Lewy (CFL) condition. This condition puts a restriction on the discrete time-steps employed by any specific algorithm, and can be expressed as:

$$\Delta t_{CFL} = min\frac{\Delta x}{\lambda_i} \tag{3.48}$$

3.4.4 Convergence

When utilizing a FVM approach for derivation of equation (3.24), the numerical approximation $Q_i^{n,ap}$ converges to the exact solution $Q_i^{n,e}$ if the following expression holds.

$$\lim_{\Delta t,\Delta x\to 0} ||Q_i^{n,e} - Q_i^{n,ap}|| = 0 \tag{3.49}$$

Further, it can be shown that the normalized difference between the exact and approximation solutions is of the same order as accuracy. Therefore, for a spatially and temporally second-order algorithm, the normalized difference can be shown as:

$$||Q_i^{n,e} - Q_i^{n,ap}|| = \mathcal{O}(\Delta t^2, \Delta x^2) \tag{3.50}$$

which therefore implies convergence for equation (3.24).

3.5 Reconstruction

Consider the semi-discrete FVM Euler equations presented previously:

$$\frac{\partial Q_i}{\partial t} + \frac{\left(F_{i+\frac{1}{2}} - F_{i-\frac{1}{2}}\right)}{\Delta x} = 0 \tag{3.51}$$

The discretization of the domain and introduction of the volume averaged vector Q_i(t) results in loss of information of $Q(x,t)$. The time-averaged Q_i requires the fluxes $F_{i\pm\frac{1}{2}}$, which are computed from the local approximate reconstruction $Q_i(x)$ of the exact $\mathcal{Q}_i$. The simplest reconstruction here is that $Q_i(x) = Q_i$; however, this greatly diminishes the numerical fidelity of the solution, and thus higher order accuracy methods are sought. This leads into reconstruction using the primitive function. Through an extensive mathematical proof, the commonly employed *modified upwind scheme for conservation laws*, or MUSCL scheme, can be derived. The final formation follows:

$$\begin{aligned} Q^l_{i+\frac{1}{2}} &= Q_i + \frac{1}{4}\Big[(1-\kappa)\Delta Q_{i-\frac{1}{2}} + (1+\kappa)\Delta Q_{i+\frac{1}{2}}\Big], \\ Q^r_{i-\frac{1}{2}} &= Q_i - \frac{1}{4}\Big[(1-\kappa)\Delta Q_{i+\frac{1}{2}} + (1+\kappa)\Delta Q_{i-\frac{1}{2}}\Big] \end{aligned} \tag{3.52}$$

where the forward and backward gradients $\Delta Q_{i\pm\frac{1}{2}}$ are defined as the difference between cell-centers of adjacent cells as:

$$\Delta Q_{i+\frac{1}{2}} = Q_{i+1} - Q_i, \qquad \Delta Q_{i-\frac{1}{2}} = Q_i - Q_{i-1} \tag{3.53}$$

This reconstruction scheme allows for differing values of κ, which produce multiple types of schemes. Depending on the value of κ, both equations shown in (3.52) can be transformed into either a second or third order reconstruction scheme. Additionally, various values of κ produce differing cell-value dependencies. Associated order and dependencies for κ = -1, 0, 1/3, and 1, are provided on the next page in Table 3.1.

Value	Order	Dependence
$\kappa = -1$	2nd order, upwind	$Q^l_{i+\frac{1}{2}}$ depends on Q_i and Q_{i-1} and $Q^r_{i-\frac{1}{2}}$ depends on Q_i and Q_{i+1}.
$\kappa = 1$	2nd order, centered	$Q^l_{i+\frac{1}{2}}$ depends on Q_i and Q_{i+1} and $Q^r_{i-\frac{1}{2}}$ depends on Q_i and Q_{i-1}.
$\kappa = \frac{1}{3}$	3rd order, upwind bias	$Q^l_{i+\frac{1}{2}}$ depends on Q_i, Q_{i-1}, and Q_{i+1} and $Q^r_{i-\frac{1}{2}}$ depends on Q_i, Q_{i-1} and Q_{i+1}.
$\kappa = 0$	2nd order, upwind bias	$Q^l_{i+\frac{1}{2}}$ depends on Q_i, Q_{i-1}, and Q_{i+1} and $Q^r_{i-\frac{1}{2}}$ depends on Q_i, Q_{i-1} and Q_{i+1}.

Table 3.1: MUSCL Scheme κ Values, Order, and Dependence

For the purposes of this thesis, κ is set to 1/3. Thus, the general reconstruction (3.52) can be shown to be:

$$\begin{aligned} Q^l_{i+\frac{1}{2}} &= Q_i + \frac{1}{6}\Big[\Delta Q_{i-\frac{1}{2}} + 2\Delta Q_{i+\frac{1}{2}}\Big], \\ Q^r_{i+\frac{1}{2}} &= Q_i - \frac{1}{6}\Big[\Delta Q_{i+\frac{1}{2}} + 2\Delta Q_{i-\frac{1}{2}}\Big] \end{aligned} \tag{3.54}$$

which works as a three-stencil method and depends on both adjacent cells as mentioned.

3.5.1 Flux Limiters

While the reconstructed equation (3.52) works very well with smooth, continuous data, large gradients and discontinuities can produce numerical oscillations. In order to maintain stability, the higher-order correction term has to be reduced. Essentially, this forces the reconstruction at cell-faces to be within the limit of adjacent cell-averages. Consider a basic Taylor expansion of the vectors $Q^{l,r}_{i\pm\frac{1}{2}}$.

$$\begin{aligned} Q^l_{i+\frac{1}{2}} &= Q_i + \frac{1}{2}\Big(\frac{\partial Q}{\partial x}\Big)\Delta x = Q_i + \frac{1}{2}\delta Q^l, \\ Q^r_{i-\frac{1}{2}} &= Q_i - \frac{1}{2}\Big(\frac{\partial Q}{\partial x}\Big)\Delta x = Q_i - \frac{1}{2}\delta Q^r \end{aligned} \tag{3.55}$$

To limit the values of $Q^{l,r}_{i\pm\frac{1}{2}}$ to that of adjacent cells, consider the following relation:

$$\begin{aligned} Q_i - \frac{1}{2}\delta Q \geq Q_{i-1}, \\ Q_i + \frac{1}{2}\delta Q \leq Q_{i+1} \end{aligned} \tag{3.56}$$

which clearly shows that if the high-order gradient δQ exceeds $2\Delta Q_{i\pm\frac{1}{2}}$, the magnitude must be limited. Allow the following filter function, where δQ is further related to equation (3.55).

$$\delta Q = R(\theta)\delta Q, \qquad \theta = \frac{\Delta Q_{i+\frac{1}{2}}}{\Delta Q_{i-\frac{1}{2}}} \tag{3.57}$$

$$\min(2\Delta Q_{i+\frac{1}{2}}, 2\Delta Q_{i-\frac{1}{2}}) = R(\theta)\Big\{\frac{1}{2}\Big[(1-\kappa)\Delta Q_{i-\frac{1}{2}} + (1+\kappa)\Delta Q_{i+\frac{1}{2}}\Big]\Big\} \tag{3.58}$$

Further specification of the filter function $R(\theta)$ is set by differing limiters. The limiter of choice for this thesis is the minimum modulus (min-mod) limiter. The min-mod function allows for the smaller (magnitude) of the two gradients to be employed if they have the same sign, and zero otherwise. In conclusion, the min-mod function can be written as:

$$minmod(x,y) = \begin{cases} x, \ |x| < |y| \ \& \ xy > 0 \\ y, \ |x| > |y| \ \& \ xy > 0 \\ 0, \ xy < 0 \end{cases}, \qquad R(\theta) = \begin{cases} \dfrac{2\theta}{\theta+1}, \ 0 \leq \theta < 1 \\ \dfrac{2}{\theta+1}, \ \theta \geq 1 \end{cases} \tag{3.59}$$

3.6 Roe Scheme

The information presented in this section follows derivations from Knight (2006) [32]. Considering that Roe's method is the utilized inviscid flux algorithm, this method will be derived in full. Philip Roe (1981,1986) developed his flux algorithm based on the

exact solution to the generalized Riemann problem. Consider the previously shown conservative form of the differential Euler equations:

$$\frac{\partial \mathcal{Q}}{\partial t} + \mathcal{A}\frac{\partial \mathcal{Q}}{\partial x} = 0 \tag{3.60}$$

where the coefficient matrix $\mathcal{A}$ is once again defined:

$$\mathcal{A} = \begin{Bmatrix} 0 & 1 & 0 \\ \frac{1}{2}(\gamma-3)u^2 & (3-\gamma)u & (\gamma-1) \\ \frac{1}{2}(\gamma-1)u^3 - Hu & H-(\gamma-1)u^2 & \gamma u \end{Bmatrix} \tag{3.61}$$

Roe sought a solution to the generalized Riemann problem by forming an approximate equation to (3.60):

$$\frac{\partial \mathcal{Q}}{\partial t} + \tilde{\mathcal{A}}(\mathcal{Q}_l, \mathcal{Q}_r)\frac{\partial \mathcal{Q}}{\partial x} = 0 \tag{3.62}$$

where $\tilde{\mathcal{A}}(\mathcal{Q}_l, \mathcal{Q}_r)$ is the approximation of the exact matrix $\mathcal{A}$. Roe postulated that the approximate matrix $\tilde{\mathcal{A}}(\mathcal{Q}_l, \mathcal{Q}_r)$ satisfied the following properties, which are important for the derivation of the algorithm.

(i) $\tilde{\mathcal{A}}$ provides a linear mapping from the vector space of $\mathcal{Q}$ to the vector space of $\mathcal{F}$.

(ii) $\tilde{\mathcal{A}}(\mathcal{Q}_l, \mathcal{Q}_r) \rightarrow \mathcal{A}(\mathcal{Q})$ as $\mathcal{Q}_l \rightarrow \mathcal{Q}_r \rightarrow \mathcal{Q}$.

(iii) For any $\mathcal{Q}_l$ and $\mathcal{Q}_r$, $\tilde{\mathcal{A}}(\mathcal{Q}_l, \mathcal{Q}_r)$ x $(\mathcal{Q}_l - \mathcal{Q}_r) = \mathcal{F}_l - \mathcal{F}_r$.

(iv) The eigenvectors of $\tilde{\mathcal{A}}(\mathcal{Q}_l, \mathcal{Q}_r)$ are linearly independent.

These postulations can be determined to have the following effects. (i) Allows the assumption that each component of $\tilde{\mathcal{A}}\mathcal{Q}$ has the same units as $\mathcal{F}$, respectively. Further assuming a smooth $\mathcal{Q}$, (ii) provides the assumption that Roe's approximation (3.62)

is consistent with the exact equation (3.60) and is a close approximation. For discontinuous jumps such as shocks, (iii) shows that Roe's approximation requires exact conditions across a shock. Lastly, (iv) is essential for the linear algebra operations that will be taken. This provides that the matrix $\tilde{\mathcal{A}}(\mathcal{Q}_l, \mathcal{Q}_r)$ can be diagonalizable into real, distinct, eigenvalues and linearly independent eigenvectors. Further, it is assumed that $\tilde{\mathcal{A}}(\mathcal{Q}_l, \mathcal{Q}_r)$ is non-singular, allowing inversion.

To determine the Roe matrix $\tilde{\mathcal{A}}(\mathcal{Q}_l, \mathcal{Q}_r)$, consider the conservative vector $\mathcal{Q}$, and flux vector $\mathcal{F}$, as shown:

$$\mathcal{Q} = \begin{Bmatrix} \rho \\ \rho u \\ \frac{1}{\gamma}[\rho H + \frac{(\gamma-1)}{2}\rho u^2] \end{Bmatrix}, \qquad \mathcal{F} = \begin{Bmatrix} \rho u \\ \frac{1}{\gamma}[(\gamma-1)\rho H + \frac{(\gamma+1)}{2}\rho u^2] \\ \rho H u \end{Bmatrix} \tag{3.63}$$

Additionally, a new vector ν is introduced in which both $\mathcal{Q}$ and $\mathcal{F}$ are a function of ν.

$$\nu = \begin{Bmatrix} \sqrt{\rho} \\ \sqrt{\rho} u \\ \sqrt{\rho} H \end{Bmatrix} \tag{3.64}$$

Further, it is possible to define $\Delta\mathcal{Q}$ and $\Delta\mathcal{F}$ as functions of two separate constant matrices multiplied by $\Delta\nu$.

$$\begin{aligned} \Delta\mathcal{Q} &= B\Delta\nu, \\ \Delta\mathcal{F} &= C\Delta\nu \end{aligned} \tag{3.65}$$

For completeness, it can be noted that $\Delta\mathcal{Q} = \mathcal{Q}_l - \mathcal{Q}_r$, $\Delta\mathcal{F} = \mathcal{F}_l - \mathcal{F}_r$, and $\Delta\nu = \nu_l - \nu_r$. The Euler Identity allows $\mathcal{Q}$ to be related with $\mathcal{F}$ as follows:

$$\Delta\mathcal{F} = \tilde{\mathcal{A}}\Delta\mathcal{Q} \tag{3.66}$$

Combining relation (3.66) with equations in (3.65), and with some additional linear algebra, the relationship between the Roe matrix $\tilde{\mathcal{A}}$ and the constant matrices B and C can be found to be: $\tilde{\mathcal{A}} = CB^{-1}$. Deriving matrices B and C can be done using the relations shown in (3.65), and is not shown for sake of brevity. Once this is done, the Roe matrix $\tilde{\mathcal{A}}$ can be found to be:

$$\tilde{\mathcal{A}} = \begin{Bmatrix} 0 & 1 & 0 \\ \frac{(\gamma-3)}{2}\tilde{u}^2 & (3-\gamma)\tilde{u} & (\gamma-1) \\ \frac{(\gamma-1)}{2}\tilde{u}^3 - \tilde{H}\tilde{u} & \tilde{H} - (\gamma-1)\tilde{u}^2 & \gamma\tilde{u} \end{Bmatrix} \tag{3.67}$$

where $\tilde{\mathcal{A}}$ is defined as the Roe matrix, $\tilde{u}$ the Roe-averaged velocity, and $\tilde{H}$ the Roe-averaged total enthalpy. In addition, $\tilde{u}$ and $\tilde{H}$ are further defined as:

$$\begin{aligned} \tilde{u} &= \frac{\sqrt{\rho_l}u_l + \sqrt{\rho_r}u_r}{\sqrt{\rho_l} + \sqrt{\rho_r}}, \\ \tilde{H} &= \frac{\sqrt{\rho_l}H_l + \sqrt{\rho_r}H_r}{\sqrt{\rho_l} + \sqrt{\rho_r}} \end{aligned} \tag{3.68}$$

It is very interesting to note that the Roe matrix $\tilde{\mathcal{A}}$ is near-identical to the original matrix $\mathcal{A}$. However, does $\tilde{\mathcal{A}}$ satisfy the necessary conditions, (i)-(iv), that Roe postulated about $\tilde{\mathcal{A}}(\mathcal{Q}_l, \mathcal{Q}_r)$? The Euler Identity, $\Delta\mathcal{F} = \tilde{\mathcal{A}}\Delta\mathcal{Q}$, is utilized in the derivations above; which is indeed a linear mapping of $\mathcal{F}$ to $\mathcal{Q}$, thus (i) is satisfied. As mentioned in the first sentence of this paragraph, $\tilde{\mathcal{A}}$ being near-identical to the original matrix $\mathcal{A}$ is not just interesting, but provides grounds for (ii) to be satisfied. From both equations shown in (3.68), it is easy to see that $\tilde{u} \to u$ and $\tilde{H} \to H$ as $\mathcal{Q}_l \to \mathcal{Q}_r \to \mathcal{Q}$. This implies that $\tilde{\mathcal{A}} \to \mathcal{A}$ as well, satisfying (ii). For (iii), it can be noted that before the derivation of $\tilde{\mathcal{A}}$, Δ terms seen in relations (3.65) are defined as $\Delta f = f_l - f_r$. Therefore, (iii) is inherently satisfied. Satisfaction of (iv) however requires additional derivations to be determined.

First, the Roe matrix, $\tilde{\mathcal{A}}(\mathcal{Q}_l, \mathcal{Q}_r)$, must be diagonalized as follows:

$$\tilde{\mathcal{A}} = \tilde{\mathcal{V}}\tilde{\Lambda}\tilde{\mathcal{V}}^{-1} \tag{3.69}$$

Here, $\tilde{\mathcal{V}}$ is a matrix comprised of individual eigenvectors $\tilde{\nu_i}$, and $\tilde{\Lambda}$ is a matrix comprised of individual eigenvalues $\tilde{\lambda_i}$. From the Roe matrix in (3.67), $\tilde{\lambda_i}$ and $\tilde{\nu_i}$ can be found, where relations in (3.70) and (3.71) below consequently satisfy (iv).

$$\tilde{\lambda_1} = \tilde{u}, \qquad \tilde{\lambda_2} = \tilde{u} + \tilde{a}, \qquad \tilde{\lambda_3} = \tilde{u} - \tilde{a} \tag{3.70}$$

$$\tilde{\nu_1} = \begin{Bmatrix} 1 \\ \tilde{u} \\ \frac{1}{2}\tilde{u}^2 \end{Bmatrix}, \qquad \tilde{\nu_2} = \begin{Bmatrix} 1 \\ \tilde{u} + \tilde{a} \\ \tilde{H} + \tilde{u}\tilde{a} \end{Bmatrix}, \qquad \tilde{\nu_3} = \begin{Bmatrix} 1 \\ \tilde{u} - \tilde{a} \\ \tilde{H} - \tilde{u}\tilde{a} \end{Bmatrix} \tag{3.71}$$

Now that the Roe matrix is determined to be consistent with postulations (i)-(iv), further derivations can be made. First, the matrices $\tilde{\Lambda}$ and $\tilde{\mathcal{V}}$ can be shown by combining components of (3.70) and (3.71) as:

$$\tilde{\Lambda} = \begin{Bmatrix} \tilde{u} & 0 & 0 \\ 0 & \tilde{u} + \tilde{a} & 0 \\ 0 & 0 & \tilde{u} - \tilde{a} \end{Bmatrix}, \qquad \tilde{\mathcal{V}} = \begin{Bmatrix} 1 & 1 & 1 \\ \tilde{u} & \tilde{u} + \tilde{a} & \tilde{u} - \tilde{a} \\ \frac{1}{2}\tilde{u}^2 & \tilde{H} + \tilde{u}\tilde{a} & \tilde{H} - \tilde{u}\tilde{a} \end{Bmatrix} \tag{3.72}$$

Additionally, the inverse matrix $\tilde{\mathcal{V}}^{-1}$ can be found:

$$\tilde{\mathcal{V}}^{-1} = \begin{Bmatrix} \frac{1}{2\tilde{a}^2}[1 - (\gamma - 1)\tilde{u}^2] & \frac{1}{\tilde{a}^2}(\gamma - 1)\tilde{u} & -\frac{1}{\tilde{a}^2}(\gamma - 1) \\ \frac{1}{4\tilde{a}^2}[(\gamma - 1)\tilde{u}^2 - 2\tilde{a}\tilde{u}] & \frac{1}{2\tilde{a}^2}[\tilde{a} - (\gamma - 1)\tilde{u}] & \frac{1}{2\tilde{a}^2}(\gamma - 1) \\ \frac{1}{4\tilde{a}^2}[(\gamma - 1)\tilde{u}^2 + 2\tilde{a}\tilde{u}] & -\frac{1}{2\tilde{a}^2}[\tilde{a} + (\gamma - 1)\tilde{u}] & \frac{1}{2\tilde{a}^2}(\gamma - 1) \end{Bmatrix} \tag{3.73}$$

Using (3.69)-(3.73), Roe's equation (3.62) can be further modified as follows:

$$\begin{aligned}
\frac{\partial \mathcal{Q}}{\partial t} + \tilde{\mathcal{A}}(\mathcal{Q}_l, \mathcal{Q}_r)\frac{\partial \mathcal{Q}}{\partial x} &= 0 \\
\frac{\partial \mathcal{Q}}{\partial t} + \tilde{\mathcal{V}}\tilde{\Lambda}\tilde{\mathcal{V}}^{-1}\frac{\partial \mathcal{Q}}{\partial x} &= 0 \\
\tilde{\mathcal{V}}^{-1}\frac{\partial \mathcal{Q}}{\partial t} + \tilde{\mathcal{V}}^{-1}\tilde{\mathcal{V}}\tilde{\Lambda}\tilde{\mathcal{V}}^{-1}\frac{\partial \mathcal{Q}}{\partial x} &= 0 \\
\frac{\partial \tilde{\mathcal{Q}}}{\partial t} + \tilde{\Lambda}\frac{\partial \tilde{\mathcal{Q}}}{\partial x} &= 0
\end{aligned} \tag{3.74}$$

where $\tilde{\mathcal{Q}} = \tilde{\mathcal{V}}^{-1}\mathcal{Q}$. Lastly, the solution to the end result of (3.74) can be considered:

$$\tilde{\mathcal{Q}} = \begin{Bmatrix} Q_1 \\ Q_2 \\ Q_3 \end{Bmatrix} = \begin{Bmatrix} \text{Constant on } C_1 \\ \text{Constant on } C_2 \\ \text{Constant on } C_3 \end{Bmatrix} \tag{3.75}$$

where C_{1-3} in equation (3.75) are defined as the characteristic curves.

3.6.1 Further Consideration

Once again, consider the semi-discrete FVM Euler equations presented previously:

$$\frac{\partial Q_i}{\partial t} + \frac{\left(F_{i+\frac{1}{2}} - F_{i-\frac{1}{2}}\right)}{\Delta x} = 0 \tag{3.76}$$

Now it can been shown that the flux vector approximation $F_{i+\frac{1}{2}}$ can be modified using the Euler Identity (3.66) and diagonalization (3.69) as:

$$F_{i+\frac{1}{2}} = \mathcal{F}_{i+\frac{1}{2}} = \tilde{\mathcal{A}}\mathcal{Q} = (\tilde{\mathcal{V}}\tilde{\Lambda}\tilde{\mathcal{V}}^{-1})(\tilde{\mathcal{V}}\tilde{\mathcal{Q}})_{i+\frac{1}{2}} = \tilde{\mathcal{V}}\tilde{\Lambda}\tilde{\mathcal{Q}}_{i+\frac{1}{2}} \tag{3.77}$$

In addition to (3.77), $\tilde{\mathcal{Q}}(\mathrm{x}_{i+\frac{1}{2}})$ can be written as:

$$\tilde{\mathcal{Q}}^{n+1}_{i+\frac{1}{2}}(k) = \frac{1}{2}[(\tilde{\mathcal{Q}}_{kl} + \tilde{\mathcal{Q}}_{kr}) + \alpha(\tilde{\mathcal{Q}}_{kl} - \tilde{\mathcal{Q}}_{kr})], \qquad \text{where} \quad k = 1, 2, 3 \quad \alpha = 0, \pm 1 \tag{3.78}$$

Here, α is determined by the corresponding sign (or value if 0) of $\tilde{\lambda}_k$. Further, the final formation of the flux vector approximation $F_{i+\frac{1}{2}}$ can be written as:

$$\begin{aligned} F_{i+\frac{1}{2}} &= \frac{1}{2}[\tilde{\mathcal{V}}\tilde{\Lambda}(\tilde{\mathcal{Q}}_l + \tilde{\mathcal{Q}}_r) + \tilde{\mathcal{V}}|\tilde{\Lambda}|(\tilde{\mathcal{Q}}_l - \tilde{\mathcal{Q}}_r)] \\ &= \frac{1}{2}[\tilde{\mathcal{Q}}\tilde{\Lambda}\tilde{\mathcal{Q}}^{-1}(\mathcal{Q}_l + \mathcal{Q}_r) + \tilde{\mathcal{Q}}|\tilde{\Lambda}|\tilde{\mathcal{Q}}^{-1}(\mathcal{Q}_l - \mathcal{Q}_r)] \\ &= \frac{1}{2}[F_l + F_r + \tilde{\mathcal{Q}}|\tilde{\Lambda}|\tilde{\mathcal{Q}}^{-1}(\mathcal{Q}_l - \mathcal{Q}_r)] \\ &= \frac{1}{2}[F_l + F_r + \tilde{\mathcal{Q}}|\tilde{\Lambda}|\tilde{\mathcal{Q}}^{-1}(\mathcal{Q}^l_{i+\frac{1}{2}} - \mathcal{Q}^r_{i+\frac{1}{2}})] \end{aligned} \tag{3.79}$$

where F_l can be defined as $F(Q^l_{i+\frac{1}{2}})$ and F_r can be defined as $F(Q^r_{i+\frac{1}{2}})$. The final result of (3.79) represents Roe's method for the flux vector F. Here, F is taken to be the exact solution to the approximate Riemann problem and $F_{i+\frac{1}{2}}$ is taken to be the approximate solution to the exact Riemann Problem.

3.7 Temporal Integration

The information presented in this section follows derivations from Saad (2003) [34]. The temporal scheme that will be presented is Gauss-Seidel, as that is the one employed in this thesis. Gauss-Seidel is an inner-iterative technique used for solving systems of linear equations. To derive the basic method, first consider an arbitrary constant matrix $\mathcal{B}$ and arbitrary vectors ϕ and ψ. Together, these can be used to form a system of linear equations. It is important to note that for this method to be feasible, matrix $\mathcal{B}$ must be invertible.

$$\mathcal{B}\phi = \psi \tag{3.80}$$

Consider the $\mathcal{LU}$ decomposition of $\mathcal{B}$, where $\mathcal{L}$ is the lower-triangle portion and $\mathcal{U}$ is the upper-triangle and $\mathcal{B} = \mathcal{L} + \mathcal{U}$. Further, the above equation (3.80) can be rearranged:

$$\mathcal{L}\phi = \psi - \mathcal{U}\phi, \qquad \phi = \mathcal{L}^{-1}(\psi - \mathcal{U}\phi) \tag{3.81}$$

Allowing an iterative scheme with parameter k, the LHS can be set to be the $k+1$ value of ϕ and the RHS can be set to be the k value of ϕ as follows:

$$\phi^{k+1} = \mathcal{L}^{-1}(\psi - \mathcal{U}\phi^{k}) \tag{3.82}$$

Equation (3.82) can further be rearranged through forward substitution and decomposition of matrices ϕ, ψ, $\mathcal{L}$, and $\mathcal{U}$ into their respective components as:

$$\phi_i^{k+1} = \frac{1}{b_{ii}}\left(\psi_i - \sum_{j=1}^{i-1} b_{ij}\phi_j^{k+1} - \sum_{j=1+1}^{N} b_{ij}\phi_j^{k}\right) \tag{3.83}$$

For $i, j = 1, 2, 3, \ldots,$N. Coefficients b_{ii} and b_{ij} are the diagonal and off-diagonal components of the matrix $\mathcal{B}$, respectively. After every iteration of k, ϕ_i^k is updated to ϕ_i^{k+1}. This method of temporal iteration is convenient for reaching steady-state solutions but does not produce time-accurate solutions. The advantages of this include reduced solution storage and exceptionally faster convergence. As a result, solutions produced by this temporal method are not considered useful until convergence is achieved, which is further defined by the residual. The residual of an iterative scheme is the calculation of solution change between iterations. In this case, this can be represented as $\Delta\phi = \phi_i^{k+1} - \phi_i^k$. Additionally, it can be noted that output residual information is commonly given as the L_2 norm of the change of solution. Consider a 1D Euler algorithm, where ϕ contains 3 elements, on a grid with N cells. The L_2 norm of the residual can be found as the root-mean-square of the solution change of each element as:

$$L_2 = \sqrt{\frac{1}{3}\sum_j \frac{1}{N}\sum_i (\Delta\phi_{i,j})^2} \qquad \text{for} \qquad \begin{matrix} i = 1, 2, 3, \ldots, N \\ j = 1, 2, 3 \end{matrix} \tag{3.84}$$

Chapter 4

3D Numerical Formations

The entire following chapter follows derivations from AeroSoft's Technical Reference Guide [35]. The numerical considerations presented in Chapter 3 provide a outline of how the Navier-Stokes equations are solved numerically in one dimension. However, the governing equation formations required for this research must be made in three dimensions, and viscous, turbulence, and heat addition effects can no longer be ignored. This chapter presents the formation of the Navier-Stokes equations in three dimensions only, where previous numerical considerations such as accuracy, consistency, and stability are considered outside the scope of this thesis. Formations presented in this chapter are done with consideration of the employed flow solver GASPex, where inviscid modeling is first presented and then expanded to viscous and turbulence modeling.

The generalized 3D Navier-Stokes equations can be numerically approximated using the finite volume method (FVM), as presented previously in Chapter 3. Similarly, V represents the control volume, A represents the control surface, and $\hat{\mathbf{n}}$ represents the unit normal vector. Consider a 3D control volume approach, where the conservation of mass, momentum, and energy equations are coupled in the following manner:

$$\frac{\partial}{\partial t}\iiint_V \boldsymbol{\mathcal{Q}}\, dV + \oiint_A (\boldsymbol{\mathcal{F}}(\boldsymbol{\mathcal{Q}}) \cdot \hat{\mathbf{n}})\, dA = \iiint_V \boldsymbol{\mathcal{S}}\, dV \tag{4.1}$$

where terms $\boldsymbol{\mathcal{Q}}$, $\boldsymbol{\mathcal{F}}$, and $\boldsymbol{\mathcal{S}}$ are comprised of the conservative, flux, and source variables for a given formation. For the purposes of this thesis, the gas will be considered perfect and non-equilibrium effects are further ignored. Because of this, the source term $\boldsymbol{\mathcal{S}}$ can be disregarded for most of the derivations presented in this chapter. FVM utilizes the form of the above equation by first allowing a cell-averaged conservative variable term,

$\bar{\boldsymbol{\mathcal{Q}}}$. Additionally, per FVM, the flux integral is approximated with a sum over the faces of each cell. Both of these are shown in the following relations.

$$\bar{\boldsymbol{\mathcal{Q}}} = \frac{1}{V} \iiint_V \boldsymbol{\mathcal{Q}} \, dV, \qquad \oiint_A (\boldsymbol{\mathcal{F}}(\boldsymbol{\mathcal{Q}}) \cdot \hat{\mathbf{n}}) \, dA \approx \sum_A (\boldsymbol{\mathcal{F}} \cdot \hat{\mathbf{n}}) \, \Delta A \tag{4.2}$$

Together, the generalized 3D FVM formation of the Navier-Stokes equations can be obtained. An additional operation is employed in GASPex in order to solve for primitive variables, rather than conserved, which is done for efficiency purposes. By applying the chain rule to the volume-averaged conservative term $\bar{\boldsymbol{\mathcal{Q}}}$, the time derivative is replaced with respect to the primitive variables. Thus together, the final FVM formation can be shown as:

$$V\left(\frac{\partial \bar{\boldsymbol{\mathcal{Q}}}}{\partial \mathbf{q}}\right)\frac{\partial \mathbf{q}}{\partial t} + \sum_A (\boldsymbol{\mathcal{F}} \cdot \hat{\mathbf{n}}) \, \Delta A = 0 \tag{4.3}$$

While GASPex employs the above FVM method formation for computations, it is more clear to show the inviscid, viscous, and turbulence equations in differential formation. This can be represented by:

$$\frac{\partial \mathbf{Q}}{\partial t} + \frac{\partial \mathbf{F}}{\partial x} + \frac{\partial \mathbf{G}}{\partial y} + \frac{\partial \mathbf{H}}{\partial z} = \mathbf{S} \tag{4.4}$$

where $\mathbf{Q}$ consists of the conservative variables, $\mathbf{F}$, $\mathbf{G}$, and $\mathbf{H}$ consist of the flux variables, and $\mathbf{S}$ consists of the source variables. Collectively, the formation shown in (4.4) represents the conservation of mass, momentum, and energy equations.

4.1 Inviscid Formations

Utilizing the differential formation presented with equation (4.4), formation of the Euler (inviscid) equations can be obtained. As discussed in Chapter 3, this formation can be subsequently solved with flux schemes, such as Roe's. First, consider the differential formation:

$$\frac{\partial \mathbf{Q}}{\partial t} + \frac{\partial \mathbf{F}}{\partial x} + \frac{\partial \mathbf{G}}{\partial y} + \frac{\partial \mathbf{H}}{\partial z} = 0 \tag{4.5}$$

where the inviscid conservative term $\mathbf{Q}$ can be decomposed as:

$$\mathbf{Q} = \begin{Bmatrix} \rho \\ \rho u \\ \rho v \\ \rho w \\ \rho e \end{Bmatrix} \tag{4.6}$$

and the inviscid flux terms $\mathbf{F}$, $\mathbf{G}$, and $\mathbf{H}$ can be decomposed as:

$$\mathbf{F} = \begin{Bmatrix} \rho u \\ \rho u^2 + p \\ \rho uv \\ \rho uw \\ (\rho e + p)u \end{Bmatrix}, \qquad \mathbf{G} = \begin{Bmatrix} \rho v \\ \rho uv \\ \rho v^2 + p \\ \rho vw \\ (\rho e + p)v \end{Bmatrix}, \qquad \mathbf{H} = \begin{Bmatrix} \rho w \\ \rho uw \\ \rho vw \\ \rho w^2 + p \\ (\rho e + p)w \end{Bmatrix} \tag{4.7}$$

The above terms (4.6) and (4.7) consist of fluid density ρ, component velocities u, v, and w, total energy per unit mass e, and pressure p. As mentioned, the gas is also assumed perfect and non-equilibrium effects are ignored. To be concise, the presentation shown above can be further condensed using Einstein notation. This allows for the velocity vector to be defined as $u_j = (u_1,u_2,u_3) = u\hat{i} + v\hat{j} + w\hat{k}$ and the position vector to be defined as $x_j = (x_1,x_2,x_3) = x\hat{i} + y\hat{j} + z\hat{k}$. In addition to this, the Dirac delta function δ_{ij} is implemented for formation purposes and defined as follows.

$$\delta_{ij} \begin{cases} 0 & if\ i \neq j \\ 1 & if\ i = j \end{cases} \tag{4.8}$$

Together, the inviscid formation can now be presented with the differential equation:

$$\frac{\partial \mathbf{Q}}{\partial t} + \sum_{j=1}^{3} \frac{\partial \mathbf{F}_j^{inv}}{\partial x_j} = 0 \tag{4.9}$$

where the conservative term $\mathbf{Q}$ and total inviscid flux term $\mathbf{F}_j^{inv}$ can be decomposed as:

$$\mathbf{Q} = \begin{Bmatrix} \rho \\ \rho u \\ \rho v \\ \rho w \\ \rho e \end{Bmatrix}, \qquad \mathbf{F}_j^{inv} = \begin{Bmatrix} \rho u_j \\ \rho u u_j + p\delta_{j1} \\ \rho v u_j + p\delta_{j2} \\ \rho w u_j + p\delta_{j3} \\ (\rho e + p) u_j \end{Bmatrix} \tag{4.10}$$

Lastly, the inviscid flux term seen in the FVM representation (4.2) and (4.3) requires an inner product of the flux vector $\mathbf{F}_j^{inv}$ with the unit normal vector $\hat{\mathbf{n}}$. Allowing $\hat{\mathbf{n}} = (\hat{n}_1,\hat{n}_2,\hat{n}_3)$, this can be shown as:

$$\sum_{A} \mathbf{F}_j^{inv} \cdot \hat{\mathbf{n}} = \mathbf{F}_1^{inv}\hat{n}_1 + \mathbf{F}_2^{inv}\hat{n}_2 + \mathbf{F}_3^{inv}\hat{n}_3 \tag{4.11}$$

where $\mathbf{F}_{1\to3}^{inv}\hat{n}_{1\to3}$ form:

$$\mathbf{F}_1^{inv}\mathbf{n}_1 = \begin{Bmatrix} \rho u\hat{n}_1 \\ (\rho u^2 + p)\hat{n}_1 \\ \rho uv\hat{n}_1 \\ \rho uw\hat{n}_1 \\ (\rho e + p)u\hat{n}_1 \end{Bmatrix}, \ldots \tag{4.12}$$

4.2 Viscous Formations

When discussing the 3D inviscid formation of the Navier-Stokes equations, viscous effects and heat addition are ignored, leading to the compressible Euler equations. While this formation is useful for supersonic applications, ignoring these effects results in loss of important physical phenomena, such as boundary layers. In order to represent truly physical flow, the inviscid formation can simply be expanded to add the viscous and heat addition effects. Consider a slight adjustment in which these effects are represented with viscous flux terms $\mathbf{F}^v$, $\mathbf{G}^v$, and $\mathbf{H}^v$. Consider the differential formation shown in (4.4):

$$\frac{\partial \mathbf{Q}}{\partial t} + \frac{\partial \mathbf{F}}{\partial x} + \frac{\partial \mathbf{G}}{\partial y} + \frac{\partial \mathbf{H}}{\partial z} = 0 \tag{4.13}$$

where the flux terms $\mathbf{F}$, $\mathbf{G}$, and $\mathbf{H}$ can be separated into inviscid and viscous terms as:

$$\mathbf{F} = \mathbf{F}^{inv} - \mathbf{G}^v, \qquad \mathbf{G} = \mathbf{G}^{inv} - \mathbf{G}^v, \qquad \mathbf{H} = \mathbf{H}^{inv} - \mathbf{H}^v \tag{4.14}$$

With this, the conservative term $\mathbf{Q}$ and invscid flux terms $\mathbf{F}^{inv}$, $\mathbf{G}^{inv}$, and $\mathbf{H}^{inv}$ remain the same. The viscous flux terms are comprised of two new components, the viscous shear stress tensor and global heat transfer vector. Just as with the velocity and position vectors, the viscous shear stress tensor and global heat transfer vector can be represented using Einstein notation as τ_{ij} and q_j, respectively. Following this, the viscous shear stress tensor can be defined in the following manner:

$$\tau_{ij} = \begin{bmatrix} \tau_{11} & \tau_{12} & \tau_{13} \\ \tau_{21} & \tau_{22} & \tau_{23} \\ \tau_{31} & \tau_{32} & \tau_{33} \end{bmatrix} = \begin{bmatrix} \tau_{xx} & \tau_{xy} & \tau_{xz} \\ \tau_{yx} & \tau_{yy} & \tau_{yz} \\ \tau_{zx} & \tau_{zy} & \tau_{zz} \end{bmatrix} \tag{4.15}$$

where it is important to note that non-symmetric indices, $i \neq j$, are identical. In addition, global heat transfer can be defined as $q_j = (q_1,q_2,q_3) = q_x\hat{i} + q_y\hat{j} + q_z\hat{k}$. Using

the above relations (4.14) and definitions of viscous shear stress and global heat transfer, the differential formation (4.13) can be represented as:

$$\frac{\partial \mathbf{Q}}{\partial t} + \sum_{j=1}^{3} \frac{\partial \mathbf{F}_j^{inv}}{\partial x_j} = \sum_{j=1}^{3} \frac{\partial \mathbf{F}_j^{v}}{\partial x_j} \tag{4.16}$$

where the additional viscous flux term $\mathbf{F}_j^v$ can be decomposed as:

$$\mathbf{F}_j^v = \begin{Bmatrix} 0 \\ \tau_{1j} \\ \tau_{2j} \\ \tau_{3j} \\ \tau_{ji}u_i - q_j \end{Bmatrix} \tag{4.17}$$

and for clarity, viscous work $\tau_{ji}u_i$ in the energy equation can be written as:

$$\tau_{ji}u_i = \begin{cases} \tau_{xx}u + \tau_{xy}v + \tau_{xz}w, & \text{j=1} \\ \tau_{yx}u + \tau_{yy}v + \tau_{yz}w, & \text{j=2} \\ \tau_{zx}u + \tau_{zy}v + \tau_{zz}w, & \text{j=3} \end{cases} \tag{4.18}$$

Once again, several items can be noted about the above formation. First, the conservative and inviscid flux terms are identical to the inviscid formation. In addition, the new viscous flux term is comprised of elements of momentum transport related to viscous shear stress τ_{ij}, and energy transport related to viscous work $\tau_{ji}u_i$ and global heat transfer q_j. As with the inviscid formation, the amount of species is one (perfect gas) and vibrational non-equilibrium is ignored. Further, the viscous shear stress tensor

Further, the individual representations of each component in the viscous shear stress tensor can be modeled by applying Stokes law for a monatomic Newtonian gas. This allows for the viscous shear stress tensor to be a linear function of the rate of strain. As a result, the diagonal and symmetric off-diagonal viscous shear stresses can be determined with the following relations.

$$\tau_{xx} = \frac{2}{3}\mu\left(2\frac{\partial u}{\partial x} - \frac{\partial v}{\partial y} - \frac{\partial w}{\partial z}\right), \qquad \tau_{xy} = \tau_{yx} = \mu\left(\frac{\partial u}{\partial y} + \frac{\partial v}{\partial x}\right),$$

$$\tau_{yy} = \frac{2}{3}\mu\left(2\frac{\partial v}{\partial y} - \frac{\partial u}{\partial x} - \frac{\partial w}{\partial z}\right), \qquad \tau_{xz} = \tau_{zx} = \mu\left(\frac{\partial u}{\partial z} + \frac{\partial w}{\partial x}\right), \tag{4.19}$$

$$\tau_{zz} = \frac{2}{3}\mu\left(2\frac{\partial w}{\partial z} - \frac{\partial u}{\partial x} - \frac{\partial v}{\partial y}\right), \qquad \tau_{yz} = \tau_{zy} = \mu\left(\frac{\partial v}{\partial z} + \frac{\partial w}{\partial y}\right)$$

The global heat transfer vector q_j can be decomposed just as with the viscous shear stress tensor. By applying Fourier's law, global heat transfer can be represented as the conduction of energy due to temperature gradients as:

$$q_j = -k\frac{\partial T}{\partial x_j} \tag{4.20}$$

Viscosity and thermal conductivity seen in equations (4.19) and (4.20) must further be modeled. Sutherland's model first assumes that viscosity and thermal conductivity are a function of temperature. Following this, these quantities can expressed as:

$$\mu = \mu_0\left(\frac{T}{T_0}\right)^{\frac{3}{2}}\frac{T_0 + S}{T + S}, \qquad k = k_0\left(\frac{T}{T_0}\right)^{\frac{3}{2}}\frac{T_0 + S}{T + S}, \tag{4.21}$$

where the constants μ_0, k_0, T_0, and S depend on the species.

4.3 Turbulence Formation

The information presented in this section additionally includes derivations from Wilcox (2006) [9]. The 3D Navier-Stokes turbulence formation requires significantly more insight and methodology than previous formations. First, consider the differential formation presented for the viscous formation, with inclusion source terms $\mathbf{S}$:

$$\frac{\partial \mathbf{Q}}{\partial t} + \sum_{j=1}^{3}\frac{\partial \mathbf{F}_j^{inv}}{\partial x_j} = \sum_{j=1}^{3}\frac{\partial \mathbf{F}_j^{v}}{\partial x_j} + \mathbf{S} \tag{4.22}$$

where the conservative $\mathbf{Q}$, inviscid flux $\mathbf{F}_j^{inv}$, and viscous flux $\mathbf{F}_j^v$ terms are first set to be the identical to the previously presented laminar formations. The source term $\boldsymbol{\mathcal{S}}$ will represent turbulent production and dissipation that arise further in the derivation. In order to incorporate the effects of turbulence, the the conservative and flux terms in formation (4.22) must be modified. First, allow (4.22) to represent the instantaneous turbulent equations. With this, the associated variables can then be further decomposed into their respective mean and fluctuating portions. This results in a statistical approach to turbulence, known Reynolds/Favre-averaging. Application of this approach is utilized to develop the Reynolds-averaged Navier-Stokes (RANS) equations, which can further be modified by various turbulence models.

4.3.1 Reynolds and Favre Averaging

Reynolds proposed the following methods of averaging that are utilized to form the RANS equations, which are further expanded by Favre-averaging in the Favre-averaged Navier-Stokes equations. Three fundamentally different types of averaging are considered, which include time-averaging, spatial averaging, and ensemble averaging. These averages can be shown as follows.

$$\begin{aligned}
\bar{\phi}(\mathbf{x}) &= \lim_{\Delta t \to \infty} \frac{1}{\Delta t} \int_t^{t+\Delta t} \phi(\mathbf{x}, t) dt \qquad \text{Time Average} \\
\bar{\phi}(t) &= \frac{1}{V} \iiint_V \phi(\mathbf{x}, t) dV \qquad \text{Spatial Average} \\
\bar{\phi}(\mathbf{x}, t) &= \lim_{N \to \infty} \frac{1}{N} \sum_{n=1}^{N} \phi_n(\mathbf{x}, t) \qquad \text{Ensemble Average}
\end{aligned} \tag{4.23}$$

In order to derive the Favre-averaged equations, time-averaging is utilized, where spatial and ensemble averages are not considered. Additionally, another type of averaging introduced by Favre is employed, known as mass-averaging, which can be shown as:

$$\tilde{\phi}_i = \frac{1}{\bar{\rho}} \lim_{\Delta t \to \infty} \frac{1}{\Delta t} \int_t^{t+\Delta t} \rho(\mathbf{x}, \tau)\ \phi_i(\mathbf{x}, \tau)\ d\tau \tag{4.24}$$

Following (4.23) and (4.24), associated variables in the terms of formation (4.22) are decomposed into their mean and fluctuating portions. Here, the mean for most of the variables is obtained using mass-averaging (Favre); however, the averaging of ρ, p, and q is done using a conventional mean. These variables can be decomposed as:

$$\begin{aligned} u = \tilde{u} + u'', \qquad \rho = \bar{\rho} + \rho', \qquad p = \bar{p} + p', \qquad h = \tilde{h} + h'', \\ e = \tilde{e} + e'', \qquad T = \tilde{T} + T'', \qquad q = \bar{q} + q' \end{aligned} \tag{4.25}$$

where h represents total enthalpy.

4.3.2 Favre-Averaged Navier-Stokes Equations

Following Reynolds/Favre-averaging, the variables associated with conservation of mass, momentum, and energy equations can be decomposed. After, equations are time-averaged and simplified to obtain a usable statistical formation. Rather than using the notation seen in Sections 4.1 and 4.2, this will be shown using the conventional differential form for clarity. Presented below, the starting equations represent the instantaneous continuity equation (4.26), momentum equation (4.27), and energy equation (4.28).

$$\frac{\partial \rho}{\partial t} + \frac{\partial \rho u_j}{\partial x_j} = 0 \tag{4.26}$$

$$\frac{\partial \rho u_i}{\partial t} + \frac{\partial (\rho u_i u_j + p\delta_{ij})}{\partial x_j} = \frac{\partial \tau_{ij}}{\partial x_j} \tag{4.27}$$

$$\frac{\partial \rho e}{\partial t} + \frac{\partial (\rho e u_j + p u_j)}{\partial x_j} = \frac{\partial (\tau_{ji} u_i - q_j)}{\partial x_j} \tag{4.28}$$

The Continuity Equation

$$\frac{\partial \rho}{\partial t} + \frac{\partial \rho u_j}{\partial x_j} = 0 \tag{4.29}$$

$$\frac{\partial \bar{\rho}}{\partial t} + \frac{\partial \overline{\rho u_j}}{\partial x_j} = 0 \tag{4.30}$$

$$\frac{\partial \bar{\rho}}{\partial t} + \frac{\partial \bar{\rho} \tilde{u}_j}{\partial x_j} = 0 \tag{4.31}$$

The Momentum Equation

$$\frac{\partial \rho u_i}{\partial t} + \frac{\partial (\rho u_i u_j + p\delta_{ij})}{\partial x_j} = \frac{\partial \tau_{ij}}{\partial x_j} \tag{4.32}$$

$$\frac{\partial \overline{\rho u_i}}{\partial t} + \frac{\partial (\overline{\rho u_i u_j} + \bar{p}\delta_{ij})}{\partial x_j} = \frac{\partial \bar{\tau}_{ij}}{\partial x_j} \tag{4.33}$$

$$\frac{\partial \bar{\rho} \tilde{u}_i}{\partial t} + \frac{\partial (\bar{\rho} \tilde{u}_i \tilde{u}_j + \overline{\rho u_i'' u_j''} + \bar{p}\delta_{ij})}{\partial x_j} = \frac{\partial \bar{\tau}_{ij}}{\partial x_j} \tag{4.34}$$

$$\frac{\partial \bar{\rho} \tilde{u}_i}{\partial t} + \frac{\partial (\bar{\rho} \tilde{u}_i \tilde{u}_j + \bar{\rho} \widetilde{u_i'' u_j''} + \bar{p}\delta_{ij})}{\partial x_j} = \frac{\partial \bar{\tau}_{ij}}{\partial x_j} \tag{4.35}$$

The Energy Equation

$$\frac{\partial \rho e}{\partial t} + \frac{\partial (\rho e u_j + p u_j)}{\partial x_j} = \frac{\partial (\tau_{ji} u_i - q_j)}{\partial x_j} \tag{4.36}$$

$$\frac{\partial \overline{\rho e}}{\partial t} + \frac{\partial (\overline{\rho e u_j} + \overline{p u_j})}{\partial x_j} = \frac{\partial (\overline{\tau_{ji} u_i} - \bar{q}_j)}{\partial x_j} \tag{4.37}$$

$$\frac{\partial \bar{\rho} \tilde{e}}{\partial t} + \frac{\partial (\bar{\rho} \tilde{e} \tilde{u}_j + \overline{\rho e'' u_j''} + \overline{p u_j})}{\partial x_j} = \frac{\partial (\overline{\tau_{ji} u_i} - \bar{q}_j)}{\partial x_j} \tag{4.38}$$

$$\frac{\partial \bar{\rho} \tilde{e}}{\partial t} + \frac{\partial (\bar{\rho} \tilde{e} \tilde{u}_j + \bar{\rho} \widetilde{e'' u_j''} + \overline{p u_j})}{\partial x_j} = \frac{\partial (\overline{\tau_{ji} u_i} - \bar{q}_j)}{\partial x_j} \tag{4.39}$$

Additionally, the mass-averaged total energy per unit mass $\tilde{e}$ and constitutive ideal gas relationship have been modified and can be represented by the following relations.

$$\tilde{e} = c_v\tilde{T} + \frac{1}{2}\tilde{u}_j\tilde{u}_j + \frac{1}{2}\widetilde{u_j''u_j''}, \qquad \bar{p} = \bar{\rho}R\tilde{T} \tag{4.40}$$

The statistical turbulent differential formation for each conservation equation is shown as the final line of each derivation (4.31), (4.35), and (4.39). Collectively, the conservation of mass, momentum, and energy equations are presented as follows.

$$\frac{\partial\bar{\rho}}{\partial t} + \frac{\partial\bar{\rho}\tilde{u}_j}{\partial x_j} = 0 \tag{4.41}$$

$$\frac{\partial\bar{\rho}\tilde{u}_i}{\partial t} + \frac{\partial}{\partial x_j}(\bar{\rho}\tilde{u}_i\tilde{u}_j + \bar{\rho}\widetilde{u_i''u_j''} + \bar{p}\delta_{ij}) = \frac{\partial\bar{\tau}_{ij}}{\partial x_j} \tag{4.42}$$

$$\frac{\partial\bar{\rho}\tilde{e}}{\partial t} + \frac{\partial}{\partial x_j}(\bar{\rho}\tilde{e}\tilde{u}_j + \bar{\rho}\widetilde{e''u_j''} + \overline{pu_j}) = \frac{\partial}{\partial x_j}(\overline{\tau_{ji}u_i} - \bar{q}_j) \tag{4.43}$$

which marks final formation of the RANS/Favre equations. In equations (4.41)-(4.43), $\tilde{u}_i$ and $\tilde{e}$ are Favre-averaged primitive variables, where $\bar{\rho}$ and $\bar{p}$ are the time-averaged variables. In addition, $\bar{\tau}_{ij}$ denotes the time-averaged viscous stress tensor and $\bar{q}_j$ denotes the time-averaged heat flux. Several additional terms that arise in Favre-averaging have the following denotations. In the momentum equation, $\bar{\rho}\widetilde{u_i''u_j''}$ is referred to as the Reynolds Stress tensor and $\overline{pu_j}$ is the time-averaged pressure-velocity moment. In the energy equation, $\bar{\rho}\widetilde{e''u_j''}$ is considered the turbulent transfer of heat and $\overline{\tau_{ji}u_i}$ is the time-averaged viscous shear-velocity moment.

4.3.3 Two-Equation Modeling (κ-ω)

The statistical conservation equations (4.41)-(4.43) are still considered open and require further modeling and simplification to be closed. As outlined in the introduction, there

are many types of turbulence models that can achieve this. With this said, the two-equation κ - ω model will be presented. The modifications and approximations made to these equations are further tabulated on the next page in Table 4.1.

Viscous Shear-Stress	$\bar{\tau}_{ij} = \tilde{\tau_{ij}} + \bar{\tau}''_{ij}$
Viscous Shear-Stress	$\tilde{\tau}_{ij} \approx \mu\left(\frac{\partial \tilde{u}_i}{\partial x_j} + \frac{\partial \tilde{u}_j}{\partial x_i}\right) - \lambda\mu\frac{\partial \tilde{u}_k}{\partial x_k}\delta_{ij}$
Shear-Stress Fluctuations	$\tau''_{ij} = \mu\left(\frac{\partial u''_i}{\partial x_j} + \frac{\partial u''_j}{\partial x_i}\right) - \lambda\mu\frac{\partial u''_k}{\partial x_k}\delta_{ij} \quad \& \quad \bar{\tau}''_{ij} \approx 0$
Turbulent Kinetic Energy	$\kappa = \frac{1}{2}\widetilde{u''_j u''_j}$
Boussinesq Approximation	$\bar{\rho}\widetilde{u''_i u''_j} = \mu_t\left(\frac{\partial \tilde{u}_i}{\partial x_j} + \frac{\partial \tilde{u}_j}{\partial x_i} - \lambda\delta_{ij}\frac{\partial \tilde{u}_k}{\partial x_k}\right) - \lambda\delta_{ij}\bar{\rho}\kappa$
Heat Flux	$\bar{q}_j = -\overline{k\frac{\partial T}{\partial x_j}} \approx -k\frac{\partial \tilde{T}}{\partial x_j},$
Pressure-Velocity Moment	$\overline{pu_j} = \bar{p}\tilde{u}_j + \bar{\rho}\widetilde{RT''u''_j}$
Viscous Shear-Velocity Moment	$\overline{\tau_{ji}u_i} = \tilde{\tau_{ji}}\tilde{u}_i + \tilde{\tau}_{ji}\bar{u}''_i, \quad \text{as} \quad \overline{\tau''_{ji}u''_i},\ \bar{\tau}''_{ji}\tilde{u}_i \approx 0$
Turbulent Transport of Heat	$\bar{\rho}\widetilde{e''u''_j} = \bar{\rho}C_v\widetilde{T''u''_j} + \bar{\rho}\tilde{u}_i\widetilde{u''_j u''_i} + \frac{1}{2}\bar{\rho}\widetilde{u''_i u''_i}u''_j$
	$\widetilde{T''u''_j} = -\frac{\mu_t}{\bar{p}Pr_t}\frac{\partial \tilde{T}}{\partial x_j} \quad \& \quad \frac{1}{2}\bar{\rho}u''_i\widetilde{u''_i u''_j} = -\sigma^*\mu_t\frac{\partial \kappa}{\partial x_j}$
Enthalpy	$\bar{\rho}\tilde{e}\tilde{u}_j + \bar{p}\tilde{u}_j = \bar{\rho}\tilde{h}\tilde{u}_j$
Turbulent Prandtl Number	$Pr_t = \frac{\nu_t}{\alpha_t} = C_p\frac{\mu_t}{k_t}, \quad \text{where} \quad k_t = C_p\frac{\mu_t}{Pr_t}$
Further Simplifications	$\bar{\rho}C_v\widetilde{T''u''_j} + \bar{\rho}R\widetilde{T''u''_j} = \bar{\rho}(C_v + R)\widetilde{T''u''_j}$
	$= -\bar{\rho}C_p\left(\frac{\mu_t}{\bar{\rho}Pr_t}\frac{\partial \tilde{T}}{\partial x_j}\right) = -k_t\frac{\partial \tilde{T}}{\partial x_j}$
Two-Equation Approximation	$\tilde{\tau}_{ji}\bar{u}''_i - \frac{1}{2}\bar{\rho}\widetilde{u''_i u''_i}u''_j = (\mu + \sigma^*\mu_t)\frac{\partial \kappa}{\partial x_j}$

Table 4.1: Modeling of Favre-Averaged Navier-Stokes Equations

The two-equation considerations can now be utilized to modify the previous statistical conservation equations (4.41)-(4.43). Collectively, the modified statistical conservation of mass, momentum, and energy equations (differential form) are presented below.

$$\frac{\partial \bar{\rho}}{\partial t} + \frac{\partial \bar{\rho}\tilde{u}_j}{\partial x_j} = 0 \tag{4.44}$$

$$\frac{\partial \bar{\rho}\tilde{u}_i}{\partial t} + \frac{\partial}{\partial x_j}(\bar{\rho}\tilde{u}_i\tilde{u}_j + \bar{p}\delta_{ij}) = \frac{\partial}{\partial x_j}(\tilde{\tau}_{ij} - \bar{\rho}\widetilde{u_i'' u_j''}) \tag{4.45}$$

$$\frac{\partial \bar{\rho}\tilde{e}}{\partial t} + \frac{\partial \bar{\rho}\tilde{h}\tilde{u}_j}{\partial x_j} = \frac{\partial}{\partial x_j}\Big[\tilde{u}_i(\tilde{\tau}_{ji} - \bar{\rho}\widetilde{u_j'' u_i''})\Big] + \frac{\partial}{\partial x_j}\Big[(\mu + \sigma^*\mu_t)\frac{\partial \kappa}{\partial x_j} - \bar{q}_j\Big] \tag{4.46}$$

The modified viscous shear-stress tensor can be coupled with the Reynolds stress as $\mathcal{T}_{ij} = \tilde{\tau}_{ij} - \bar{\rho}\widetilde{u_i'' u_j''}$ and decomposed into its respective components (including $\lambda = 2/3$):

$$\begin{aligned}
\mathcal{T}_{xx} &= \frac{2}{3}(\mu + \mu_t)\left(2\frac{\partial \tilde{u}}{\partial x} - \frac{\partial \tilde{v}}{\partial y} - \frac{\partial \tilde{w}}{\partial z}\right) - \frac{2}{3}\bar{\rho}\kappa, \qquad \mathcal{T}_{xy} = (\mu + \mu_t)\left(\frac{\partial \tilde{u}}{\partial y} + \frac{\partial \tilde{v}}{\partial x}\right), \\
\mathcal{T}_{yy} &= \frac{2}{3}(\mu + \mu_t)\left(2\frac{\partial \tilde{v}}{\partial y} - \frac{\partial \tilde{u}}{\partial x} - \frac{\partial \tilde{w}}{\partial z}\right) - \frac{2}{3}\bar{\rho}\kappa, \qquad \mathcal{T}_{xz} = (\mu + \mu_t)\left(\frac{\partial \tilde{u}}{\partial z} + \frac{\partial \tilde{w}}{\partial x}\right), \\
\mathcal{T}_{zz} &= \frac{2}{3}(\mu + \mu_t)\left(2\frac{\partial \tilde{w}}{\partial z} - \frac{\partial \tilde{u}}{\partial x} - \frac{\partial \tilde{v}}{\partial y}\right) - \frac{2}{3}\bar{\rho}\kappa, \qquad \mathcal{T}_{yz} = (\mu + \mu_t)\left(\frac{\partial \tilde{v}}{\partial z} + \frac{\partial \tilde{w}}{\partial y}\right)
\end{aligned} \tag{4.47}$$

where off-diagonal components of $\mathcal{T}_{ij}$ are still symmetric (e.g. $\mathcal{T}_{xy} = \mathcal{T}_{yx}$). As with the viscous formation, the modified heat transfer vector $\bar{q}_j$ can also be decomposed as:

$$\bar{q}_x = -(k + k_t)\frac{\partial \tilde{T}}{\partial x}, \qquad \bar{q}_y = -(k + k_t)\frac{\partial \tilde{T}}{\partial y}, \qquad \bar{q}_z = -(k + k_t)\frac{\partial \tilde{T}}{\partial z} \tag{4.48}$$

Lastly, the total energy $\tilde{e}$ relation shown in (4.40) can now be shown with relation to turbulent kinetic energy κ as follows.

$$\tilde{e} = c_v\tilde{T} + \frac{1}{2}\tilde{u}_j\tilde{u}_j + \kappa \tag{4.49}$$

Two-equation models incorporate additional turbulent variables for computation. First, the eddy viscosity, denoted μ_t, is modeled by turbulent kinetic energy κ, dissipation ϵ, and frequency ω, in the following manner.

$$\mu_t\big|_{\kappa-\epsilon} = \frac{\bar{\rho}\kappa^2}{\epsilon}, \qquad \mu_t\big|_{\kappa-\omega} = \frac{\bar{\rho}\kappa}{\omega} \tag{4.50}$$

The relations and approximations made in this section give rise to what are know as closure coefficients that are needed in order to close the turbulence formation. First, the turbulent Prandtl number Pr_t, which represents the ratio of diffusion of momentum to diffusion of heat, can be obtained with the empirical relations. Subsequently, the laminar and turbulent Prandtl numbers can be expressed for air as:

$$Pr = \frac{C_p\mu}{\kappa} \approx 0.72, \qquad Pr_t = \frac{C_p\mu_t}{\kappa_t} \approx 0.9 \tag{4.51}$$

The other closure coefficient seen above is σ^*. For the Wilcox κ-ω model, this coefficient is set to 3/5. With introduction of additional transport equations, multiple new closure coefficients will be introduced.

4.3.4 Additional Transport Equations

The arise of the turbulent quantities κ, ϵ and ω in two-equation modeling requires additional transport equations for computation. For the Wilcox κ - ω model, these two equations are known as the Turbulent Kinetic Energy (TKE) equation and Turbulent Frequency Energy (TFE) equation. The TKE and TFE equations take the same formation of the conservative equations, with the inclusion of additional source terms, shown as production and dissipation. The TKE equation is first required to solve for turbulent kinetic energy κ. This equation, shown in differential form, can be represented as:

$$\frac{\partial\bar{\rho}\kappa}{\partial t} + \frac{\partial\bar{\rho}\kappa\tilde{u}_j}{\partial x_j} = \frac{\partial\tau_j^\kappa}{\partial x_j} + \mathcal{P}_\kappa - \mathcal{D}_\kappa \tag{4.52}$$

where the spatial derivative on the LHS is the convection term, the spatial derivative on the RHS is the diffusion term, $\mathcal{P}_\kappa$ is the production term, and $\mathcal{D}_\kappa$ is the dissipation term. The diffusion, production, and dissipation terms can be represented as:

$$\tau_j^\kappa = (\mu + \sigma^* \mu_t)\frac{\partial \kappa}{\partial x_j}, \qquad \mathcal{P}_\kappa = \mu_t S^2 - \frac{2}{3}\bar{\rho}\kappa\frac{\partial \tilde{u}_i}{\partial x_j}, \qquad \mathcal{D}_\kappa = \beta^* \bar{\rho}\epsilon \tag{4.53}$$

where the strain invariant S^2, and dissipation rate ϵ, can be shown as:

$$S^2 = \left(\frac{\partial \tilde{u}_i}{\partial x_j} + \frac{\partial \tilde{u}_j}{\partial x_i}\right)\frac{\partial \tilde{u}_i}{\partial x_j} - \frac{2}{3}\left(\frac{\partial \tilde{u}_k}{\partial x_k}\right)^2, \qquad \epsilon = \kappa\omega \tag{4.54}$$

The additional closure coefficient introduced in the TKE equation is β^*. For the Wilcox κ-ω model, this coefficient is set to 9/100.

Following the previous derivation, an additional equation known as the TFE equation is required to solve for the turbulent frequency ω. The equation is structured in the same way as the TKE equation, and can be shown in differential form as:

$$\frac{\partial \bar{\rho}\omega}{\partial t} + \frac{\partial \bar{\rho}\omega \tilde{u}_j}{\partial x_j} = \frac{\partial \tau_j^\omega}{\partial x_j} + \mathcal{P}_\omega - \mathcal{D}_\omega \tag{4.55}$$

where the diffusion, production, and dissipation terms can be similarly shown as:

$$\begin{aligned} \tau_j^\omega = (\mu + \sigma\mu_t)\frac{\partial \omega}{\partial x_j}, \qquad \mathcal{P}_\omega &= \alpha\frac{\omega}{\kappa}\left(\mu_t S^2 - \frac{2}{3}\bar{\rho}\kappa\frac{\partial \tilde{u}_i}{\partial x_j}\right), \\ \mathcal{D}_\omega &= \beta\bar{\rho}\epsilon\frac{\omega}{\kappa}, \qquad \epsilon = \kappa\omega \end{aligned} \tag{4.56}$$

The new closure coefficients that arise in the TFE equation are σ, α, σ_d, and β. For the Wilcox κ-ω model, the first two coefficients are set to 1/2 and 13/25, respectively. The second two coefficients are more involved. σ_d is determined by the following relation:

$$\sigma_d = \begin{cases} 0 & \mathcal{G} \leq 0 \\ & \\ \sigma_{d_0} & \mathcal{G} > 0 \end{cases}, \qquad \mathcal{G} = \frac{\partial \kappa}{\partial x_j}\frac{\partial \omega}{\partial x_j}, \qquad \sigma_{d_0} = \frac{1}{8} \tag{4.57}$$

and additionally, β is obtained by the following:

$$\beta = \beta_0 f_b, \qquad \beta_0 = 0.0708, \qquad f_b = \frac{1+85\mathcal{X}_w}{1+100\mathcal{X}_w}, \qquad \mathcal{X}_w = \left|\frac{\Omega_{ij}\Omega_{jk}\hat{S}_{ki}}{(\beta^*\omega)^3}\right|$$
$$\Omega_{ij} = \frac{1}{2}\left(\frac{\partial\tilde{u}_i}{\partial x_j} - \frac{\partial\tilde{u}_j}{\partial x_i}\right), \qquad \hat{S}_{ki} = \frac{1}{2}\left(\frac{\partial\tilde{u}_k}{\partial x_i} + \frac{\partial\tilde{u}_i}{\partial x_k}\right) - \frac{1}{2}\frac{\partial\tilde{u}_m}{\partial x_m}\delta_{ki} \tag{4.58}$$

4.3.5 Final Formation

With implementation of the TKE and TFE equations to the statistical equations (4.44)-(4.46), the complete two-equation turbulence formation can be considered. In addition to the conservative and flux terms, the production and dissipation terms are added as turbulent sources. Closure coefficients follow those presented in the previous subsections. Collectively, the final differential turbulence formation of the Wilcox κ - ω turbulent model can be represented as:

$$\frac{\partial\bar{\rho}}{\partial t} + \frac{\partial\bar{\rho}\tilde{u}_j}{\partial x_j} = 0 \tag{4.59}$$

$$\frac{\partial\bar{\rho}\tilde{u}_i}{\partial t} + \frac{\partial}{\partial x_j}(\bar{\rho}\tilde{u}_i\tilde{u}_j + \bar{p}\delta_{ij}) = \frac{\partial}{\partial x_j}(\tilde{\tau}_{ij} - \bar{\rho}\widetilde{u_i''u_j''}) \tag{4.60}$$

$$\frac{\partial\bar{\rho}\tilde{e}}{\partial t} + \frac{\partial\bar{\rho}\tilde{h}\tilde{u}_j}{\partial x_j} = \frac{\partial}{\partial x_j}\left[\tilde{u}_i(\tilde{\tau}_{ji} - \bar{\rho}\widetilde{u_j''u_i''})\right] + \frac{\partial}{\partial x_j}\left[(\mu+\sigma^*\mu_t)\frac{\partial\kappa}{\partial x_j} - \bar{q}_j\right] \tag{4.61}$$

$$\frac{\partial\bar{\rho}\kappa}{\partial t} + \frac{\partial\bar{\rho}\kappa\tilde{u}_j}{\partial x_j} = \frac{\partial}{\partial x_j}\left[(\mu+\sigma^*\mu_t)\frac{\partial\kappa}{\partial x_j}\right] + \left[\mu_t S^2 - \frac{2}{3}\bar{\rho}\kappa\frac{\partial\tilde{u}_i}{\partial x_j}\right] - \beta^*\bar{\rho}\kappa\omega \tag{4.62}$$

$$\frac{\partial\bar{\rho}\omega}{\partial t} + \frac{\partial\bar{\rho}\omega\tilde{u}_j}{\partial x_j} = \frac{\partial}{\partial x_j}\left[(\mu+\sigma\mu_t)\frac{\partial\omega}{\partial x_j}\right] + \alpha\frac{\omega}{\kappa}\left[\mu_t S^2 - \frac{2}{3}\bar{\rho}\kappa\frac{\partial\tilde{u}_i}{\partial x_j}\right] + \sigma_d\frac{\partial\kappa}{\partial x_j}\frac{\partial\omega}{\partial x_j} - \beta\bar{\rho}\omega^2 \tag{4.63}$$

In conclusion, differential equations (4.59)-(4.63) provide the final turbulence formation employed for this thesis.

Chapter 5

Experimental Study

The following chapter will present the experimental study done as a precursor to this thesis. The study was conducted by CUBRC Internal Research, and subsequently presented at the American Institute of Aeronautics and Astronautics (AIAA) Aviation conference in 2014. The information and data utilized for the research done in this thesis was obtained from this publication [36]. CUBRC, or the Calspan-University of Buffalo Research Center, is a non-profit research and development organization formed in 1983. The mission of CUBRC is to employ developing technology to solve influential and challenging issues that exist among various United States communities, such as Defense and Homeland Security [37].

The experimental study was sponsored by CUBRC Internal Research, NSSEFF grant with University of Minnesota, and AFOSR. The primary purpose of the study was to obtain and document results for use of a blind code validation. In addition to the experiment, post-computational studies were also conducted and published by various contributors. Overall data is collected for several configurations, where the large cone flare and large hollow cylinder are primarily considered. The focus of this thesis is on the large cone flare, where it can be noted that a similar analysis has been done for the large hollow cylinder by Saumil Patel [16]. Data collection includes surface pressure and surface heat transfer measurements in regions of shock-wave boundary-layer interaction (SBLI). The experiments were conducted at various freestream conditions ranging from Mach 5 to 8, in both cold flows and fully turbulent flows with duplicated flight velocities. For the large cone flare, a total of ten different runs were conducted and published. For the purposes of this thesis, the experimental uncertainty for the study is estimated at 5% for surface pressure readings and 10% for surface heat transfer readings.

5.1 Experimental Equipment (CUBRC)

The collective information presented in this section is obtained from CUBRC's main website [37]. CUBRC has multiple testing facilities, employed for various experimental purposes. The LENS AeroThermal and AeroOptic test facility is the main facility associated with this experimental study and is comprised of four LENS, or Large Energy National Shock, wind tunnels. Each tunnel was constructed with a specific focus on major supersonic and hypersonic flow regimes. The current tunnels are the LENS 48-inch Mach 6 to 18 Shock Tunnel, LENS I, LENS II, and LENS XX. The tunnel that was employed for this experimental study was the LENS II Shock/Ludweig Tunnel, constructed for high Reynolds number flows with Mach ranges of 2 through 12.

5.1.1 LENS II

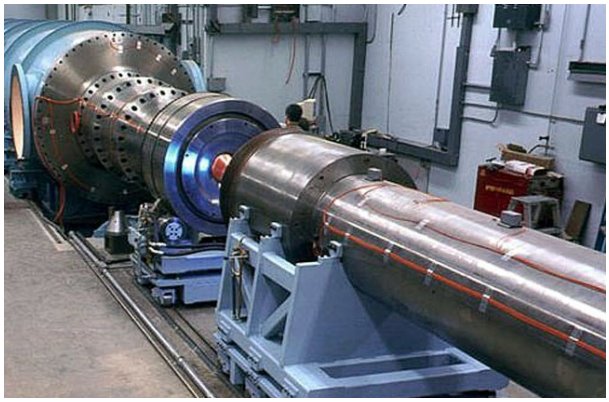

Figure 5.1: LENS II Tunnel [36]

The LENS II High Reynolds Number Shock Tunnel is designed to operated between Mach 2 and 12. In addition, duplicated flight velocities can range from 3,000 to 9,000 ft/sec. LENS II is a very large tunnel with driver and driven tubes that are 60 and 100 ft, respectively. Major tests using LENS II have been conducted at duplicated flight conditions to determine aerothermodynamic loading and propulsion system performance. Fundamental studies of SBLI have been conducted on flight-scale models in high Reynolds number cold flows, as well as high enthalpy flows to provide "flight like" conditions for code-development and calibration. Overall test times can range about 1/3 of a second for low Mach number flows and about 1/10 of a second for higher Mach number flows. Freestream conditions in the LENS II are obtained from pitot pressure probes, stagnation heat transfer gauges, and thermocouple probes for total temperature readings.

5.1.2 Large Cone Flare

The large cone flare design can be related to many supersonic vehicles, such as the nose of jet-propulsion aircraft. This thesis is focused on the experimental study conducted on this specific configuration. To the right, a physical image of the large cone flare is shown inside of the LENS II Tunnel. The total length of the large cone flare is 98.59 inches. The axisymmetric cone exhibits a sharp point at the nose, with a 7° vertex angle. Farther downstream, at 92.64 inches, a second flare exists with a 40° vertex angle. In high Mach number flows, it can be expected that this configuration will produce multiple supersonic phenomena. Most notably is SBLI, which takes place near the surface of the second flare. For computational purposes, the sharp point at the nose is considered to be infinitesimally sharp, with zero thickness. Additionally, considering the size of the configuration, the incoming turbulent boundary layer at the second flare is considered to be fully developed. The overall schematic for the large cone flare is shown below.

Figure 5.2: Large Cone Flare [36]

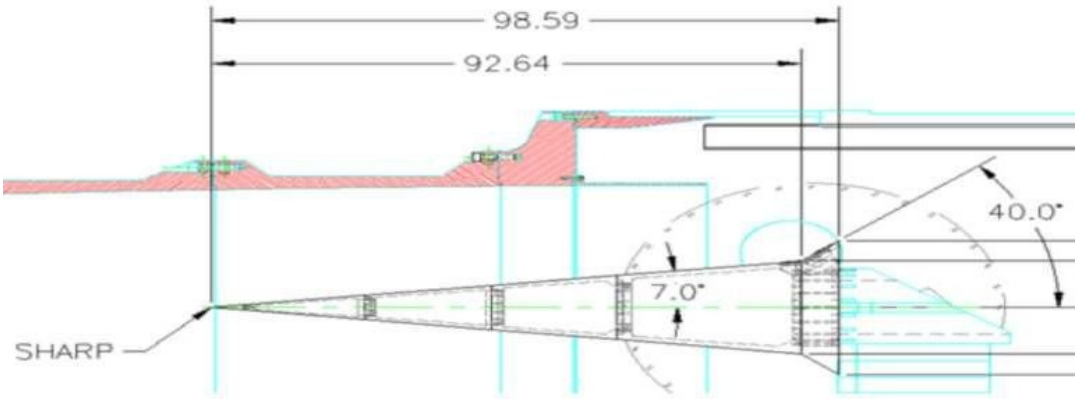

Figure 5.3: Large Cone Flare Schematic [36]

The Large Flare is equipped with numerous surface pressure and surface heat transfer sensors. These sensors include piezoelectric pressure gauges (for surface pressure) and thin-film heat transfer gauges (for surface heat transfer) [38]. A total of 48 pressure sensors are clustered locally along the axial surface near the second flare, ranging from 89 inches (7.46 feet) to 97.6 inches (8.13 feet). Additionally, a total of 86 heat transfer sensors are distributed along the entire axial surface of the cone, ranging from 6.8 inches (.57 feet) to 97.7 inches (8.14 feet). Condensed sensor locations are tabulated below, where sensor denotations for pressure and heat transfer are P# and T#, respectively.

Sensor	Axial Location (inches)	Sensor	Axial Location (inches)
P26	89.607	T1	6.848
P27	89.761	T2	9.892
P28	89.915	T4	15.892
P29	90.069	T96	16.892
P30	90.223	T97	17.892
⋮	⋮	⋮	⋮
P75	96.357	T159	96.548
P76	96.548	T160	96.827
P77	96.827	T161	97.133
P78	97.21	T162	97.44
P79	97.593	T163	97.746

Table 5.1: Pressure and Heat Transfer Sensor Locations

5.2 Experimental Data

Experiments were run with multiple freestream conditions, with Mach number ranges of roughly 5 to 8. These conditions are tabulated for each run and provided on the next page. For computations, six out of the ten runs were selected: Runs 28, 34, 33, 14, 41, and 37. The model surface is approximated to be isothermal with a wall temperature of 300 K, or 540° R. The freestream gas is assumed to be dry air with mass fractions $c_{N2} = 0.765$ and $c_{O2} = 0.235$, and is further approximated as a perfect ideal gas.

Run Number	Mach Number	Velocity ($\frac{ft}{sec}$)	Temperature (R°)	Density ($\frac{slugs}{ft^3}$)
28	4.96	4844.1	395.8	2.75E-04
34	6.03	5177.6	305.8	1.38E-04
33	6.17	3055.3	101.7	1.43E-04
14	7.18	3862.6	119.9	1.11E-04
41	8.10	6898.5	300.5	4.57E-05
37	8.21	4205.9	108.8	8.48E-05

Table 5.2: Freestream Conditions for CUBRC LCF Experiments

5.3 Computational Study

Previous computational studies have been done corresponding to this experimental study. Detailed submissions were received by NASA Langley Research Center, NASA Ames Research Center, University of Minnesota, Texas A&M University, and CUBRC. Simulations from these organizations were carried out by MacLean, Candler, Prabhu, Bowersox, and Gnoffo, respectively. Comparisons that were presented by CUBRC include plots for surface pressure and surface heat transfer in regions of SBLI. The main turbulence models employed for simulations were SST and Spalart-Allmaras. Contributors found very similar results for each respective run for both surface pressure and surface heat transfer. For each run, all contributors produced reasonable pressure predictions, with over-prediction of the region of separation and location of peak pressure. In addition, all contributors produced inaccurate post-flare surface heat transfer predictions, as well as large over-predictions of peak heat transfer. Computational studies were also conducted for the large hollow cylinder, where results show similar inaccuracies. Collectively, the computational results published by these contributors are on-par with the final results for this thesis. All predictive inaccuracies are dually observed, with slight discrepancies due to the employed turbulence model.

Chapter 6

Methodology

There are many commercial software that exist for computational fluid dynamics (CFD). Some examples include GASPex, ANSYS CFX, COMSOL Multiphysics, OpenFoam, and Autodesk Simulation. The commercial software utilized for this thesis is AeroSoft's GASPex. GASPex is multi-physics package that primarily solves the Reynolds-averaged Navier-Stokes (RANS) equations. To be able to utilize GASPex, a grid must first be imported. Once this is done, the graphic user interface (GUI) can be configured in order to produce a fluid-flow simulation. There are numerous specifications that can be made, as well as parameters that can be set. Some examples include boundary conditions, freestream conditions, inviscid flux scheme, and turbulence model. This chapter will present the methodology of this thesis, which includes grid generation and GASPex configuration.

6.1 Grid Generation

GASPex requires a grid to be self-created and imported into the GUI. Multiple grid formats are accepted in GASPex, including Plot3D, CGNS, GASP, FVUns, and VGrid. Plot3D was chosen, however this format requires additional code such as C++ or MATLAB for creation. Due to familiarity, the grid generation code was created using MATLAB. Additionally, because the software utilizes a matrix-base language, it is very easy to create an efficient grid generation code using it.

To create a Plot3D grid, first a basic geometry outline needs to be considered. Using this, the outline needs to be converted into separate zones. For the purposes of GASPex, each zone will allow for different boundary conditions and solution storage. After this, the geometrical outline needs to be converted into a discrete mesh. For the Plot3D format, this is recorded by specifying each individual node's Cartesian location. After this, the mesh needs to be formated in a particular way. The line-by-line formatting of a 2D Plot3D grid with dimensions of N by M is shown to right, in Table 6.1. Figure 6.1, shown below, represents an example grid. For this grid, the number of zones, nodes, and cells are 1, 9, and 4, respectively. The dimensions of this grid are [0,2] by [0,2].

(i)	Number of Zones (α)
(ii)	Dimensions$_{1\rightarrow\alpha}$: N x M
	$\vdots$
(iii)	Cell Coordinates: $x_{i,j}$
	$\vdots$
(iv)	Cell Coordinates: $y_{i,j}$
	$\vdots$
	for i = 1, 2, 3, $\cdots$, N j = 1, 2, 3, $\cdots$, M

Table 6.1: Plot3D Grid Formatting

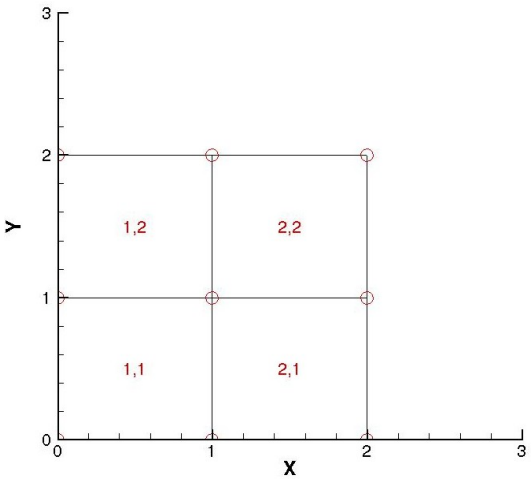

Figure 6.1: Sample Plot3D Grid

For the employed grid configuration, the amount of zones was set set to three. The first zone is the incoming flow region, set to be the inlet flow. Without this first zone, computational instability occurs. The second zone is the main physical region, where the geometry is based on the double cone flare. The last zone is the outlet zone, set to be slightly downstream of the end of the flare and is required for similar reasons as the inlet zone. To create the outline geometry and dimensions for each zone, multiple considerations were taken. First, the second zone is set as the center-zone in which it begins at the origin of the Cartesian grid. The length of this zone is set to the length of double cone flare, which is 98.59 inches (or 8.126 feet). The height of this zone needed special consideration,

as it needed to be tall enough to fully contain all supersonic phenomena. The leading constraint for this is the incoming leading edge shock. The height needed to contain this shock can be approximated by the Mach wave angle μ, which is a function of incoming Mach number. This angle and the corresponding height h, can be found with the following relations: *Note that L = length.*

$$\mu = sin^{-1}\frac{1}{M_\infty}, \qquad \mathrm{h} = \mathrm{L}\tan(\mu) \tag{6.1}$$

It is important to mention that one grid was made to incorporate all runs. Since the incoming Mach angle μ is inversely proportional to Mach number, the lowest run Mach number (Run 28 - Mach 4.96) was used to create the grid. Additionally, a factor of 1.25 was added to the total height to ensure room for uncertainty and approximation error. The dimensions for the incoming and exiting zone are arbitrary in the x-direction, and based on the beginning/ending coordinates of the second zone in the y-direction. The total dimensions for the grid are presented below in Table 6.2, where the second zone is split into the pre, 2a, and post, 2b, flare dimensions. In the table, x-coordinates are always constant and the beginning/ending y-coordinates for each zone are shown as a result of the trapezoidal geometry. Additionally, it should be noted that coordinates in Table 6.2 are rounded, where actual coordinates utilized are double-precision.

Zone	x	y_1	y_2
1	-0.74 $\rightarrow$ 0.00	0.00 $\rightarrow$ 1.46	”
2a	0.00 $\rightarrow$ 7.72	0.00 $\rightarrow$ 1.46	0.95 $\rightarrow$ 2.40
2b	7.72 $\rightarrow$ 8.22	0.95 $\rightarrow$ 2.40	1.36 $\rightarrow$ 2.82
3	8.22 $\rightarrow$ 8.95	1.36 $\rightarrow$ 2.82	”

Table 6.2: Employed Grid Dimensions

Next, the mesh for the grid was created where the overall geometry that was employed follows Table 6.2. The x spatial-direction was discretized in an arbitrary manner at first, and later refined. The y spatial-direction took further consideration. First, a basic mesh was created that had a constant change of height Δy. Here, the starting location for each J-Surface follows basic trigonometry as a function of the flare angle and spatial location. After, viscous effects needed to be considered. Due to the viscous sublayer which needs to be resolved, the y-direction spacing near the wall is required to be extremely small (roughly 10^{-06} inches). If this was kept at a constant change of height, the amount of cells required would be extremely large and computationally expensive. Therefore, two geometric progressions were employed to optimize computational loading. The first geometric progression progressed the surface height location y_w, to about 1/10 of the total surface height y_α, in half of the total nodes. The second geometric progression then progressed y_α to the total height, in the remainder of the points. Arbitrary constants associated with these progressions, C_1 and C_2, are based on the height of each surface and corresponding amount of nodes in the y-direction. After this, the final grid mesh was created, represented in Figure 6.2. It should be noted that considering the large amount of cells for the final grid, Figure 6.2 shows a reduced version of the grid through I/J-Blanking in Tecplot.

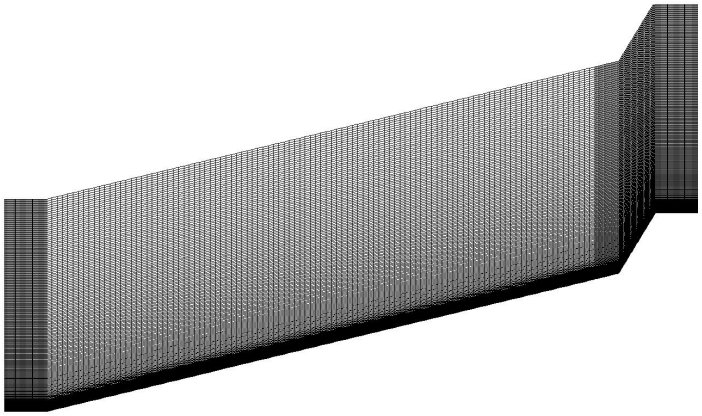

Figure 6.2: Mesh for Large Cone Flare, Plot3D

Throughout the research conducted in this thesis, a grid independence study was also done. The purpose of the study, which will be presented in the Results chapter, was to create a fine enough grid where grid sequencing had a negligible affect on the solution. Before the grid was deemed independent, several configurations were made. Each time a configuration was created, the grid was split into three sequences: course, medium, and fine. Various differing grid configurations were employed to test grid dependence. After several iterations, the final grid configuration was created in which grid sequencing effected the results within the experimental uncertainty and thus deemed independent. The final grid configuration nodal information and sequencing is tabulated in Table 6.2.

Zone	# of Nodes	# of Cells
1	(x): 51.00 (y): 3,009	150,400
2	(x): 3,281 (y): 3,009	9,866,240
3	(x): 51.00 (y): 3,009	150,400

Table 6.3: Finest Grid Mesh Information

6.1.1 2D to Axisymmetric Conversion

A common practice in CFD is simulating 3D configurations with 2D axisymmetric models. It has been seen that basic phenomena and approximations using this method allow for minimal computational resources with low change in results. For the purposes of this thesis, the 2D grid model is converted to a 2D axisymmetric grid. GASPex allows for this conversion to be done when importing a 2D grid automatically. When this is done, the 2D grid is rotated about the axis of symmetry by $\pm \frac{\pi}{80}$, or 2.25°, which creates a total of 2 nodes in the k-direction. Using the solution visualization feature in GASPex, a representation of the employed 2D axisymmetric grid is provided (on the next page).

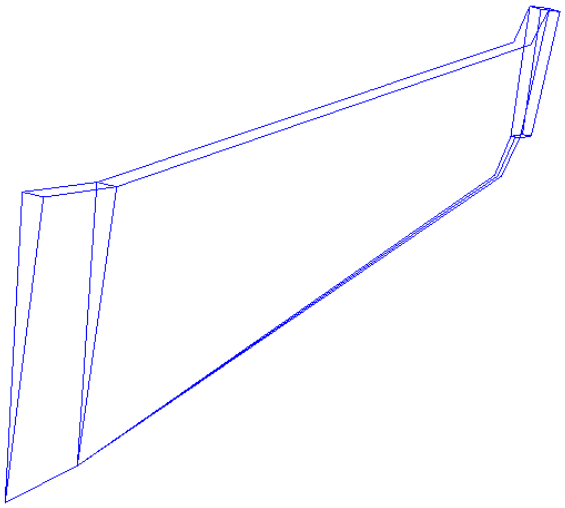

Figure 6.3: GASPex Visualization of Grid

6.2 Solver Configuration

Once a grid is imported, GASPex's input deck must be configured. First, the imported grid can be sequenced either automatically or by user definition. After, the zonal and surface boundary conditions must be specified. Once this is done, the rest of the fluid simulation specifications can be chosen, such as physical models and run definitions.

Grid sequencing is often employed for CFD applications in order to reduce the time taken for simulations. The first initial imported grid, denoted as the fine grid, is subsequently reduced into less-refined meshes. Luckily, additional meshes do not need to be created outside of GASPex, as an in-software grid sequencing mechanism exists. After sequencing, the meshes are consecutively run in reverse order. The first mesh utilizes an initialized flow, in that all flow quantities are set arbitrarily. This can cause issues for temporal convergence, and thus a separate CFL definition is often needed for this mesh. After, the solutions are interpolated to the next, more refined, mesh. This acts as a new initialization, which is much more accurate than the first. A total of three sequences are utilized; which are denoted coarse, medium, and fine. The medium and coarse meshes are sequenced from the fine grid by 1/2 and 1/4, respectively. The method of sequencing and subsequent nodal/cell-information for the medium and coarse

meshes are provided below on Table 6.4.

Zone	Sequence	# of Nodes	# of Cells
1	Medium	(x): 51.00 (y): 1,505	75,200
	Coarse	(x): 51.00 (y): 753.0	37,600
2	Medium	(x): 1,641 (y): 1,505	2,466,560
	Coarse	(x): 821.0 (y): 753.0	616,640
3	Medium	(x): 51.00 (y): 1,505	75,200
	Coarse	(x): 51.00 (y): 753.0	37,600

Table 6.4: Grid Sequencing Information

An important part of CFD is the implication of boundary conditions into any code. GASPex allows for numerous types of physical boundary conditions including solid wall, in/out flow, extrapolation, symmetry, etc. Zonal boundaries are configured with the point-to-point boundary condition, which interpolates solutions between adjacent zones based on distance between corresponding grid cells. The employed grid was created in a way that aligns each individual cell between adjacent zones and therefore should allow for exact transition between each zone. These boundaries are set for the left faces of Zone 2 and 3, as well as the right faces for Zone 1 and 2. The physical boundary conditions that were implemented are additionally tabulated below in Table 6.5. Not included in this table are the boundary conditions set for the K-faces of the axisymmetric conversion, which are automatically set to positive/negative axisymmetric. In Table 6.5, several boundary conditions are listed: *Symmetry plane* is used when symmetrical flow conditions are expected. *Positive/Negative Axisymmetric* specification works in a similar fashion. *Fixed at Q* sets the flow conditions of the boundary to the freestream specifications. *No slip,* $T = T_w$*,* allows for an isothermal physical wall boundary. Lastly, *First-Order Extrapolation* sets boundary values to neighboring flow properties. The two types of turbulent boundaries included are *Inflow/Outflow* and *Default*; which prescribe values for κ/ω at specific boundaries.

Zone	Surface	Boundary Condition	Turbulent B.C.
1	Bottom	Symmetry Plane	N/A
1	Top	Symmetry Plane	N/A
1	Left Side	Fixed at Q	Inflow/Outflow
2	Bottom	No Slip, T=T_w	N/A
2	Top	First-Order Extrapolation	Default
3	Bottom	First-Order Extrapolation	Default
3	Top	First-Order Extrapolation	Default
3	Right Side	First-Order Extrapolation	Inflow/Outflow

Table 6.5: Implemented Boundary Conditions

Another requirement to set up a fluid simulation in GASPex is the configuration of the physical models employed. Information prescribed here includes specifications of thermo-chemistry, freestream conditions, and inviscid, viscous, and turbulence models. The gas model is chosen to be a perfect gas, with frozen chemistry and equilibrium translation and rotation temperatures. The freestream specifications are set to the exact freestream conditions for each run, where freestream temperature, density, and velocity are used as key parameters. The inviscid, viscous, and turbulence modeling definitions employed are as follows.

(i) Inviscid Modeling: Roe scheme, 3rd order upwind bias accuracy ($\kappa = \frac{1}{3}$) with Min-Mod flux limiter.

(ii) Viscous Modeling: Sutherland viscosity and conductivity models.

(ii) Turbulence Modeling: Wilcox κ - ω (2006), default settings with no limiting or compressibility correction.

The last component of the flow solver that needs to be configured is the run definition. Here, temporal integration, convergence criteria, CFL number, and physical resources can be specified for each simulation. Each sequence needs to be individually ran with differing specifications. Re-initialization is done for the coarse sequence

only, where the coarse and medium solutions are further interpolated up to consecutive sequences. Convergence criteria allows for specification of the maximum amount of iteration cycles to be conducted, as well as with exiting convergence parameters. The temporal integration scheme, and associated CFL number/basis, can be further be specified. The temporal scheme employed is Gauss-Seidel inner-iterative. With an iterative scheme such as Gauss-Seidel, convergence criteria needs to be chosen and modified throughout computations in order to definitively reach the steady-state solution. This is done by monitoring the output solution residuals, which were described previously, in detail, at the end of Chapter 3. Essentially, residuals define the solution change between temporal iterations (cycles), and once a certain level is reached, can be used to determine if steady-state has been reached. A basic residual plot is shown below (log-scale) for the first 10,000 iterations of an arbitrary run. It is important to note that GASPex outputs residual as a L_2 norm, normalizing each consecutive sequence by the first iteration's residual value (i.e. the first residual of each sequence is set to one).

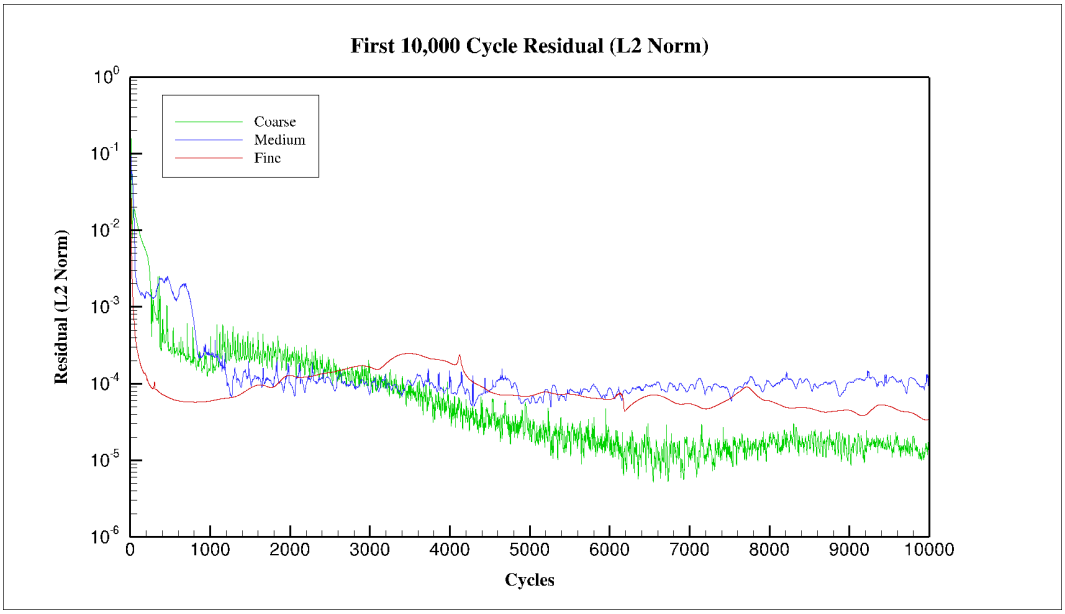

Figure 6.4: First 10,000 Cycle Residual (L2 Norm)

With the Gauss-Seidel temporal scheme, CFL numbers can be set and do not always have to be ≤ 1. CFL numbers can be altered throughout a run, allowing for higher CFL numbers to be utilized. Additionally, the CFL number can be defined by a basis, in which the wave-speed condition can be set to global or local specifications. Local values are needed in order to obtain useful solutions in regions of SBLI; however, freestream specifications may need to be employed in order to avoid instability caused by initialization. The method of CFL progression through each sequence follows in Table 6.6, where it should be noted that differing freestream velocities may require additional modifications.

Sequence	Convergence	CFL Definition	CFL #	Cycles
Coarse	10^{-8}	Q Infinity	0.1 - 1	5,000
			1	5,000
		Q Local	1	10,000
			1-2	5,000
			2	10,000
Medium	10^{-6}	Q Local	1	5,000
			1-2	5,000
			2	10,000
Fine	10^{-5}	Q Local	1	5,000
			1-5	5,000
			5	10,000

Table 6.6: CFL Number and Definition Progression

Specification of computational resources, such as memory per core and total number of cores, is required for each individual simulation. Following this, zonal decomposition must be configured for allocation of these resources. Zonal decomposition allows for all zones to be decomposed into multiple partitions, which allows for parallel efficiency when running across multiple cores/nodes. This needs to be conducted separately for each sequence, or when computational resources employed are modified. To obtain the

computational resources required for this research, the Rutgers School of Engineering (SOE) High Performance Computing (HPC) Cluster was accessed. The SOE HPC Cluster has a total of 60 available nodes, with 16 cores and 128 GB of RAM per each node. The computational resources of the SOE HPC Cluster utilized for each sequence is tabulated below in Table 6.7.

Sequence	Memory per Core	# of Cores	# of Nodes
Coarse	2,000 MB	40	4
Medium	4,000 MB	80	8
Fine	6,000 MB	96	8

Table 6.7: Computational Resources

6.3 Post-Processing

For any CFD simulation, post-processing is required for data analysis. Post-processing can be done with numerous software; however, Tecplot and MATLAB were chosen. MATLAB was used to convert various solutions obtained by GASPex to match with respective experimental data. Tecplot was used for creation of all surface pressure, surface heat transfer, and Mach counter plots presented in the Results chapter. Additionally, Tecplot allows for data manipulation which is used in order to calculated streamlines in the Mach contours. Lastly, it should be noted that extraneous data analysis and manipulations done throughout research, such as evaluation of the obtained results, was conducted using MATLAB.

Chapter 7

Results

The following chapter will present the final results obtained in this research. The main considerations for discussion are surface pressure and surface heat transfer in regions of shock-wave boundary-layer interaction (SBLI). Both grid convergence and experimental comparison plots are provided for each surface variable, where solution change (for grid convergence) and error (for comparison) are included as well. Mach contours of the SBLI region are additionally provided, along with tabulated surface variable data.

The general flowfield of the entire large cone flare can be visualized in a Mach contour using sample results from Run 28, shown below. For this configuration, a leading edge attached oblique shock is formed at the sharp tip. The region of investigation (SBLI) is located at the downstream flare ($\sim$ 89 inches). At the downstream flare, a detached

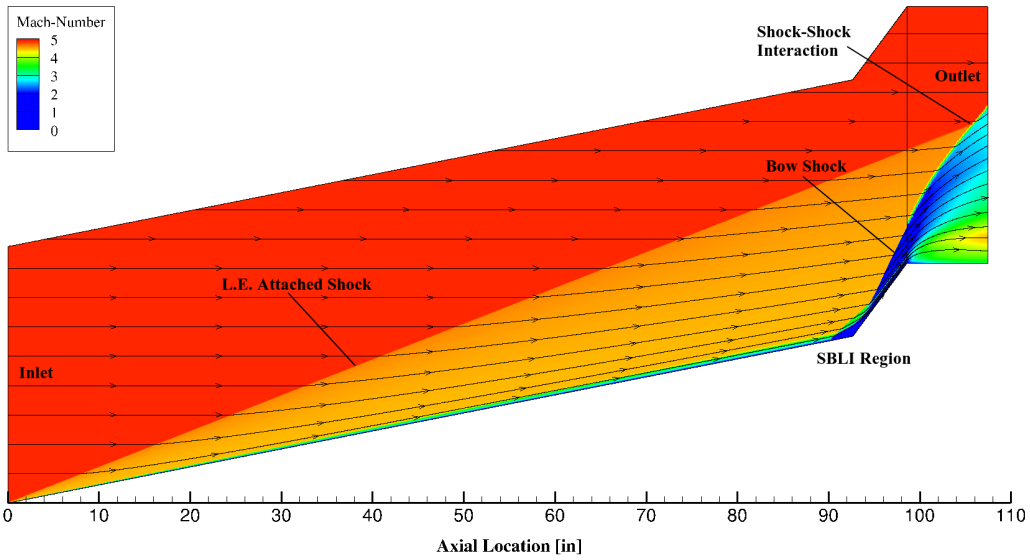

Figure 7.1: Total Flowfield

bow shock (separation shock) can be seen. Further aft, recovery and expansion takes place, and eventually the bow shock and leading edge shock interact causing a shock-shock interaction. However, this interaction is not investigated further and all discussion remains in the SBLI region. This region will be further discussed in the following section.

7.0.1 SBLI Flowfields

While the total flowfield is similar for each run, the SBLI region between runs differs significantly. Due to this, Mach contours for each run will be shown in the following pages (Figure 7.2-7.7). The SBLI region consists of an incoming turbulent boundary layer, recirculation/separation region, and separation/reattachment shocks. The incoming turbulent boundary layer succumbs to an adverse pressure gradient at the flare, causing separation. Separation occurs at roughly 90 inches (2 inches pre-flare), producing a strong separation shock and detached shear layer. The flow eventually reattaches at roughly 95 inches (3 inches post-flare), causing peak surface pressure and surface heat transfer loading, along with an additional reattachment bow shock.

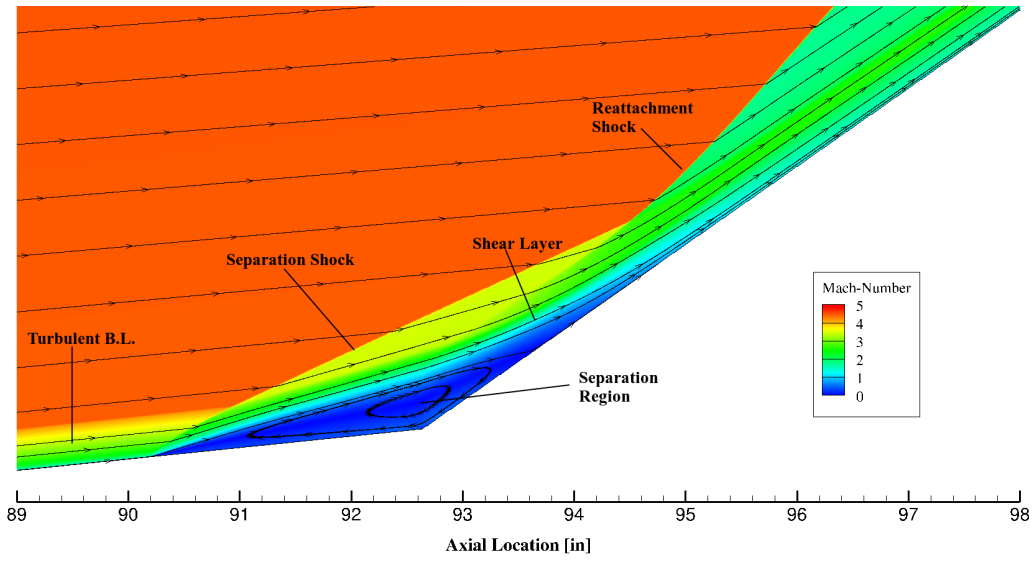

Figure 7.2: Run 28 - Flowfield

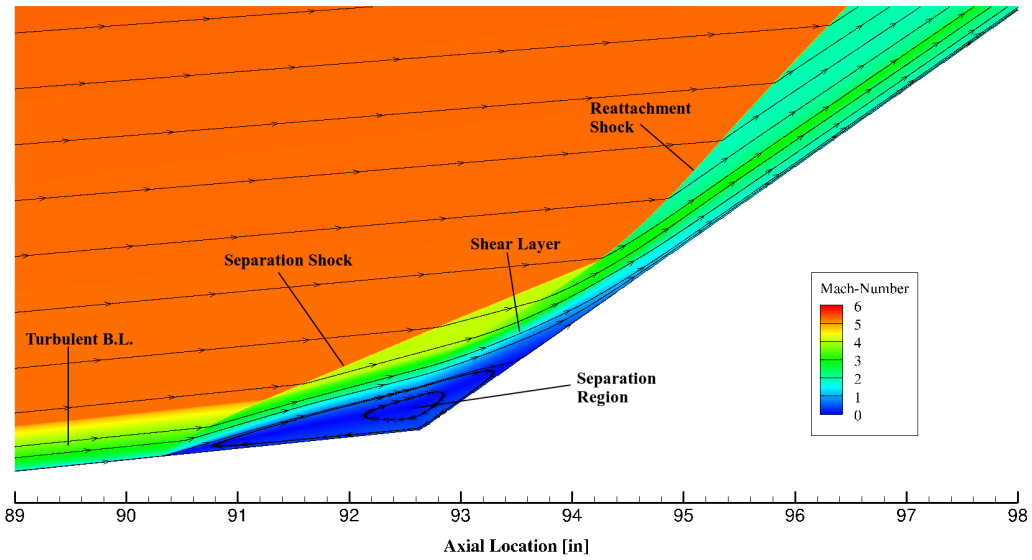

Figure 7.3: Run 34 - Flowfield

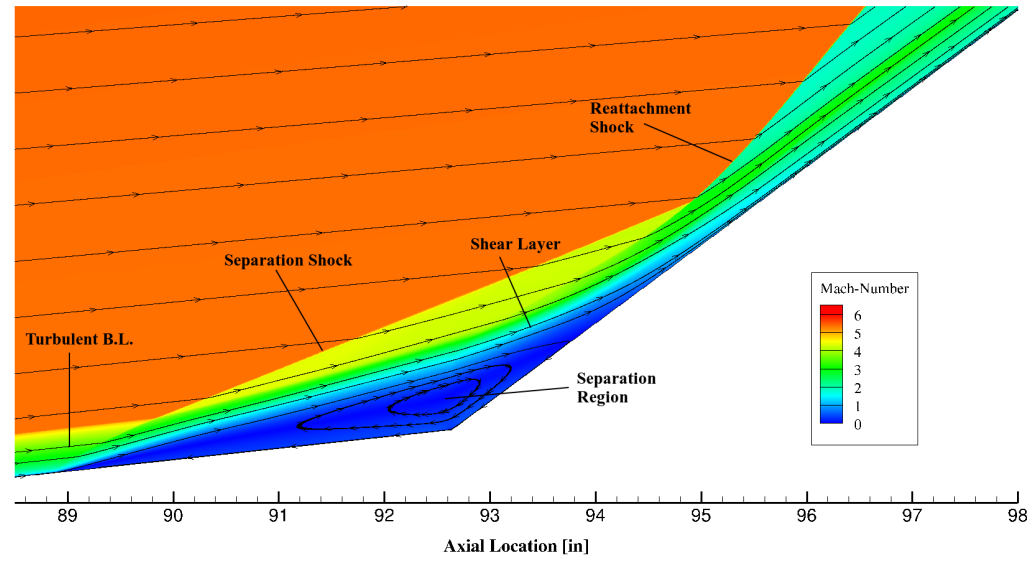

Figure 7.4: Run 33 - Flowfield

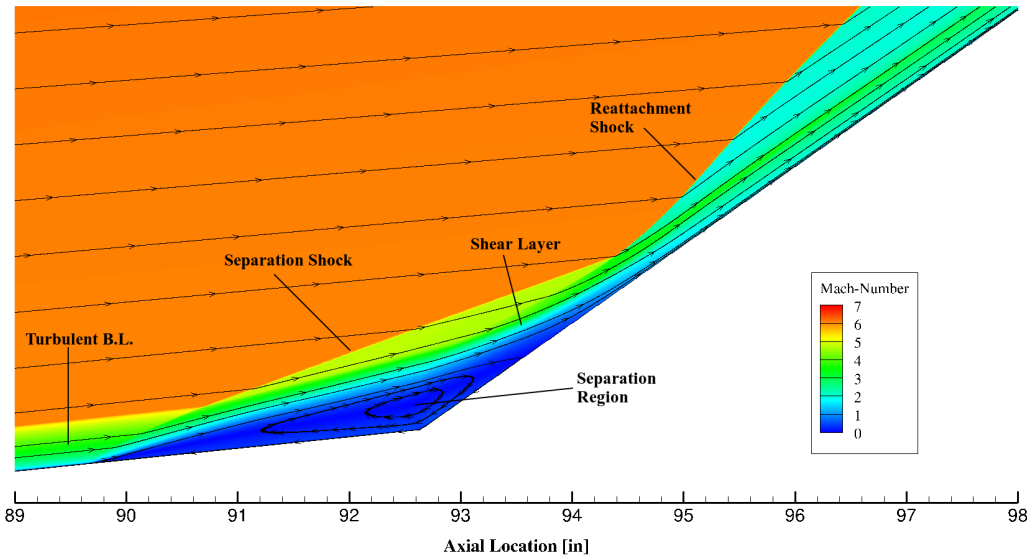

Figure 7.5: Run 14 - Flowfield

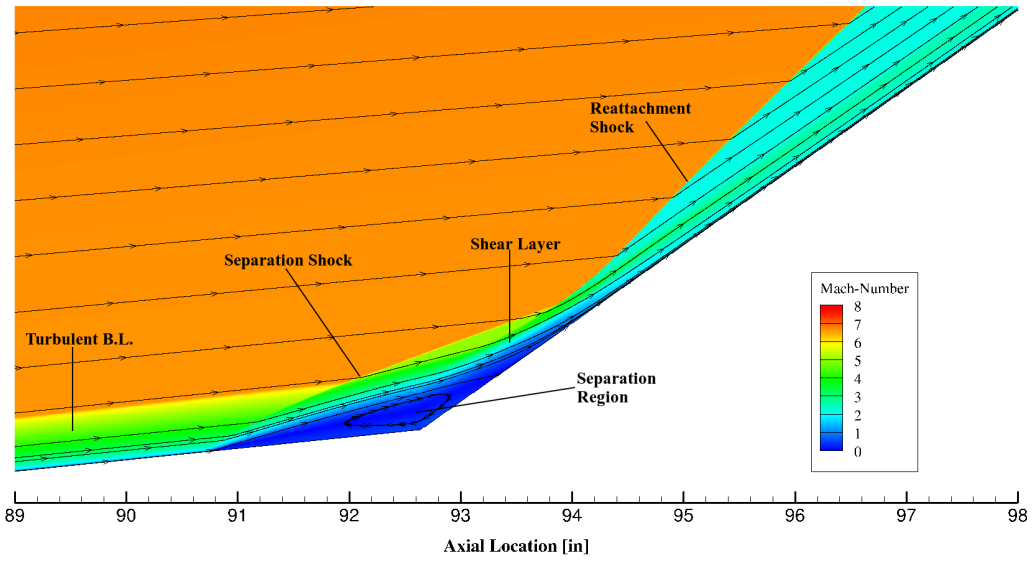

Figure 7.6: Run 41 - Flowfield

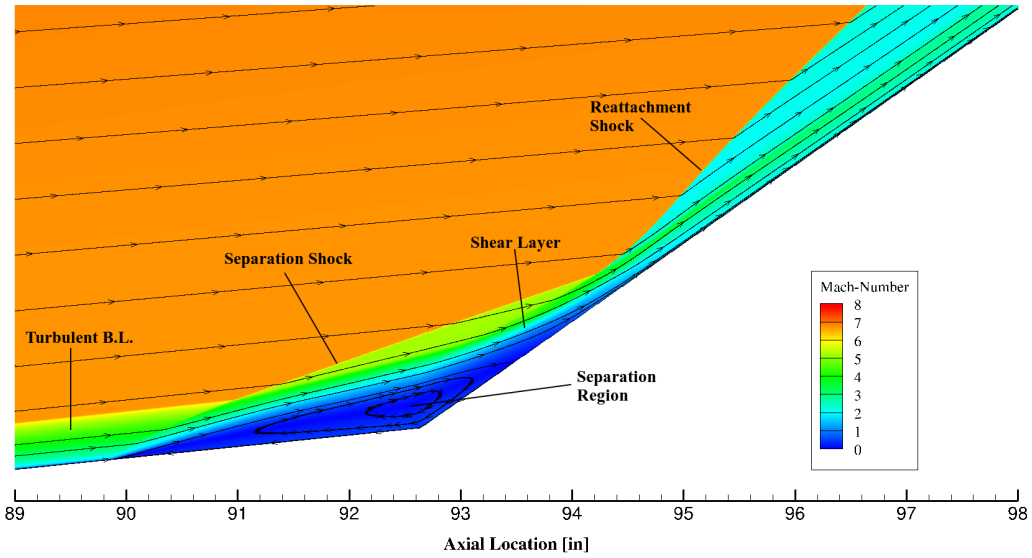

Figure 7.7: Run 37 - Flowfield

7.1 Presentation of Results

Analysis of surface pressure and surface heat transfer results will be presented in separate categories: grid convergence and experimental comparison. The primary focus is on surface variable averages and peak values. Averages are taken in two regions, which are the fore region, ranging from 0 to 89 inches, and the SBLI region, ranging from 89 to 98 inches. Runs are presented with increasing Mach number, in the following order: Run 28, Run 34, Run 33, Run 14, Run 41, and Run 37.

7.1.1 Gird Convergence

Grid convergence is mainly measured by the percent solution change between the medium and fine grids. Surface variable plots for each respective run are provided following discussion and tabulated data is included in "Final Remarks and Tabulated Data". The information presented in this subsection concludes that all solution change values are negligible. With this, it can be asserted that the employed grid can be considered "converged", implying that final results are independent of grid refinement.

1) Surface Pressure

For surface pressure, average fore solution change for all runs is negligible at 0.11%. Average SBLI solution change for all runs is higher, but still within the experimental uncertainty at 3.41%. Minimum fore solution change is found in Run 14 at 0.02% (Figure 7.11), where maximum fore solution change is found in Run 33 at 0.37% (Figure 7.10). Minimum SBLI solution change is found in Run 41 at 2.26% (Figure 7.12), where maximum SBLI solution change is found in Run 33 at 4.25% (Figure 7.10). Peak surface pressure magnitude solution change and location displacement follow similar trends. Average peak solution change is negligible at 1.03% and average peak location displacement can be considered low at 0.11 inches. Minimum peak magnitude solution change is found in Run 28 at 0.47% (Figure 7.8), where maximum peak magnitude solution change is found in Run 37 at 1.76% (Figure 7.13). Minimum peak location displacement is found in Run 41 at 0.05 inches (Figure 7.12), where maximum peak location displacement is found in Run 33 at 0.17 inches (Figure 7.10). Associated surface pressure grid convergence plots are provided on the following pages (Figures 7.8-7.13).

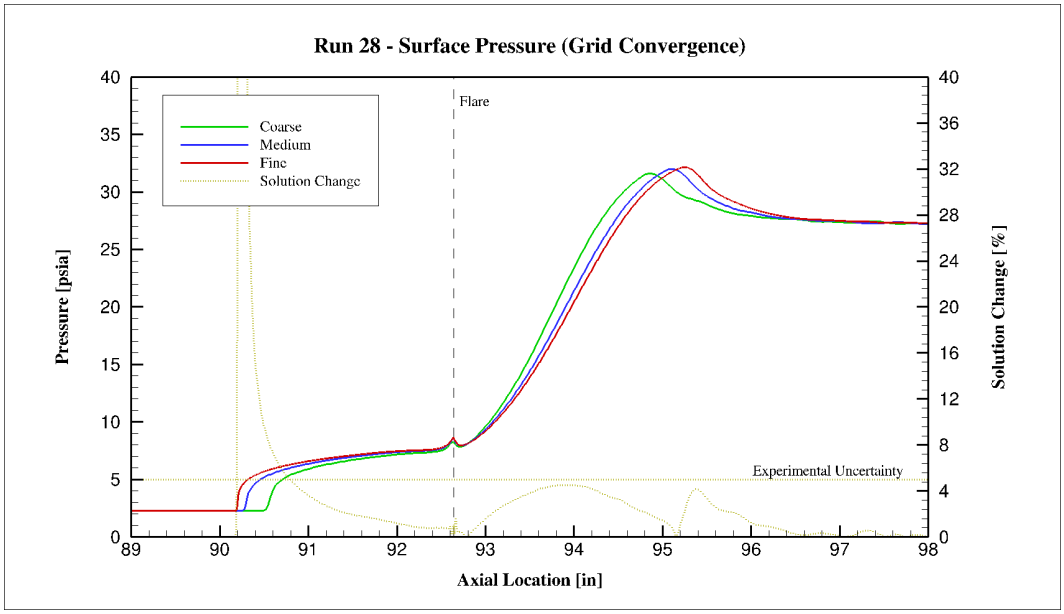

Figure 7.8: Run 28 - Surface Pressure (Grid Convergence)

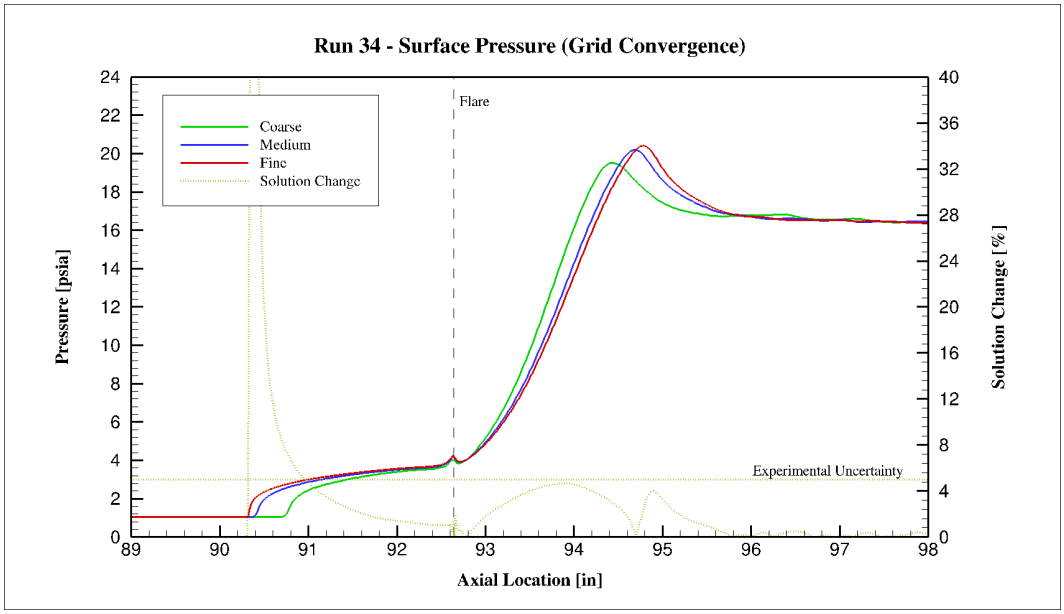

Figure 7.9: Run 34 - Surface Pressure (Grid Convergence)

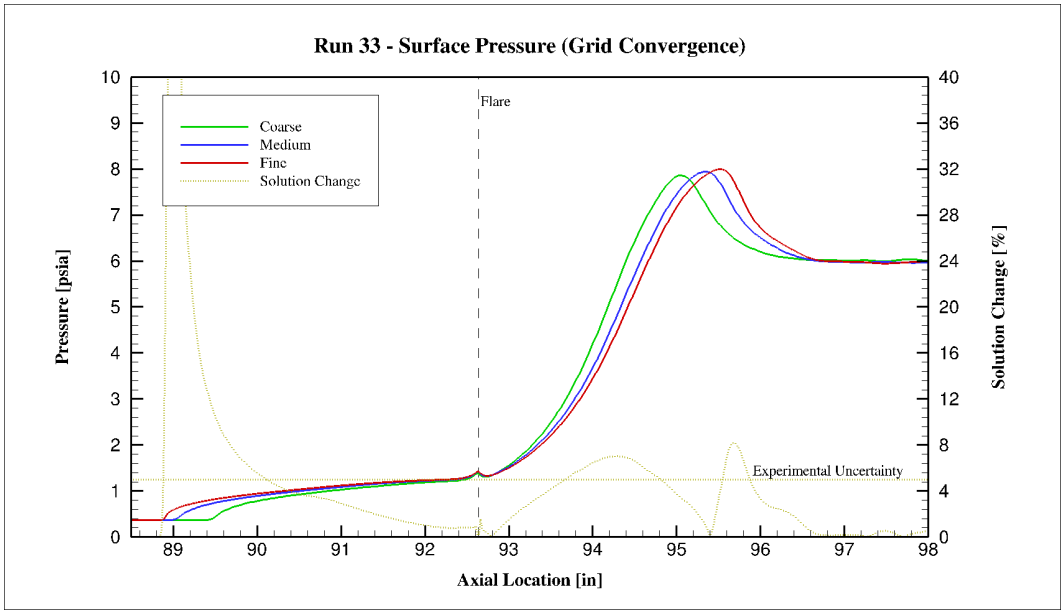

Figure 7.10: Run 33 - Surface Pressure (Grid Convergence)

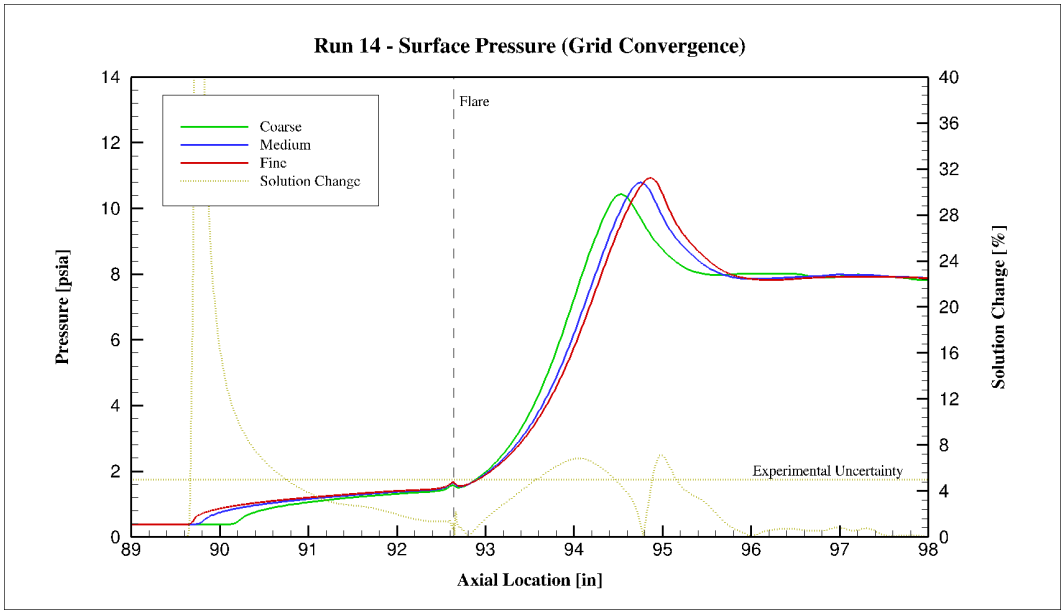

Figure 7.11: Run 14 - Surface Pressure (Grid Convergence)

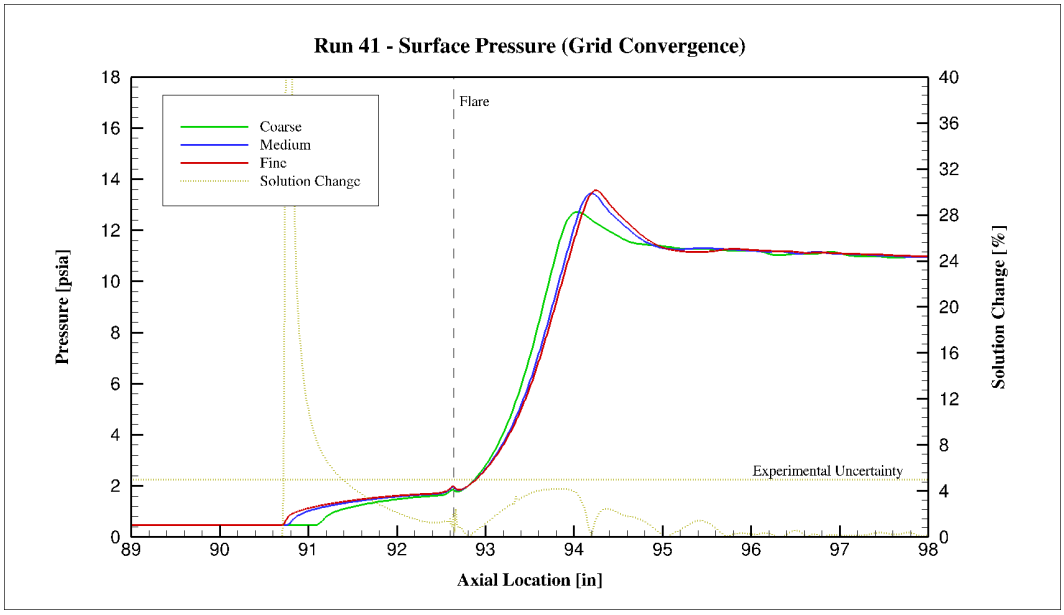

Figure 7.12: Run 41 - Surface Pressure (Grid Convergence)

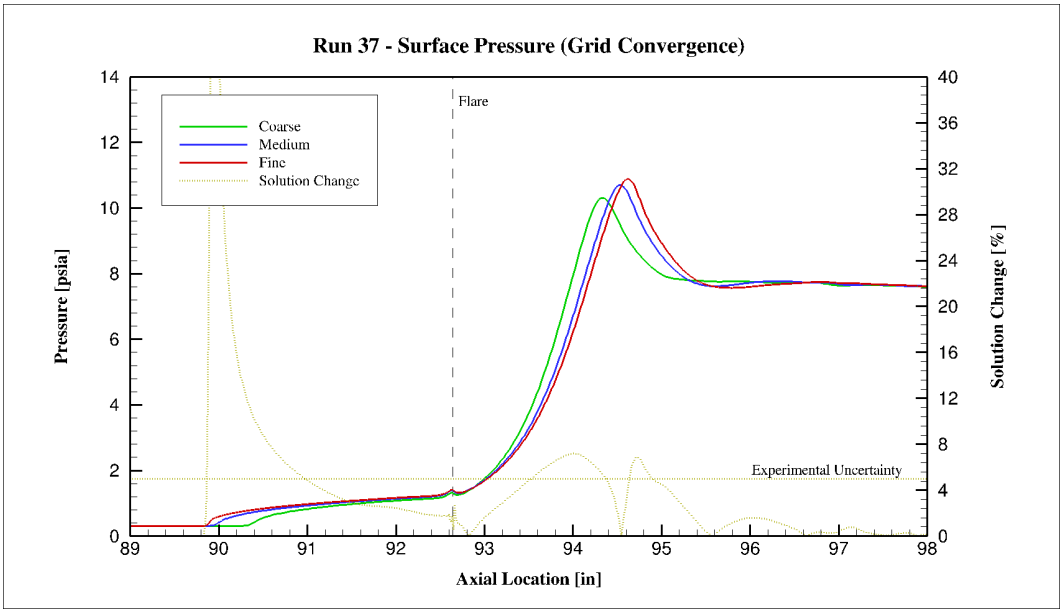

Figure 7.13: Run 37 - Surface Pressure (Grid Convergence)

2) Surface Heat Transfer

For surface heat transfer, average fore solution change for all runs is negligible at 1.11%. Average SBLI solution change for all runs is higher, but still within the experimental uncertainty at 3.31%. Minimum fore solution change is found in Run 41 at 0.71% (Figure 7.18), where maximum fore solution change is found in Run 33 at 1.60% (Figure 7.16). Minimum SBLI solution change is found in Run 41 at 2.25% (Figure 7.18), where maximum SBLI solution change is found in Run 33 at 4.04% (Figure 7.16). Peak surface heat transfer magnitude solution change and location displacement follow similar trends. Average peak solution change is negligible at 1.64% and average peak location displacement can be considered low at 0.12 inches. Minimum peak magnitude solution change is found in Run 37 at 0.83% (Figure 7.19), where maximum peak magnitude solution change is found in Run 33 at 2.85% (Figure 7.16). Minimum peak location displacement is found in Run 41 at 0.03 inches (Figure 7.18), where maximum peak location displacement is found in Run 34 at 0.15 inches (Figure 7.15). Associated surface heat transfer grid convergence plots are provided on the following pages (Figures 7.14-7.19).

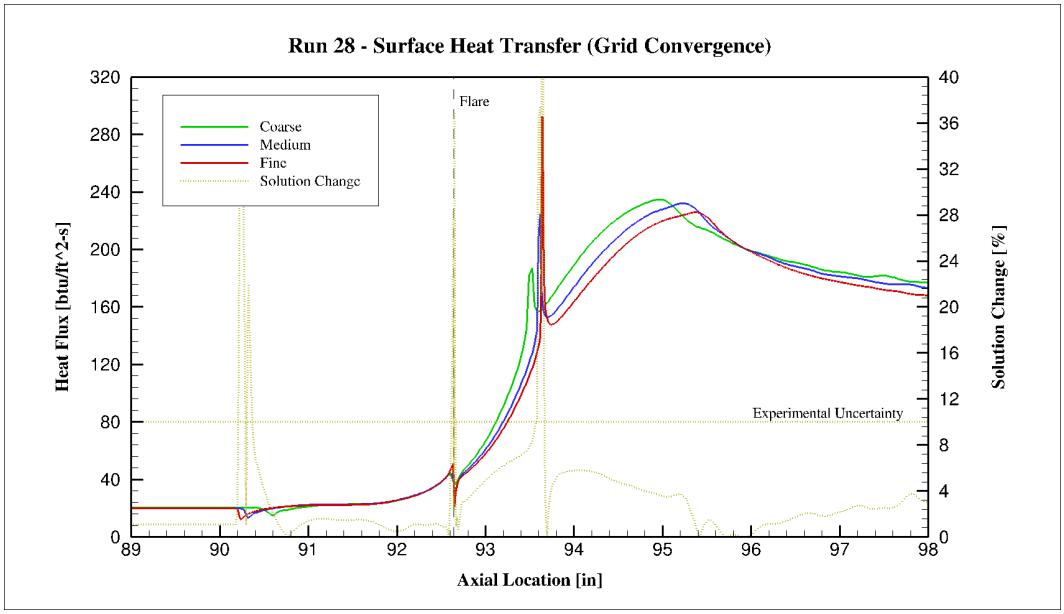

Figure 7.14: Run 28 - Surface Heat Transfer (Grid Convergence)

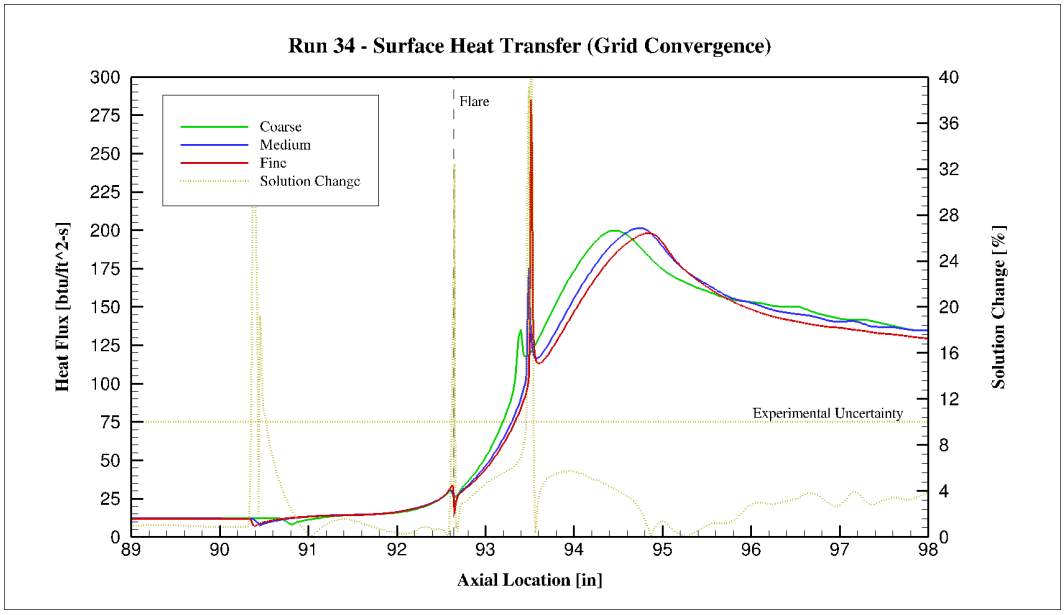

Figure 7.15: Run 34 - Surface Heat Transfer (Grid Convergence)

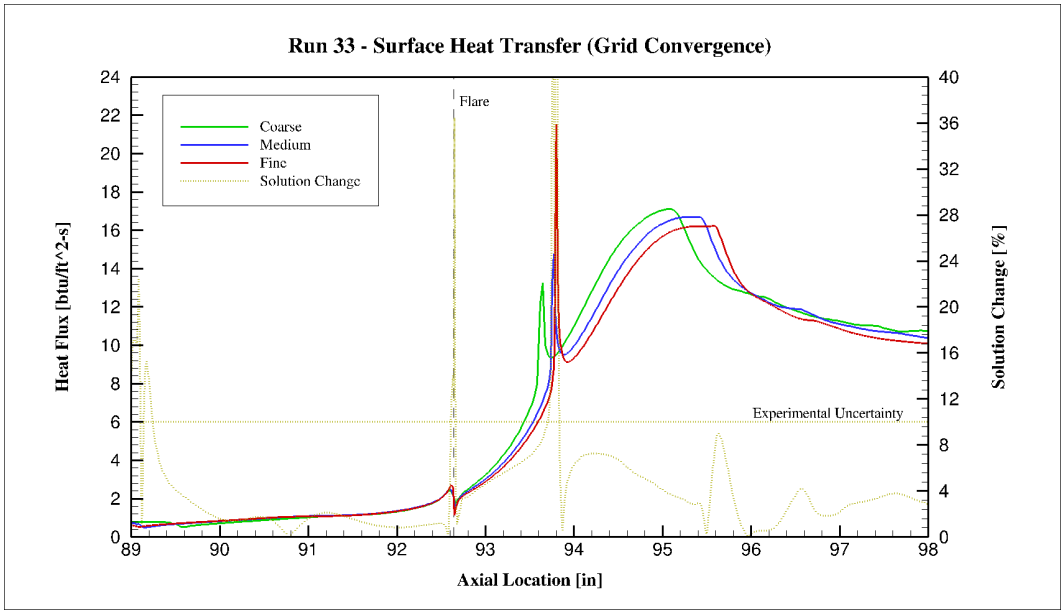

Figure 7.16: Run 33 - Surface Heat Transfer (Grid Convergence)

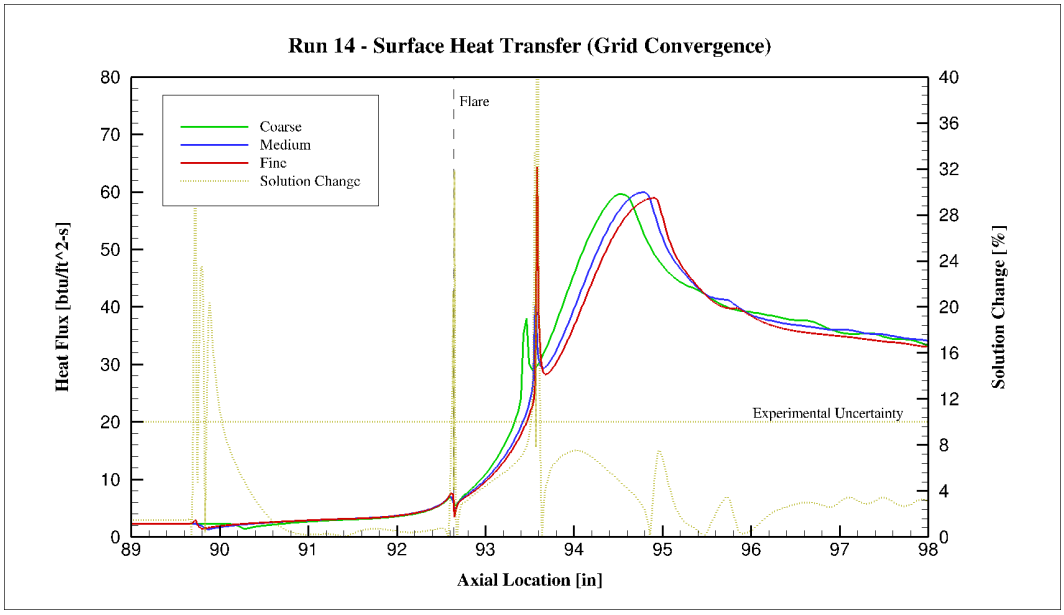

Figure 7.17: Run 14 - Surface Heat Transfer (Grid Convergence)

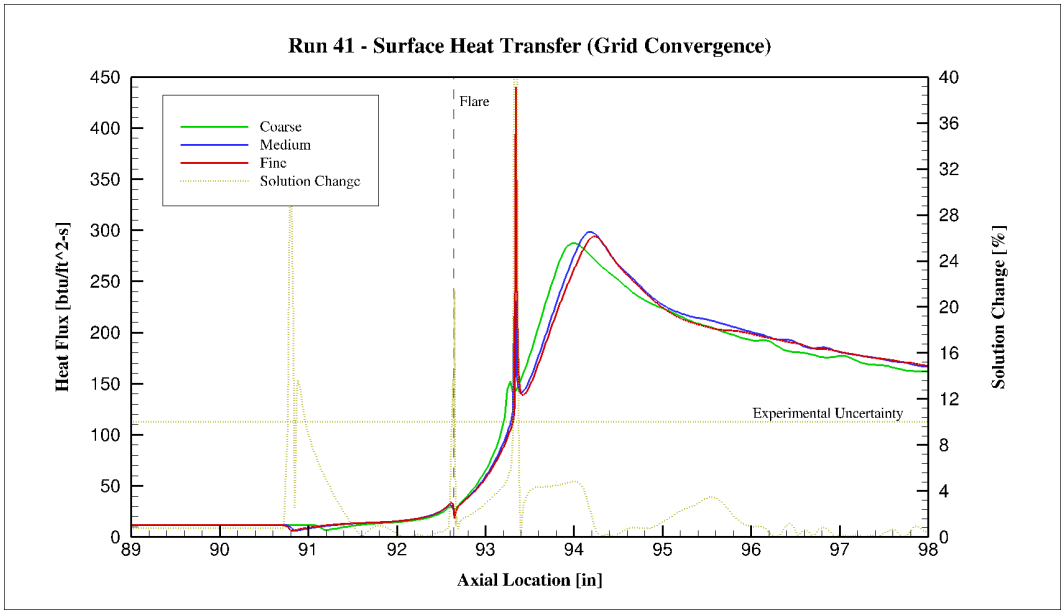

Figure 7.18: Run 41 - Surface Heat Transfer (Grid Convergence)

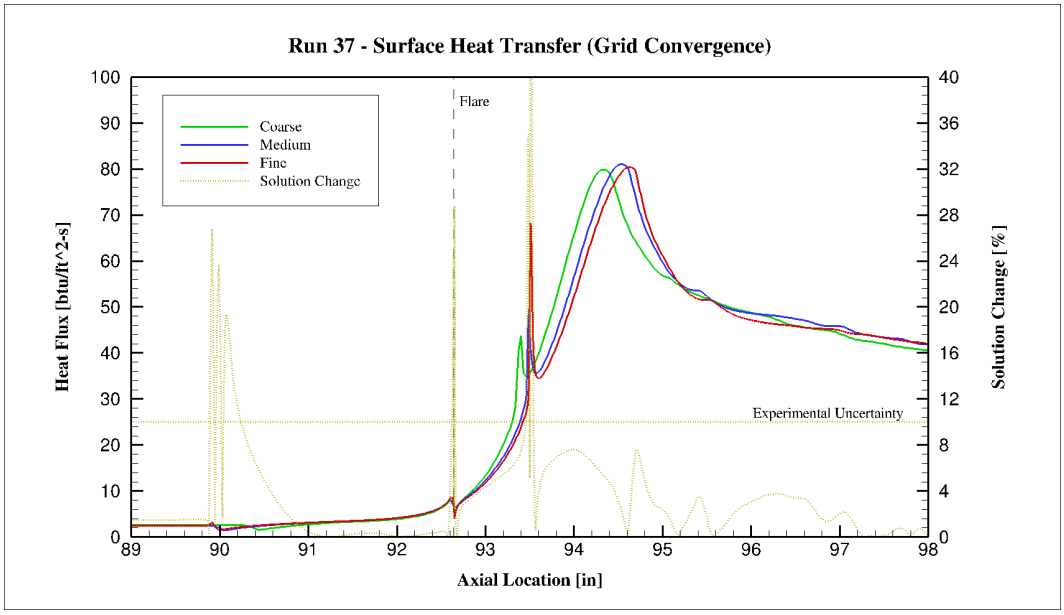

Figure 7.19: Run 37 - Surface Heat Transfer (Grid Convergence)

7.1.2 Comparison to Experiment

Now that grid independence is proven, final results can be compared to CUBRC. Comparison is mainly measured by percent error between the fine grid and interpolated experimental data. As with grid convergence, surface variable plots for each respective run are provided following discussion and tabulated data is included in "Final Remarks and Tabulated Data". Analysis of the information presented in this subsection is more comprehensive than grid convergence. Due to this, conclusions will be provided after the presentation of results in "Final Remarks and Tabulated Data" as well.

1) Surface Pressure Prediction

For surface pressure, average fore error for all runs is near the experimental uncertainty at 6.45%. However, average SBLI error for all runs is much higher at 36.9%. Minimum fore error is found in Run 14 at 3.23% (Figure 7.23), where maximum fore error is found in Run 37 at 11.2% (Figure 7.25). Minimum SBLI error is found in Run 14 at 28.0% (Figure 7.23), where maximum SBLI error is found in Run 41 at 44.6% (Figure 7.24). Peak surface pressure magnitude is predicted very well, averaging 7.96% for all runs. Minimum peak magnitude error is found to be as low as 1.27% in Run 14 (Figure 7.23), where maximum peak magnitude error is found in Run 33 at 18.0% (Figure 7.22). Peak surface pressure location is predicted with less accuracy, averaging a displacement of 0.82 inches. Minimum peak location displacement is found in Run 41 at 0.30 inches (Figure 7.24), where maximum peak location displacement is found to be as high as 1.54 inches in Run 28 (Figure 7.20). Associated surface pressure error plots are provided on the following pages (Figures 7.20-7.25).

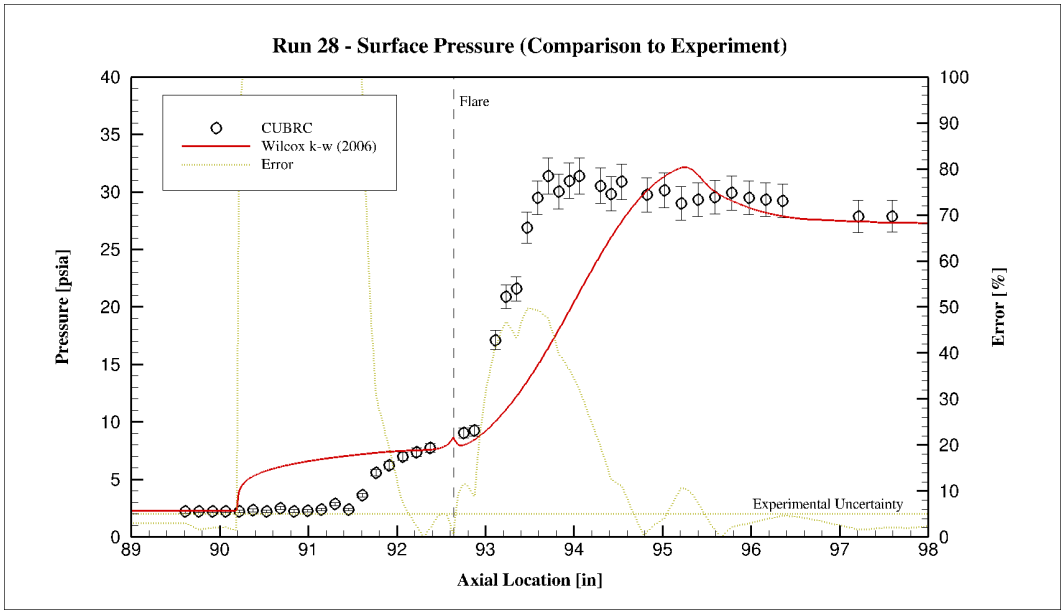

Figure 7.20: Run 28 - Surface Pressure (Comparison to Experiment)

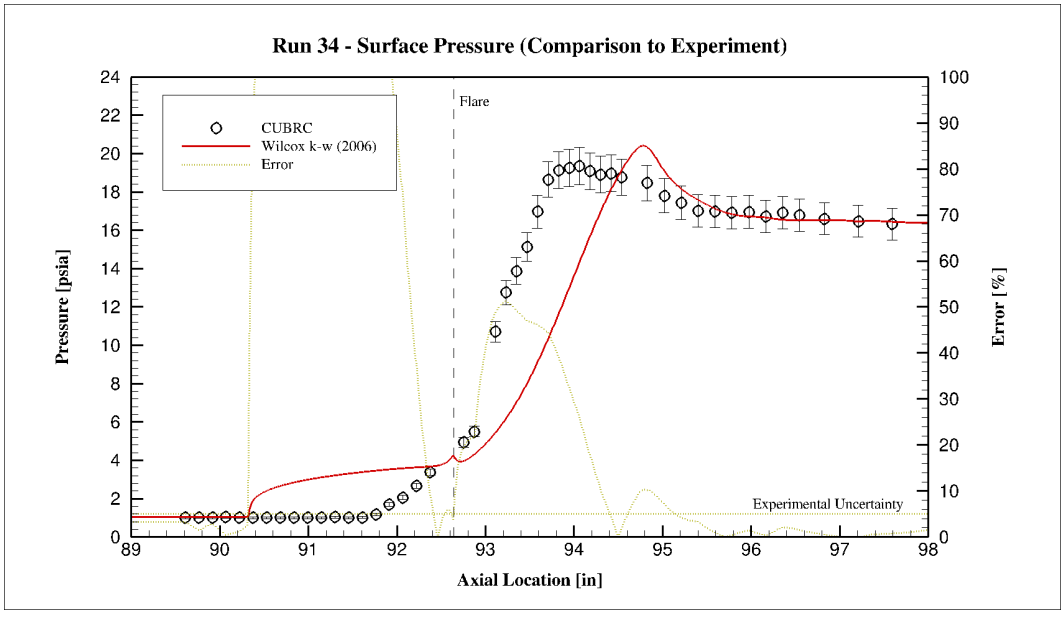

Figure 7.21: Run 34 - Surface Pressure (Comparison to Experiment)

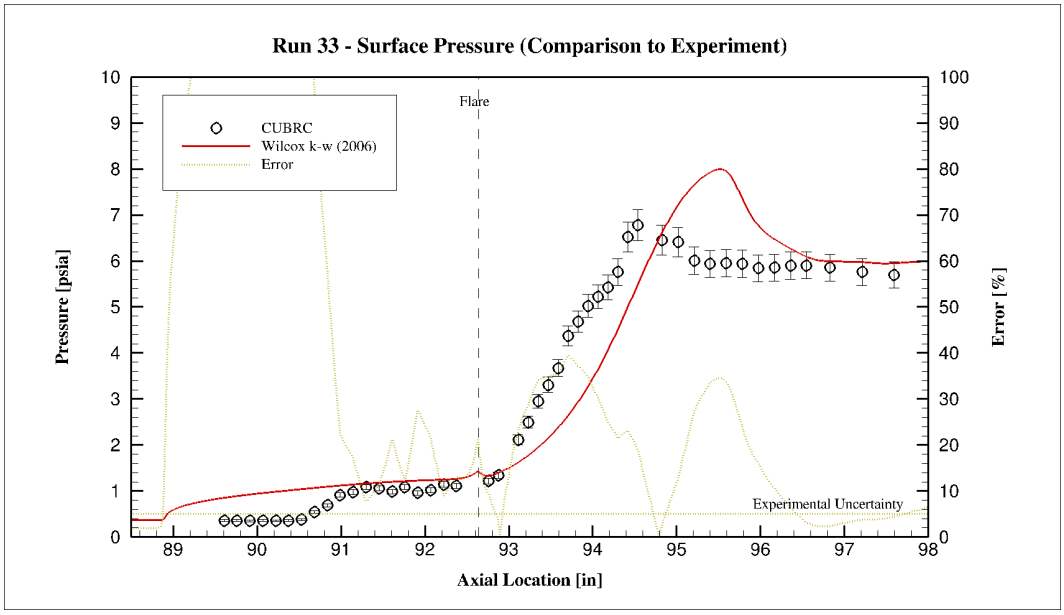

Figure 7.22: Run 33 - Surface Pressure (Comparison to Experiment)

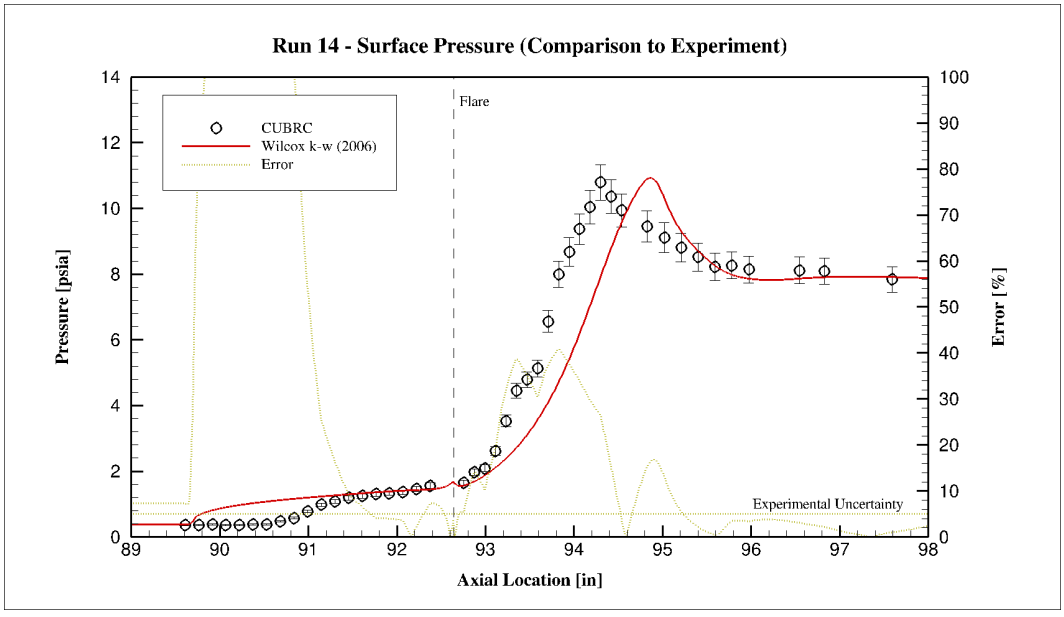

Figure 7.23: Run 14 - Surface Pressure (Comparison to Experiment)

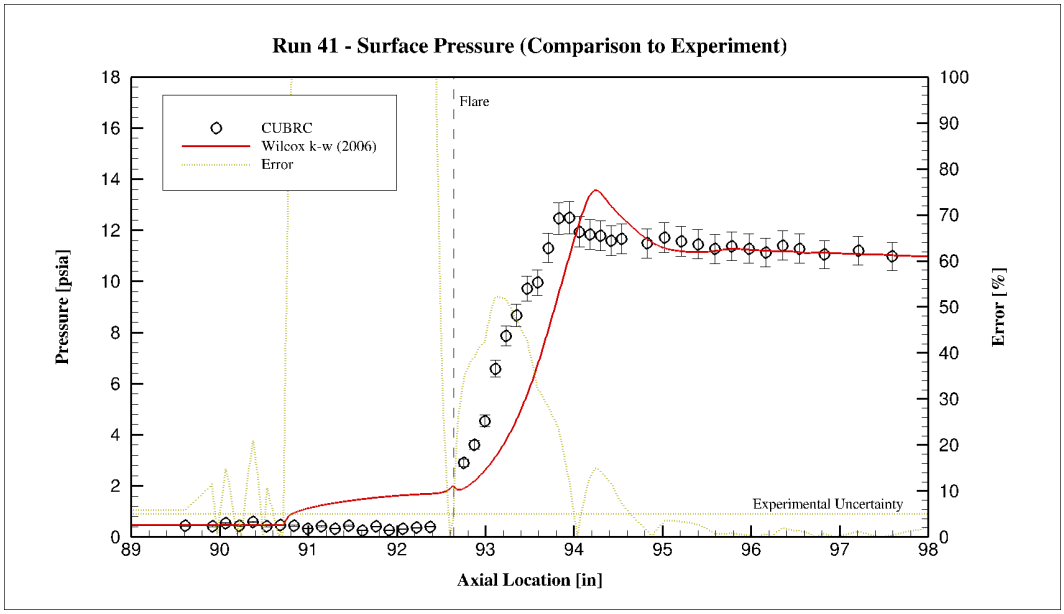

Figure 7.24: Run 41 - Surface Pressure (Comparison to Experiment)

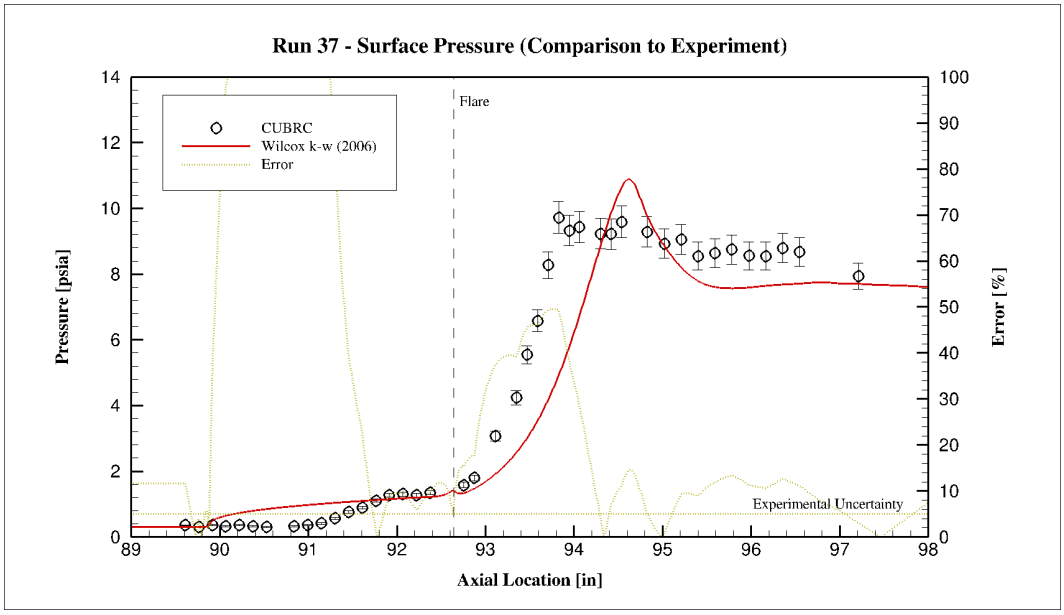

Figure 7.25: Run 37 - Surface Pressure (Comparison to Experiment)

2) Separation Over-Prediction

From Figures 7.20-7.25 and the discussion presented in (1), it can be concluded that surface pressure is predicted reasonably well overall. While the the average error in the SBLI region is very high at 36.9%, the primary source of error lies in the over-prediction of separation. Error is shown to be exceedingly higher in separation than post-flare in the SBLI region, thus causing the large percentage of error. Separation is over-predicted, on average, by 1.36 inches. Minimum over-prediction of separation is found in Run 14 at 0.89 inches (Figure 7.23), where maximum over-prediction is found to be as high as 1.70 inches in Run 33 (Figure 7.22).

3) Surface Heat Transfer Prediction

For surface heat transfer, average fore error for all runs is higher than surface pressure at 18.5%. Average SBLI error for all runs is also high at 29.5%, where the primary source of error is the over-prediction of heat transfer itself. Minimum fore error is found in Run 41 at 4.88% (Figure 7.30), where maximum fore error is found to be as high as 55.6% in Run 14 (Figure 7.29). Minimum SBLI error is found in Run 37 at 19.5% (Figure 7.31), where maximum SBLI error is found to be as high as 53.9% in Run 14 (Figure 7.29). Peak surface heat transfer location is predicted within the same ranges as pressure, averaging a displacement of 0.80 inches. Minimum peak location displacement is found in Run 41 at 0.52 inches (Figure 7.30), where maximum peak location displacement is found in Run 28 at 1.19 inches (Figure 7.26). However, peak surface heat transfer magnitude is predicted much more poorly, averaging 54.6% error. Minimum peak magnitude error is found in Run 37 at 29.8% (Figure 7.31), where maximum peak magnitude error is found to be over 100% in Run 14 (Figure 7.29). Associated surface heat transfer error plots are provided on the following pages (Figures 7.26-7.31).

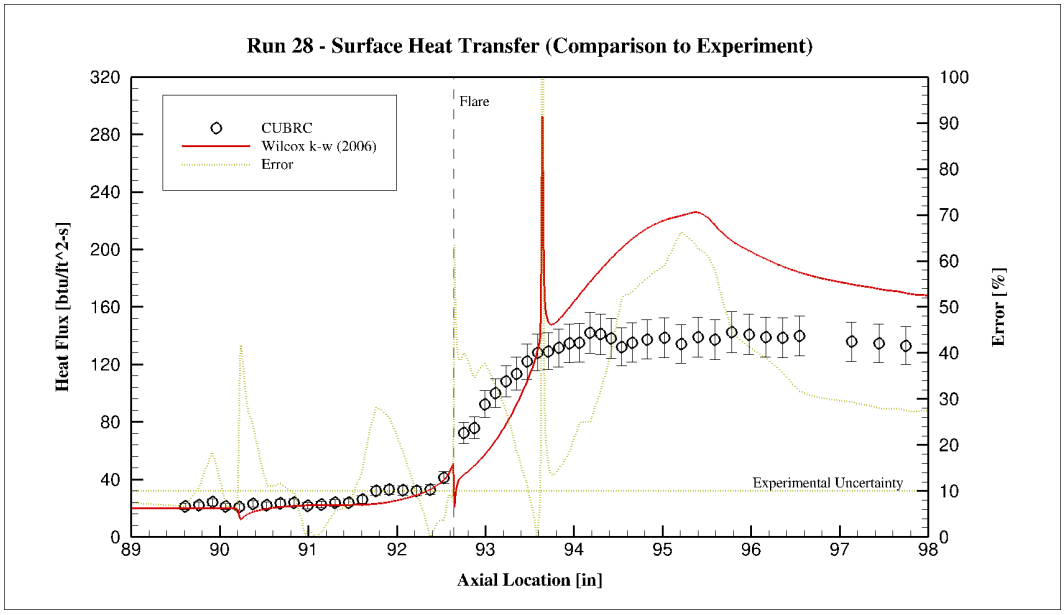

Figure 7.26: Run 28 - Surface Heat Transfer (Comparison to Experiment)

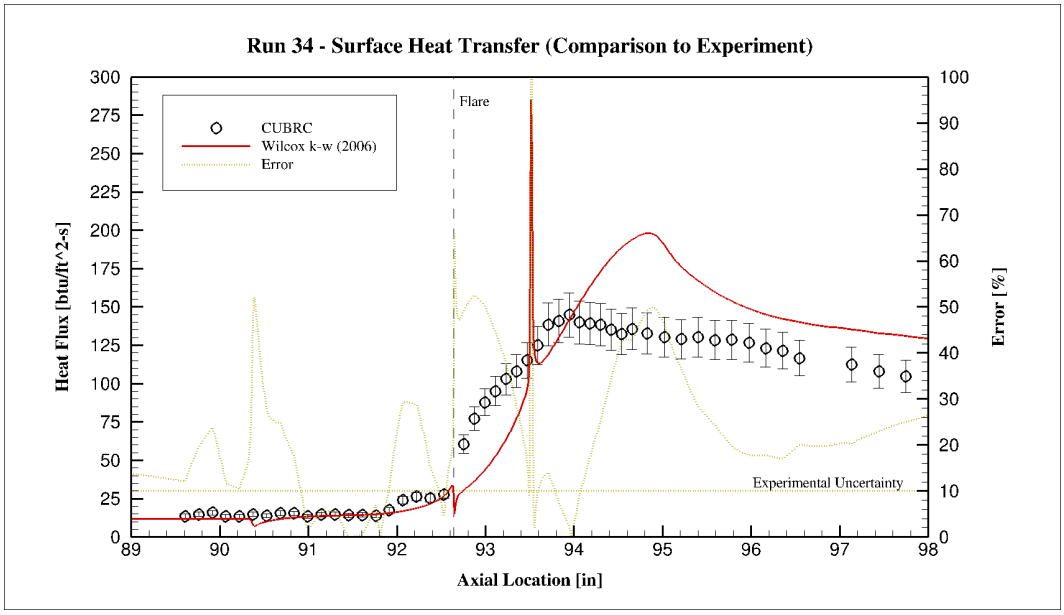

Figure 7.27: Run 34 - Surface Heat Transfer (Comparison to Experiment)

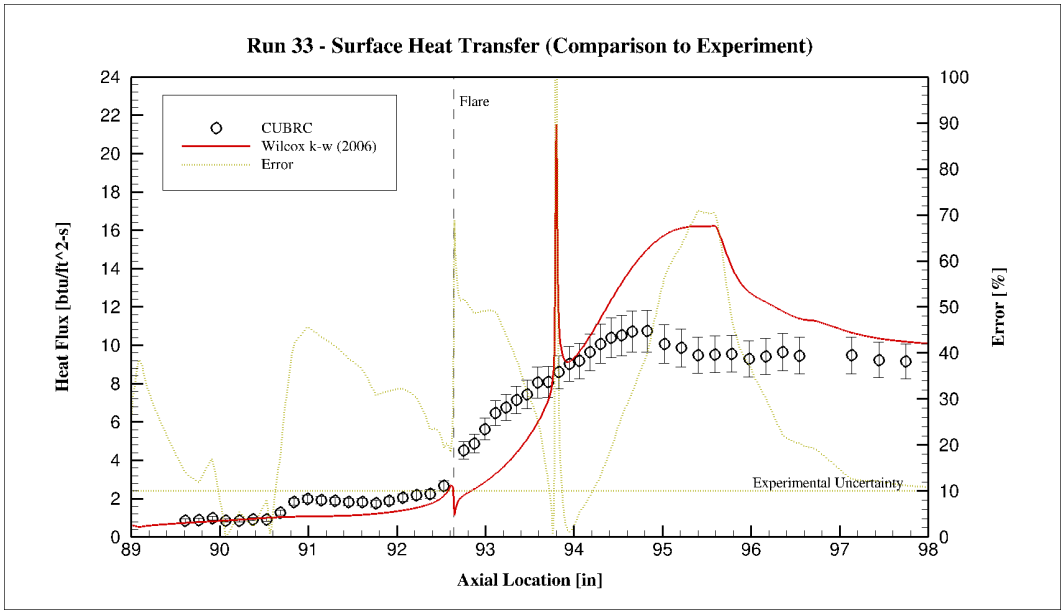

Figure 7.28: Run 33 - Surface Heat Transfer (Comparison to Experiment)

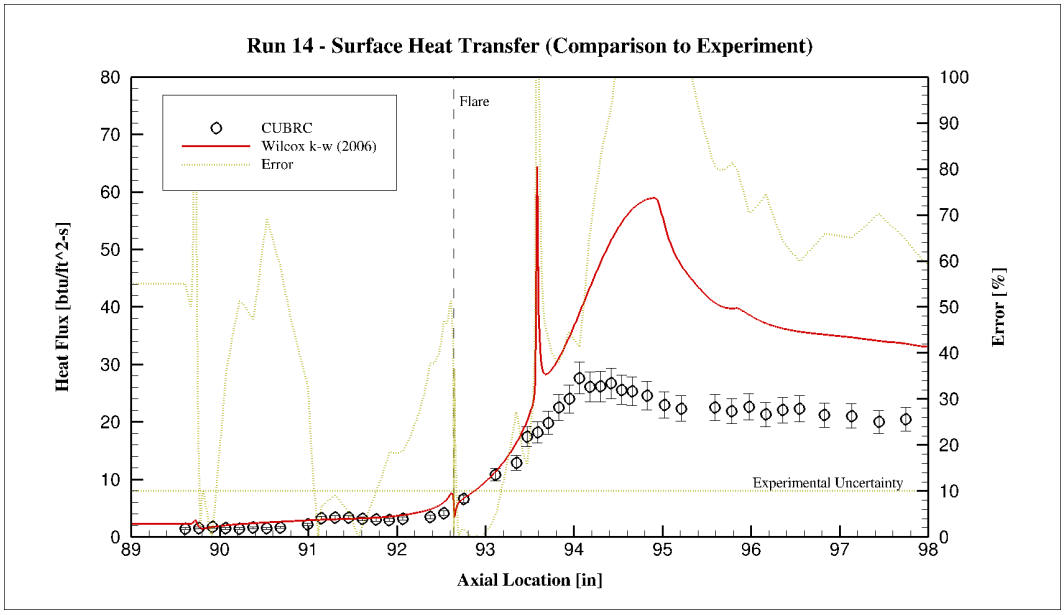

Figure 7.29: Run 14 - Surface Heat Transfer (Comparison to Experiment)

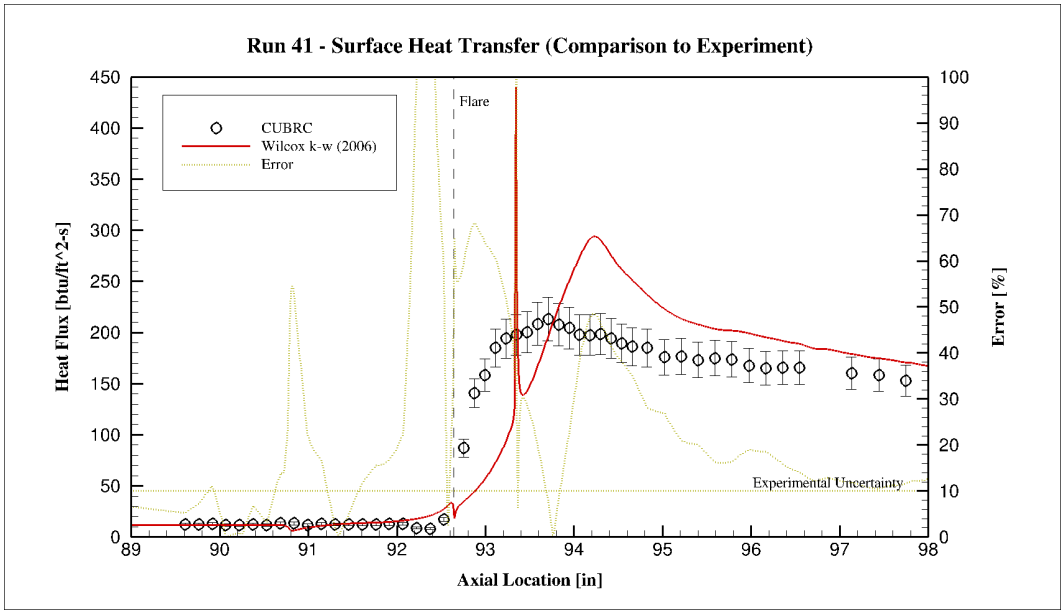

Figure 7.30: Run 41 - Surface Heat Transfer (Comparison to Experiment)

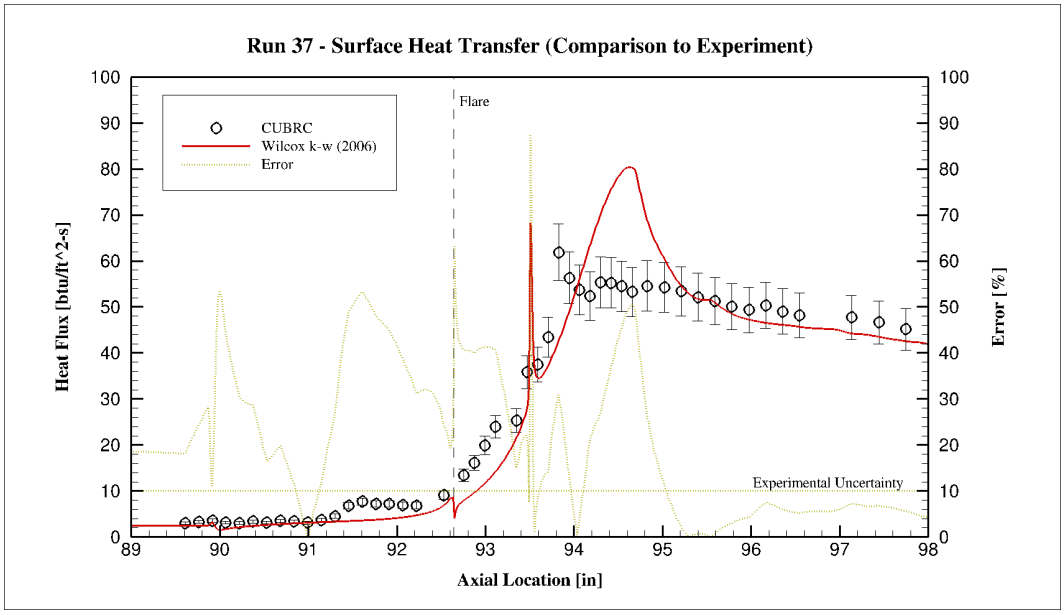

Figure 7.31: Run 37 - Surface Heat Transfer (Comparison to Experiment)

4) Anomalous Heat Transfer Spike

In addition to previous considerations, the Wilcox κ - ω model produces an anomalous surface heat transfer spike in all runs post-flare. While the spike has no physical significance, it can be attributed to an error in the turbulence model. The magnitude is almost always larger than peak surface heat transfer, averaging 125% of its value for all runs. It can also be noted that there is a direct dependence to a similar, exceedingly large, spike in turbulent kinetic energy κ near the wall. This dependence is clear considering that both spikes are practically positioned in the same location. In total, the κ-spike's magnitude averages over 8,000% of the near-wall κ value. In order to display this spike, turbulent kinetic energy is plotted near the spike for Run 28 (Figure 7.32). To create this plot, κ is taken one cell above the wall and compared to the surface heat transfer results for locational purposes. With this, it can be seen that the κ-spike is produced in same vicinity as the surface heat transfer spike (which is consistent in all runs).

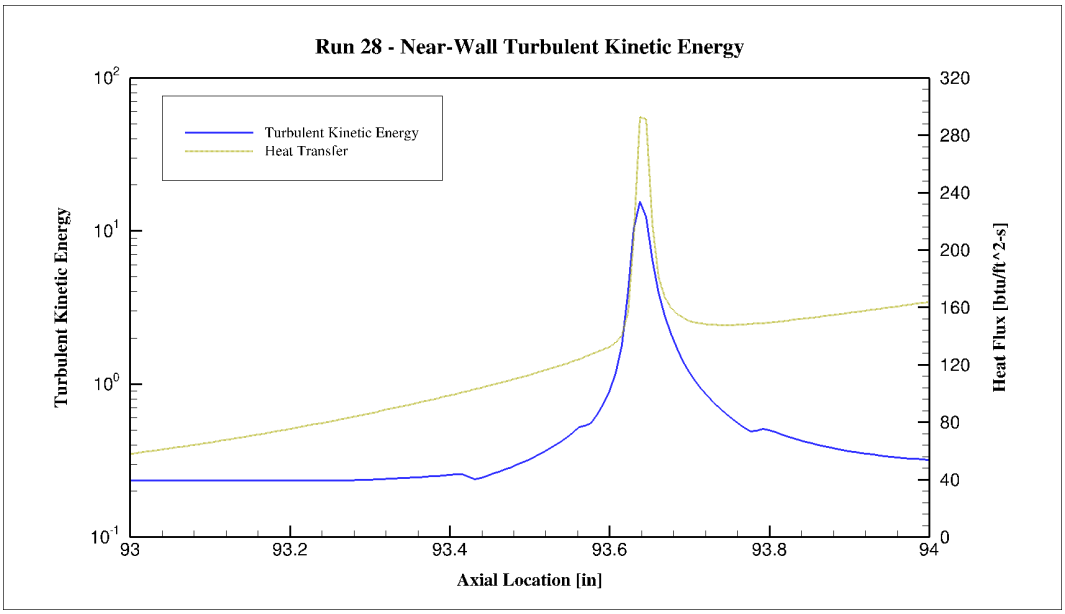

Figure 7.32: Run 28 - Near-Wall Turbulent Kinetic Energy

7.2 Final Remarks and Tabulated Data

In conclusion, it is apparent that the Wilcox κ - ω model has several advantages and disadvantages in regions of SBLI. First, the model predicts surface pressure within reason, but displacements of peak values and separation size are cause for concern. The model is also proven to predict surface heat transfer poorly in both the fore and SBLI region. Additionally, the anomalous spike in surface heat transfer and turbulent kinetic energy is another large cause for concern. Therefore, these factors need to be taken into consideration when employing the Wilcox κ - ω turbulence model in regions of SBLI. Future modifications to the model are dually required to increase predictive accuracy.

Tabulated Data

All of the associated grid convergence and experimental comparison data is provided on the following pages (Tables 7.2-7.7), as well as total run averages below (Table 7.1).

General Averages		Pressure	Heat Transfer
Fore (avg.)	Sol. Change	0.11 %	1.11 %
	Error	6.45 %	18.5 %
SBLI (avg.)	Sol. Change	3.41 %	3.31 %
	Error	36.9 %	29.5 %
Peak Values		**Pressure**	**Heat Transfer**
Displacement	Med $\rightarrow$ Fine	0.11 (in)	0.12 (in)
	Experiment	0.82 (in)	0.80 (in)
Magnitude	Sol. Change	1.03 %	1.64 %
	Error	7.96 %	54.6 %
Additional Analysis			
Displacement	Separation	Med $\rightarrow$ Fine	-0.13 (in)
		Experiment	-1.36 (in)
Magnitude	Heat-Spike	% of Peak Flux	125 %
		% of Average κ	8,400 %

Table 7.1: All Runs - Surface Variable Solution Averages

General Averages		Pressure	Heat Transfer
Fore (avg.)	Sol. Change	0.06 %	1.26 %
	Error	3.23 %	5.03 %
SBLI (avg.)	Sol. Change	4.04 %	3.67 %
	Error	34.6 %	27.9 %
Peak Values		**Pressure**	**Heat Transfer**
Displacement	Med → Fine	0.14 (in)	0.27 (in)
	Experiment	1.54 (in)	1.19 (in)
Magnitude	Sol. Change	0.47 %	1.78 %
	Error	2.4 %	59.1 %
Additional Analysis			
Displacement	Separation	Med → Fine	-0.11 (in)
		Experiment	-1.28 (in)
Magnitude	Heat-Spike	% of Peak Flux	129 %
		% of Average κ	6,631 %

Table 7.2: Run 28 - Surface Variable Solution Data

General Averages		Pressure	Heat Transfer
Fore (avg.)	Sol. Change	0.03 %	0.82 %
	Error	3.56 %	12.6 %
SBLI (avg.)	Sol. Change	2.82 %	3.26 %
	Error	42.9 %	23.3 %
Peak Values		**Pressure**	**Heat Transfer**
Displacement	Med → Fine	0.09 (in)	0.15 (in)
	Experiment	0.72 (in)	0.9 (in)
Magnitude	Sol. Change	1.11 %	1.43 %
	Error	5.45 %	36.8 %
Additional Analysis			
Displacement	Separation	Med → Fine	-0.09 (in)
		Experiment	-1.29 (in)
Magnitude	Heat-Spike	% of Peak Flux	143 %
		% of Average κ	7,903 %

Table 7.3: Run 34 - Surface Variable Solution Data

General Averages		Pressure	Heat Transfer
Fore (avg.)	Sol. Change	0.37 %	1.60 %
	Error	6.61 %	13.0 %
SBLI (avg.)	Sol. Change	4.25 %	4.04 %
	Error	34.5 %	27.9 %
Peak Values		**Pressure**	**Heat Transfer**
Displacement	Med → Fine	0.17 (in)	0.03 (in)
	Experiment	0.98 (in)	0.56 (in)
Magnitude	Sol. Change	0.69 %	2.85 %
	Error	18.0 %	50.9 %
Additional Analysis			
Displacement	Separation	Med → Fine	-0.22 (in)
		Experiment	-1.70 (in)
Magnitude	Heat-Spike	% of Peak Flux	133 %
		% of Average κ	7,120 %

Table 7.4: Run 33 - Surface Variable Solution Data

General Averages		Pressure	Heat Transfer
Fore (avg.)	Sol. Change	0.02 %	0.95 %
	Error	7.75 %	55.6 %
SBLI (avg.)	Sol. Change	3.10 %	3.27 %
	Error	28.0 %	53.9 %
Peak Values		**Pressure**	**Heat Transfer**
Displacement	Med → Fine	0.11 (in)	0.15 (in)
	Experiment	0.56 (in)	0.84 (in)
Magnitude	Sol. Change	1.27 %	1.54 %
	Error	1.27 %	113 %
Additional Analysis			
Displacement	Separation	Med → Fine	-0.15 (in)
		Experiment	-0.89 (in)
Magnitude	Heat-Spike	% of Peak Flux	109 %
		% of Average κ	7,500 %

Table 7.5: Run 14 - Surface Variable Solution Data

General Averages		Pressure	Heat Transfer
Fore (avg.)	Sol. Change	0.06 %	0.71 %
	Error	6.37 %	4.88 %
SBLI (avg.)	Sol. Change	2.26 %	2.25 %
	Error	44.6 %	24.6 %
Peak Values		**Pressure**	**Heat Transfer**
Displacement	Med → Fine	0.05 (in)	0.03 (in)
	Experiment	0.30 (in)	0.52 (in)
Magnitude	Sol. Change	0.88 %	1.42 %
	Error	8.61 %	38.1 %
Additional Analysis			
Displacement	Separation	Med → Fine	-0.08 (in)
		Experiment	-1.66 (in)
Magnitude	Heat-Spike	% of Peak Flux	149 %
		% of Average κ	13,500 %

Table 7.6: Run 41 - Surface Variable Solution Data

General Averages		Pressure	Heat Transfer
Fore (avg.)	Sol. Change	0.11 %	1.30 %
	Error	11.2 %	19.9 %
SBLI (avg.)	Sol. Change	3.96 %	3.34 %
	Error	34.6 %	19.5 %
Peak Values		**Pressure**	**Heat Transfer**
Displacement	Med → Fine	0.08 (in)	0.09 (in)
	Experiment	0.80 (in)	0.80 (in)
Magnitude	Sol. Change	1.76 %	0.83 %
	Error	12.0 %	29.8 %
Additional Analysis			
Displacement	Separation	Med → Fine	-0.15 (in)
		Experiment	-1.32 (in)
Magnitude	Heat-Spike	% of Peak Flux	84.9 %
		% of Average κ	7,724 %

Table 7.7: Run 37 - Surface Variable Solution Data

Chapter 8

Future Work

In light of the results obtained in this thesis, two main categories of future work can be specified. The first consideration lies with the anomalous spike in surface heat transfer. It was observed that the spike is associated to a similar spike in near-surface turbulent kinetic energy. The spike was also observed to be correlated to grid refinement, where it was seen to disappear in previous, less refined, grid configurations. This leads to the main question: "What is the cause of the anomalous spike"? Aside from the turbulence model, possible reasons may include the flux/temporal schemes, boundary conditions, grid sequences, input parameters, etc. However, as a similar spike was seen in an identical study by Patel [16], it is likely that the reason lies inherently in the Wilcox κ - ω turbulence model. Collectively, the first category of future work can be defined as:

1) Investigation of the Anomalous Surface Heat Transfer Spike

The next consideration is the main concern of the Wilcox κ - ω turbulence model. In regards to prediction of shock-wave boundary-layer interaction (SBLI), the model produces significant discrepancies to experimental results. Accuracy of predications are shown to be dependent on the freestream conditions, preforming better/worse for differing runs. In addition, while overall accuracy of surface pressure pressure is reasonable, separation is alarmingly over-predicted. Surface heat transfer is consistently predicted poorly, as well. These findings are not new, as various studies have made similar observations. Thus, the second category of future work can be defined as:

2) Improvement of the Wilcox κ - ω Predictability in SBLI

References

[1] R Stimson. The Wright Stories, History of Flight. http://wrightstories.com.

[2] T von Karman. Aerodynamics Selected Topics in the Light of Their Historical Development. *Journal of the Franklin Institute*, 1954.

[3] J Anderson. *A History of Aerodynamics: And Its Impact on Flying Machines*. Cambridge Aerospace Series. Cambridge University Press, 1997.

[4] J Anderson. Research in Supersonic Flight and the Breaking of the Sound Barrier. *From Engineering Science to Big Science:*, 1998.

[5] Bell X-1B. https://www.nasa.gov, 2017.

[6] G BarMeir. *Fundamentals of Compressible Fluid Mechanics*. 2006.

[7] A Jameson. Computational Fluid Dynamics Past, Present and Future. Technical Report, Stanford University, 2012.

[8] J Merodio and G Saccomandi. *Continuum Mechanics*, volume 3. 2011.

[9] D Wilcox. *Turbulence Modeling for CFD*. DCW Industries, Inc., 3rd edition, 2006.

[10] S Pope. *Turbulent flows*. Cambridge University Press, 1st edition, 2000.

[11] P Spalart, W Jou, M Stretlets, and S Allmaras. Comments on the Feasibility of LES for Wings and on the Hybrid RANS/LES Approach. *AFOSR International Conference*, 1997.

[12] D Dolling. Fifty Years of Shock Wave Boundary Layer Interaction Research: What Next? *AIAA Journal*, 39(8):1517–1531, August 2001.

[13] D Knight and G Degrez. Shock Wave Boundary Layer Interactions in High Mach Number Flows - A Critical Survey of Current CFD Prediction Techniques. AGARD Advisory Report AR-319, Vol. 2, AGARD, 1998.

[14] D Knight, H Yan, A Panaras, and A Zheltovodov. Advances in CFD Prediction of Shock Wave Turbulent Boundary Layer Interaction. *Progress in Aerospace Sciences*, 39:121–184, 2003.

[15] A Oliver, R Lillard, A Schwing, G Blaisdell, and A Lyrintzis. Assessment of Turbulent Shock Boundary Layer Interaction Computations Using the OVERFLOW code. *45th AIAA Aerospace Sciences Meeting and Exhibit*, January 2007.

[16] S Patel. Evaluation of $\kappa - \omega$ Turbulence Model and Euler Flux Schemes for Shock Wave Turbulent Boundary Layer Interactions. Master's thesis, Rutgers University, 2018.

[17] G Batchelor. *An Introduction to Fluid Dynamics*. Cambridge Mathematical Library. Wiley, 2000.

[18] J Anderson. *Modern Compressible Flow*. McGraw Hill, New York, 2003.

[19] G Mase, T Mase, and R Smelser. *Continuum Mechanics for Engineers*. Computational Mechanics and Applied Analysis. CRC Press, 2nd edition, 1999.

[20] H Goldstein, C Poole, and J Safko. *Classical Mechanics*. Addison-Wesley, 3rd edition, 2000.

[21] R Fox, A McDonald, and P Pritchard. *Introduction to Fluid Dynamics*. Cambridge University Press, 6th edition, 2002.

[22] AMES Research Staff. Equations, Tables and Charts for Compressible Flow. Technical report, Ames Aeronautical Laboratory, 1953.

[23] J Bibin, V Kulkarni, and G Natarajan. Shock wave boundary layer interactions in hypersonic flows. *International Journal of Heat and Mass Transfer*, 70:81 – 90, 2014.

[24] H Tennekes and J Lumley. *A First Course in Turbulence*. MIT Press, 1972.

[25] P Davidson. *Turbulence: An Introduction for Scientists and Engineers*. Oxford University Press, 2004.

[26] U Frisch. *Turbulence: The Legacy of A. N. Kolmogorov*. Cambridge, New York, 1995.

[27] F Incropera. *Fundamentals of Heat and Mass Transfer*. John Wiley & Sons, Inc., USA, 2006.

[28] J Delery and JP Dussauge. Some physical aspects of shock wave/boundary layer interactions. *Shock Waves*, 19, July 2009.

[29] T Apostol. *Mathematical Analysis*. Series in Mathematics. Addison-Wesley, 2nd edition, 1974.

[30] J Anderson. *Computational Fluid Dynamics: the Basics with Applications*. Series in Mechanical Engineering. McGraw-Hill, 1st edition, 1995.

[31] H Versteeg and W Malalasekera. *An Introduction to Computational Fluid Dynamics: The Finite Volume Method*. Pearson, 2nd edition, 2007.

[32] D Knight. *Elements of Numerical Methods for Compressible Flows*. Cambridge University Press, New York, 2006.

[33] J Mathews and K Fink. *Numerical Methods using MATLAB*. Prentice Hall, 3rd edition, 1998.

[34] Y Saad. *Iterative Methods for Sparse Linear Systems*. Society for Industrial and Applied Mathematics, 2nd edition, 2003.

[35] *GASPex Technical Reference Guide*. Blacksburg, VA.

[36] T Wadhams, M Holden, and M MacLean. Comparison of Experimental and Computational Results from 'Blind' Turbulent Shock Wave Interaction Study Over Cone Flare and Hollow Cylinder Flare Configuration. AIAA Aviation Presentation, 2014.

[37] CUBRC Website. https://www.cubrc.org.

[38] T Wadhams, E Mundy, M MacLean, and M Holden. Pre-Flight Ground Testing of the Full-Scale HIFiRE-1 Vehicle at Fully Duplicated Flight Conditions. *American Institute of Aeronautics and Astronautics 46th AIAA Aerospace Sciences Meeting and Exhibit*, 2008.